UNIVERSITÀ DEGLI STUDI DI VERONA

DEPARTMENT OF COMPUTER SCIENCE

DOCTORAL PROGRAM IN COMPUTER SCIENCE

XXXVI CYCLE, 2023

Exploiting flexible links in surgical applications: from interaction control to needle insertion

Author:
Chiara ZANDONA'

Supervisor:
Prof. Andrea CALANCA

PhD Program Coordinator:

Prof. Ferdinando CICALESE

Submitted in fulfilment of the requirements for the degree of Doctor of Philosophy at the Department of Computer Science

S.S.D. ING-INF/05

March 2024

Abstract

This thesis aims to contribute to the goal of improving autonomy in robotic surgery, focusing on the following challenges: (1) the development of accurate models for flexible surgical tools, (2) the investigation of properties for the real-time control of surgical instruments, during the execution of minimally invasive robotic surgery.

In the first part of the thesis, we investigate interaction control algorithms that take advantage of the inherent flexibility of commonly used surgical instruments. We leverage continuum mechanics theory and high-order approximants to model the surgical instrument and investigate passivity and stability properties. For the first time, this thesis theoretically demonstrates that force control based on a collocated feedback signal from a continuum flexible beam can be passive with respect to the environment port, meaning that stability can be guaranteed in any passive environment. On the other hand, when the feedback is non-collocated, passivity may be hampered, and these cases are analyzed using a high-order lumped approximant. An experimental validation using real-world surgical instruments is provided, showing coherence with theoretical expectations.

In the second part, we focus on modelling the interaction between a bevel-tip biopsy needle and the surrounding tissue to enable automated needle insertion during a robotic prostate biopsy. In this context, the objective is to estimate the deflection of the tip during insertion and to plan the trajectory accordingly. An experimental comparison is conducted to assess the accuracy of existing models in predicting needle deflection.

"Success is not final; failure is not fatal;
it is the courage to continue that counts."

- Winston S. Churchill

Contents

List of Figures

IV

List of Tables

List of Abbreviations and Symbols

Abbreviations

ARS	The Autonomous Robotic Surgery ERC Project
ASTM	American Society for Testing and Materials International standards
DoF	One degree of freedom
ERC	European Research Council
FE/FEM	Finite elements/Finite elements model
GAN	Generative Adversarial Network model
MICCAI	International Conference on Medical Image Computing and Computer-Assisted Intervention
MRI	Magnetic resonance imaging
PCa	Prostate cancer
PROST	The Autonomous Prostate Biopsy ERC Project
PSA	Prostate specific antigen
RGB-D	Type of depth camera that provides both depth (D) and color (RGB) data as the output in real-time
UTM	Universal Testing Machine

PART I - Flexible Link and Force Control Symbols

$(')$	Space derivative
$(\cdot)$	Time derivative
α	Parameter to reduce motor inertia
$\cos(x)$	Cosine of the angle x

$\delta\mathcal{F}$	Variation of the action functional
$\mathbb{R}$	Set of real numbers
$\mathcal{F}$	Action functional
$\mathcal{L}$	Lagrangian equation
$\mathcal{V}$	Lyapunov candidate function
ν_{RATIO}	Poisson ratio of the link
τ_{link}	Kinetic energy of the link
τ_{motor}	Kinetic energy of the motor
τ_{tip}	Kinetic energy of the mass m placed on the tip of the link on which F_E acts
τ_{TOT}	Total kinetic energy
ν	Potential energy
$\omega''(t,r)$	Link bending torque at a spatial coordinate r expressed in the motor body frame $X_1Y_1Z_1$
$\omega'(t,0)$	Link bending angle at the base of the link
$\omega(t,0)$	Link bending displacement at the base of the link
$\omega(t,r)$	Link bending displacement at a spatial coordinate r expressed in the motor body frame $X_1Y_1Z_1$
ω_S	Low-frequency peak of the system $G(s)$
$\omega_E(t)$	Link bending displacement at the end of the link
ρ	Uniform mass density per unit length of the link
$\sin(x)$	Sine of the angle x
τ_0	Torsional spring torque at the base of the link
τ_i	Torsional spring torque related to the i-th link block
$\tau_m(t)$	Torque developed by the motor
τ_{n-1}	Interaction torque with the environment
$\mathbf{P}$	Tip position vector
$\mathbf{r}$	Position vector of an infinitesimal portion of the link at r

$I(s)$	System impedance in the linear representation model of flexible link and the model of a flexible link with a bending stiffness
$I_n(s)$	System impedance of the system discretized into n blocks
j_i	Rotational moment of inertia of the i-th link block
J_m	Moment of inertia of the motor
K	Bending stiffness of the link
k_0	Stiffness of the motor gearbox
k_i	Stiffness of the i-th link block
k_p	Proportional gain
L	Length of the link
l	Distance between one link block and another
M	Mass of the link
m_i	Mass of the i-th link block
M_m	Mass of the motor
$min\_distance$	Distance of the system $G(s)$ from the instability
Min_i	I-th minor of the Hurwitz matrix
n	Number of rigid block in which the system is discretized
$N(i\omega)$	Numerator of the system impedance in Frequency domain
$N(s)$	Numerator of the system impedance in Laplace domain
O	Origin of the fixed frame XYZ
O_1	Origin of the motor shaft frame $X_1Y_1Z_1$
$P(s)$	Characteristic polynomial of the system impedance
$P_{M_i}(s)$	Subsystem defining the relation between τ_m and τ_i in Laplace domain
q_i	Position of the center of mass and inertia of the i-th link block
r	Spatial coordinate expressed in the motor body frame $X_1Y_1Z_1$
$Re(N(i\omega))$	Real part of the numerator $N(i\omega)$
$Re(s)$	Real part of the system $G(s)$
S	Shear modulus of the link

t	Time
t_i	Integration bounds
$X_1 Y_1 Z_1$	Motor shaft frame of the system motor-link
x_i	Linear equivalent position of the i-th link block
x_m	Linear equivalent position of the motor
XYZ	Fixed frame of the system motor-link
vec	Bold symbols represent the vectors
a	Real part of the denominator $D(i\omega)$
b	Imaginary part of the denominator $D(i\omega)$
vec	Normal symbols represent the scalar and vector modules

PART II - Needle Insertion and Deflection Symbols

(z, y)	Location of the tip of the needle (Unicycle model) and the location of the back wheel of the needle (Extended Bicycle model)
α	Back wheel slippage which depends on λ in the Extended Bicycle model
β	Front fixed angle in the Extended Bicycle model
Δd	Variation of the needle tip depth between two sample times
Δy	Variation of the needle tip deflection between two sample times
Δz	Variation of the needle tip insertion between two sample times
γ	Angle between the z-axis of the $\{A\}$ frame and the needle tip path in the Extended Bicycle model
γ	Angle between the z-axis of the $\{A\}$ frame and the z-axis of the $\{B\}$ frame in the Unicycle model
λ_i	Mechanical tissue properties in the Extended Bicycle model
$\omega_{exp}(l)$	Average final tip deflection
ρ_i	Coefficients of the least-square identification regression of the Unicycle model
σ_{eM_i}	Standard deviation of the error identification of the M_i model
σ_{exp}	Standard deviation of the final tip position

θ	Angle between the z-axis of the $\{A\}$ frame and the z-axis of the $\{B\}$ frame in the Extended Bicycle model
$\{A\}$	Global fixed frame of the needle system
$\{B\}$	Frame of the back-wheel of the needle system
$\{C\}$	Frame of the front-wheel of the needle system
$c = [0, c_y]$	Center of the fixed curvature of the needle in the Unicycle model
e_{maxM_i}	Maximum tip prediction error of the M_i model
e_{meanM_i}	Average tip error identification of the M_i model
F	Force normal to the bevel tip
l	Distance between the two wheel of the needle in the Extended Bicycle Model
M_i	Unicycle model (M_1) and Extended Bicycle model (M_2)
O_A	Origin of the fixed frame $\{A\}$
Q	Resultant vertical force which causes the needle bending
q	Distributed load applied to the needle shaft
r	Radius of the fixed curvature of the needle in the Unicycle model
$RMSE_{M_i}$	Root-mean-squared error of the M_i model
t	Time
v	Insertion speed of the needle
$v(t, z)$	Deflection of the needle
v_z	Wheel speed of the needle
XYZ	Frame of the needle tip

Chapter 1

Introduction

Robotic surgery, also called robot-assisted surgery, allows doctors to perform many types of complex procedures with more precision, flexibility, and control than is possible with conventional techniques. Robotic surgery is usually associated with minimally invasive surgical procedures performed through tiny incisions. Using robotic surgery, surgeons can perform delicate and complex procedures that may be difficult or impossible with other methods. Often, robotic surgery makes minimally invasive surgery possible. The benefits of minimally invasive surgery include fewer complications, less pain and blood loss, shorter hospital stay, a quicker recovery and less noticeable scars. Nowadays, the da Vinci Surgical System (Figure 1.1) is the most advanced robotic system for minimally invasive surgery. Its technical characteristics make it usable in various sectors, from urology to gynaecology, from thoracic surgery to general surgery. The surgeon, seated at a computer console near the operating table, moves the robot's arms, associated with the endoscopic instruments introduced through small incisions. The console gives the surgeon a high-definition, 3D view of the surgical site.

1.1 Autonomy in Robotic Surgery

Recent research in robotic-assisted minimally invasive surgery mostly focuses on autonomous systems that perform repetitive surgical steps, such as suturing, ablation, and needle insertions. Leaving monotonous tasks to the robot could allow surgeons to concentrate on the more mentally demanding aspects of the procedure. Despite having all the necessary mechanical and computational capabilities, most surgical robots do not currently carry out any autonomous tasks due to technical and legal constraints such as the complexity of the surgical environments (patient-specific variations), perception and sensing limitations (lack of real-time feedback required for precise operations) and some ethical considerations about patient consent, trust in automated systems.

Six increasing levels are identified in a surgical system's autonomy grade classification [3].

- Level 0: Systems at level-0 are not autonomous, the motion of the robot
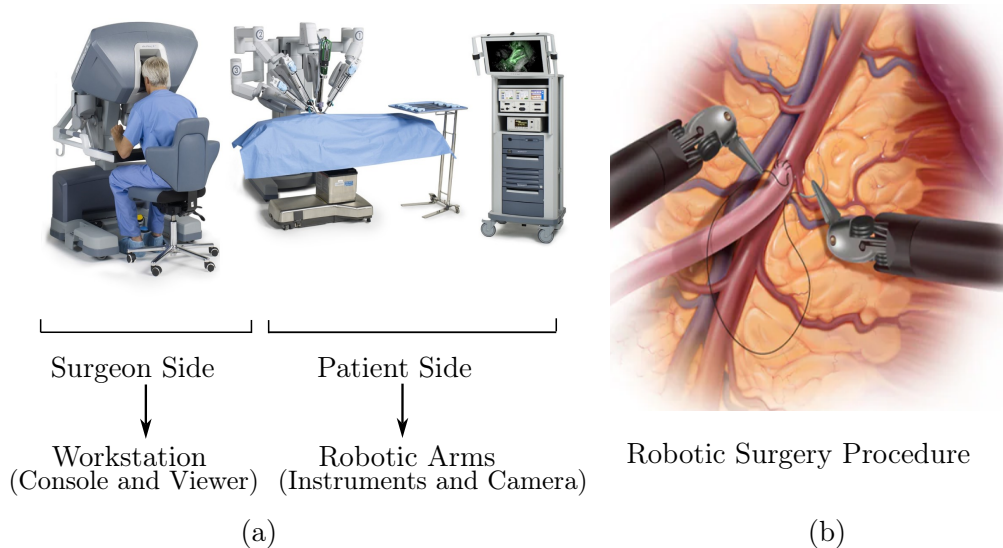
Figure 1.1: (a) The da Vinci Surgical System. Image adapted from [1]; (b) 3D view of the surgical site during a robotic procedure.

is controlled exclusively by the surgeon, and no supports or constraints are provided.

- Level 1: Systems classified within Level-1 "Robot Assistance" are capable of interacting with the surgeon to guide or support the execution of a particular task. The assistance provided consists of either active constraints to guide the surgeon's motion or a virtual fixture to enhance the surgical site visualisation.

- Level 2: Systems classified within Level-2 "Task Autonomy" are capable of accomplishing specific surgical tasks upon specifications provided by the surgeon.

- Level 3: Systems categorised in Level-3 "Conditional Autonomy" are provided with perceptual capabilities to understand the surgical scenario, to plan and execute a specific task and to update the plan during execution.

- Level 4: Surgical systems at Level-4 "High Autonomy" can interpret preoperative and intra-operative information, devise an interventional plan composed by a sequence of tasks, and execute it autonomously, re-planning if necessary.

- Level 5: Surgical systems at Level-5 "Full autonomy" can perform an entire surgery. This can be construed broadly as a system capable of all procedures performed.
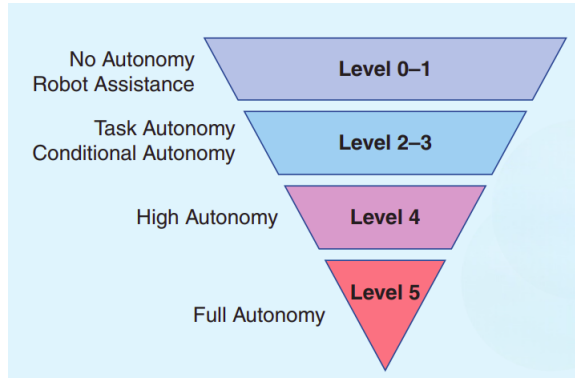
Figure 1.2: Different levels of autonomy as mapped to robotic surgery. Image adapted from [2].

The introduction of autonomy involves the development of systems with advanced perception, reasoning, and motion planning skills as well as specific approaches for controlling interaction with the external environment. Due to the complex nature of the patient's anatomical environment, these tasks are extremely difficult in the surgical field. Recently, several projects have been carried out to provide surgical robots with a certain level of autonomy, as exemplified by ARS (Autonomous Robotic Surgery Project)[1] and its proof of concept, PROST (The Autonomous Prostate Biopsy Project)[2]. This thesis is integrated within both ARS and PROST Projects. We are focusing on controlling the forces exchanged between the patient and the surgical instrument to ensure the accuracy and the safety of the procedure in two areas: Minimally Invasive Robotic Surgery (MIS) with da Vinci Research Kit (dVRK) and Prostate Biopsy. The following section describes in detail both European projects.

1.2 European Projects on Autonomy in Robotic Surgery

1.2.1 The Autonomous Robotic Surgery Project

The ARS European Project aims to develop methodologies that will enable the execution of surgical intervention by a robotic system with complete autonomy. The goal of the ARS project is the derivation of a unified framework for the autonomous execution of robotic tasks in challenging environments in which accurate performance and safety are of paramount importance. The framework for autonomous robotic surgery will include five main research objectives. The

---

first will address the analysis of the robotic surgery data set to extract action and knowledge models of the intervention. The second objective will focus on planning, consisting of instantiating the intervention models to a patient-specific anatomy. The third objective is to develop methods for the real-time control of the surgical instruments during the execution of the intervention. The fourth research objective will focus on real-time reasoning to assess the intervention state and the overall surgical situation. Finally, the last research objective will address autonomous surgical robotic capabilities' verification, validation, and benchmarking. Surgical instruments have undergone great innovation over time, from short and rigid instruments such as forceps, scissors, spreaders, scalpels, etc., to long and more flexible robotic laparoscopic instrumentation that allows the replication of human movement through an articulation (wrist) positioned at the tooltip.

(a)   (b)
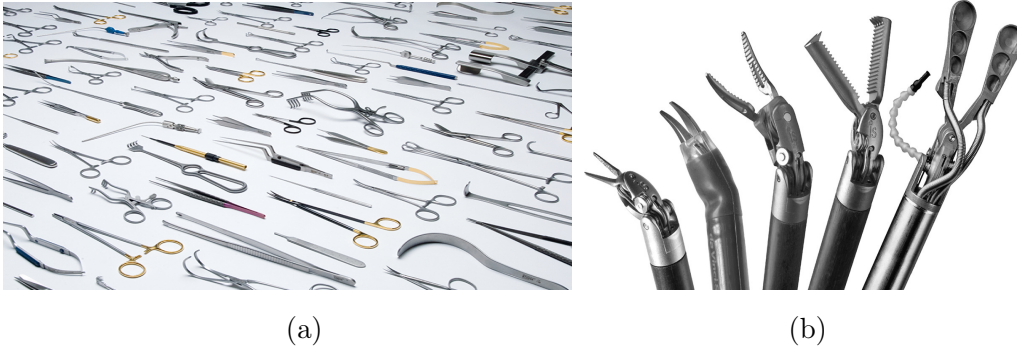
Figure 1.3: (a) Open-Surgery Instruments; (b) The da Vinci Surgical System Laparoscopic Instruments.

1.2.2   The Autonomous Prostate Biopsy Project

The PROST European PoC proposal aims at demonstrating the technical, clinical and economic feasibility of autonomous prostate biopsy execution, by applying the technologies developed by the ERC project ARS to a robotic prostate biopsy system. The project is made feasible by two enabling factors: the ongoing ERC project ARS which is developing sensing and control architecture for autonomous surgical robots, and the availability of a prototype of a robot for prostate biopsy developed with a grant by the Italian Ministry of Foreign Affairs and International Cooperation. Prostate cancer is the second most common cancer in men, early diagnosis is key to improve patients' therapeutic path and reduce the mortality rate. Prostate biopsy is a good candidate for applying automation in clinical practice since it is a rather simple procedure, carried out on more than 1 Mil/year patients in Europe, and still affected by a diagnostic error higher than 30%. due to the difficulty in identifying the location of the lesion and in manually aiming the biopsy gun. The diagnostic tool developed by PROST Project will allow the autonomous robotic execution of the biopsy: a new paradigm that will turn a subjective and operator-dependent procedure into a safer and more

accurate procedure. The clinical process to identify a possible carcinoma involves a blood sampling with the evaluation of the PSA enzyme followed by a digital rectal examination in which the doctor surrounds the gland in search of surface abnormalities. To have a final diagnosis, a histopathological evaluation is made on the samples taken during the prostate biopsy. There are two types of biopsies: transrectal and transperineal. Although the first is simpler and more intuitive PROST device performs a transperineal biopsy in order to limit complications such as sepsis. The standard procedure consists of 12 samples and other target samples chosen from Magnetic Resonance Imaging (MRI) images. The needle is inserted into the cannula and then "fired" into various areas.
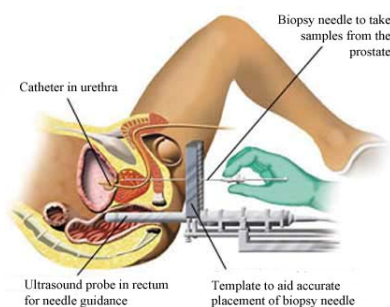
Figure 1.4: Transperineal Prostate Biopsy.

1.3 Contributions and structure of the thesis

This thesis contributes to the ambitious goal of achieving surgical autonomy in robotic surgery by providing feedback on the interaction between instruments and the anatomical environment. Feedback allows surgeons to control their movements and actions during surgery precisely. This is especially important in delicate procedures where even slight deviations can cause significant harm. Excessive force can damage tissues, while insufficient force may be ineffective. Feedback helps manage the amount of force applied, reducing the risk of tissue damage. In robotic surgery, where the surgeon is not directly in contact with the tissues, feedback is essential to simulate the tactile sensation and ensure appropriate force application.

Two different robotic systems are considered: da Vinci Surgical System and a robotic device to perform prostate biopsy. Starting from the study of the mathematical models of tools available in robotics, we developed methodologies in order to measure and control the forces exchanged between the instrument and organs involved during a procedure. During the robotic laparoscopic procedure, the surgeon decides to perform certain movements based on visual information and his experience, but he has not any physical perception of the reaction forces between the laparoscopic tool and the tissues. In this thesis, we take advantage of the flexibilities within the laparoscopic tool to control interaction forces with human

tissues.

During a prostate biopsy, the estimation of the needle deflection during the insertion is a problem that needs to be addressed in order to ensure accurate needle tip placement, especially when considering the small dimension of the organ and the possibility of taking tissue samples in the most distal areas. Given the high flexibility of prostate biopsy needles, important deflections can indeed be observed due to the tissue reaction forces acting on the bevelled tip during insertion (Figure 1.5).
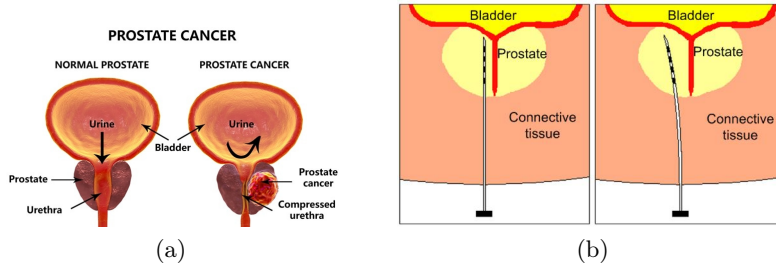
Figure 1.5: (a)Prostate Cancer (b) Bevelled-tip needle deflection.

The thesis is divided into two distinctive parts. In part I, we focus on exploiting the flexible nature of surgical links for force control. Chapter 2 shows that the force control, based on feedback from the deformation at the base of the link, is passive with respect to the surrounding environment. Using a continuum mechanics model that considers the dynamics of the system ensures that the force control is able to maintain stability in any passive environment. In chapter 3, we present a software library that can generate nth-order lumped models to accurately approximate the dynamics of flexible links characterized by certain inertia, stiffness, and damping parameters under the action of non-collocated feedback. The passivity and stability of these models are analysed considering robotic surgery as a reference application. In part II of the thesis, we focus on modelling the interaction forces between a biopsy needle and tissues in the prostate area. We propose an experimental comparison to evaluate the accuracy of the kinematic models available in the literature. Kinematic models should then be compared with finite elements models and approximate quasi-static mechanical models. The final goal is to provide a comprehensive and detailed assessment of the accuracy of different models within the needle-prostate tissue interaction. Finally, Chapter 5 summarizes the results of this thesis and proposes future extensions for both parts.

Part I

Flexible Links and Force Control

Chapter 2

Force control exploiting link flexibility: passivity considerations

Structural flexibility may appear in different robotic systems. It can emerge as a consequence of certain design requirements, such as lightweight, safety or minimal encumbrance [4], or it can be added on purpose to absorb impacts and reduce mechanical stress, like in the case of certain legged robots [5]. Once flexibility is there, one needs to deal with it and, if possible, take advantage of it. Some results in the last three decades of force control research have highlighted that flexibilities can help to improve stability margins [6, 7, 8]. These results are based on lumped models: series elastic actuators [9] and, more in general, series elastic systems [10] represent a main example. In particular, it has been proved that collocated flexibilities and collocated force feedback allow higher gain stability margins. In turn, higher force feedback gains allow to better mask the inherent actuator dynamics, including inertia, friction and stiction phenomena leading to enhanced performance and transparency [8, 7, 6]. With the rise of series elastic actuation flexibilities are deliberately introduced at the joint level by adding a (lumped) deformable element between the motor and the link, leading to accurate force sensing and control at each robot joint [7, 9, 11]. Indeed, the deformation of such flexible element can be used to provide collocated force feedback and may lead to improve the so-called accuracy-robustness tradeoff [12]. As a matter of fact, several passive controllers have been proposed for series elastic actuators guaranteeing a stable interaction with any passive environment [13, 14].

Interestingly, it is possible to achieve a similar advantage by exploiting different forms of flexibilities, appearing at the link level instead of at the joint level [15, 16]. Unfortunately, link flexibility is harder to model in comparison to joint flexibility as it involves a more complex formalism from continuum mechanics theory. Probably due to these modelling complexities, the idea of exploiting link flexibilities has received little attention in the force control literature. The few existing works are limited to simulation studies [17], or they present simple exper-

imental results without considering a solid theoretical analysis [18], or they use approximated lumped models [19, 20, 16, 21, 22].

Nevertheless, different kinds of robotic systems exhibit inherent link flexibilities, from medical to collaborative robotics. In surgical robots, flexibilities are unavoidable due to the thin diameter of the laparoscopic tool used for minimally invasive surgery [23]; in certain collaborative robots, flexibilities can be due to safety requirements, which leads to preferred lightweight structures [4]; in exoskeletons, link flexibilities can be added on purpose to reduce kinematic misalignments [24]. All these systems can take advantage of force control technology, which in turn can take advantage of flexibilities already embedded in the robot structure. Unfortunately, a solid theoretical foundation to exploit link flexibilities in robot force control does not exist yet, and the objective of this work is to start filling this gap. This Chapter considers force control based on feedback from link deformation and investigates related passivity properties, considering a continuum mechanics model expressing the link dynamics. Even if some results exist on passive control of distributed systems [25, 26, 27], they are not specifically linked to force control applications. We recall that passivity represents a fundamental requirement in interaction control since the high uncertainties that typically characterize the environment affect the closed-loop stability. Passivity is the only tool able to guarantee stability in any passive environment. The discussion proposed in this Chapter could be applicable to a wide class of robotic systems with structural flexibilities, such as lightweight collaborative robots, industrial and medical exoskeletons, or medical robots. In this Chapter, the term force control is intended in a general sense, including both force and torque feedback.

The Chapter is organised as follows: Section 2.1 summarizes the past work on flexible link and force control and motivates our choice to focus on single joint-link modules. Sections 2.2 and Appendix 2.6 report continuum mechanics models for a flexible link interacting with a generic environment under small and large joint angle assumptions, respectively. In section 2.3, force control passivity is proven with respect to the environment port and considering feedback from link deformation measured at the link base while in Appendix 2.7 trunked lumped approximants of the system are reported and passivity conditions for collocated force feedback are calculated. In Section 2.4 and Appendix 2.8, a high-order lumped approximation of the continuum mechanics model is built up to validate results using numerical examples. Section 2.5 reports our conclusions and plans for future work.

The results of this chapter are reported in "Force Control Exploiting Link Flexibility: Passivity Considerations" submitted to "IEEE Transactions on Automatic Control".

2.1   Background

2.1.1   Flexible links in force control applications

Few attempts to exploit link flexibility in force control applications appeared in
the literature. One example is the work by Garcia [18], which describes exper-
iments using link deformation, measured at the link base, as a feedback signal
to close a force control loop. The work is only empirical and reports force con-
trol experiments without theoretically proving stability. Instead, a theoretical
stability analysis is reported in the work by Feliu-Talegon [28] where a hybrid
position-force controller is proposed aiming at controlling the tip position (in free
motion) and the force exerted on the environment (in constrained motion). An
interesting point about this work is that stability analysis considers a numerable
set of environments, thus guaranteeing robustness to environment uncertainties.
Robustness to environment uncertainty is indeed a fundamental feature in force
control applications since the environment is, in most cases, unknown or at least
uncertain. A critical point in the work by Feliu-Talegon is that the considered
link model is trunked to the second order. Such approximation leads in practice
to a lumped model that is equivalent to those used for series elastic actuation
and cannot account for the continuum nature of flexible links, which should be
formalised as a partial differential equation (PDE). A similar trunked model was
used in our previous work, where we described the concept with the term Series
Elastic Link [15] to highlight the analogy with series elastic actuation. The work
by Morita [17] is the only example we could find where a PDE model is consid-
ered for the link within a force feedback application. Unfortunately, the proposed
system does not aim to control forces; it presents a position control architecture
where force feedback from link deformation, measured at the link base, is just
used to damp link oscillations. While the works reported so far consider force
control applications on a single flexible link, the work by Malzahn represents the
only example we could find on multiple-link robots. Unfortunately, the consid-
ered link model is again trunked to the second order and does not account for
the continuum nature of the system [16, 29, 30, 31]. Quite interestingly, even if
Malzahn has been the first to exploit elastic link deformations on a multi-DOF
robot, his main contribution is related to decentralized single-DOF controllers "to
shape the closed loop dynamics of each joint-link module," leading to simplify the
complex multi-elastic-body model. In other words, Malzahn stated that if each
joint-link subsystem can be considered an ideal torque source, thanks to quality
force control, the whole manipulator dynamics could be approximated to simpler
equations. Therefore, advancing the control of single joint-link subsystems to
better approximate ideal torque sources is of fundamental importance. Starting
from this consideration, our contribution focuses on a single joint-link module,
and the continuum nature of links is considered within a force control application
and passivity arguments are introduced.

2.1.2 Existing models for Flexible links

Most of the existing models for flexible links come from position control literature where the main objective is to control the link end-point position while suppressing vibrations due to the link dynamics [32, 33, 34, 35, 36, 37, 38]. All existing models are based on the small link deformation assumption. In addition, these models assume small joint displacements to obtain an overall linear description of the link dynamics. Two main modelling approaches can be found. A first class of approaches (time-space models) use partial differential equations along time and space coordinates derived using the Lagrangian formalism [39, 17, 40, 41, 36, 42]. A second class of approaches (frequency models) consider linearized models along a defined spatial coordinate and use time-space separation to define the frequency relation between the motor input torque and the position (or orientation) at a selected spatial coordinate [43, 44, 45, 46, 47, 48, 49, 50, 19, 51]. This class introduces a further approximation by only considering the dominant system dynamics expressed in terms of dominant poles and zeros. The infinite-order expression derived from time-space models is often trunked to the second order, leading to the approximation discussed in section 2.1.1, which is equivalent to a series elastic actuation model [15]. Rarely, higher-order models are used, trunking to the fourth or sixth order [52, 53]. In conclusion, the first class of models (time-space models) seems to provide the most accurate description of flexible links subject to small deformations, and these are the kinds of models considered in this work. In particular, we take inspiration from the model in [17], which is, among the few, the only one including external forces acting on the link.

2.2 System Modelling
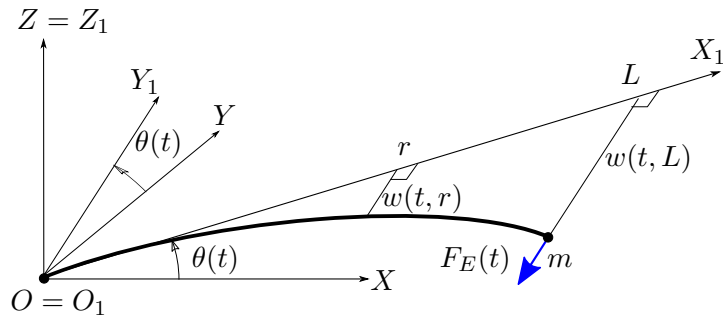
Figure 2.1: Flexible link clamped to a revolute joint

In this section, we use the Lagrangian formalism to derive the motion equations for the joint-link module represented in Figure 2.1. It includes a flexible link clamped to a revolute joint, rotating on Z-axis, driven by an electric motor in such a way that the motor torque τ_m and the external force F_E produce a link bending deformation laying on the XY plane. Since only the planar motion of the link is considered, even the external F_E is taken into account. Reference

$\{O, XYZ\}$ represents the fixed frame, while $\{O_1, X_1Y_1Z_1\}$ is the body frame with $O = O_1$. However, since θ is assumed small, as in [17], the two frames coincide. The quantities $\theta(t)$, $\tau_m(t)$, and J_m represent the angle of rotation of the motor, the torque developed by the motor, and the moment of inertia of the motor. The function $w(t,r)$ denotes the link bending displacement at a spatial coordinate r expressed in the motor body frame. The link has length L, uniform mass density ρ per unit length, and uniform bending stiffness EI where E is Young's modulus and I is the second moment of area. Torsional and axial stiffness are assumed to be infinite. The interaction with the environment generates an external force $\boldsymbol{F_E}$ applied at the link endpoint. According to the continuum mechanics theory, since the force $\boldsymbol{F_E}$ lies on the XY plane, it can be expressed as

$$\boldsymbol{F_E} = \begin{bmatrix} F_{E_x} & F_{Ey} & 0 \end{bmatrix}^T. \tag{2.1}$$

Also, since the force component considered link bending is perpendicular to the link and considering small θ, it can be obtained considering the third derivative of $w(t,r)$ with respect to the space r computed at the tool endpoint position.

$$\boldsymbol{F_{E_\perp}} = \begin{bmatrix} 0 & EIw_E'''(t) & 0 \end{bmatrix}^T \tag{2.2}$$

with $w_E(t) = w(t,L)$. This is the only component affecting the in-plane link bending. In our notation, the symbols $(\cdot)$ and $(')$ represent the time and the space derivative, respectively. The bold symbols represent the vectors, while the normal symbols represent the scalar and the vector modules. As mentioned before, the model assumptions for the motion are small link deformations $w(t,r)$ and small joint angle displacement $\theta(t)$, as in [17]. The boundary conditions are $w(t,0) = 0$ and $w'(t,0) = 0$, and no torque applied at the link endpoint $EIw''(t,L) = 0$. These conditions are applied to derive the motion equations because the link is considered as a cantilever beam fixed at the rotational joint. By considering these assumptions, the tip position vector $\boldsymbol{P}$ can be expressed as

$$\boldsymbol{P} = \begin{bmatrix} L & L\theta(t) - w_E(t) & 0 \end{bmatrix}^T \tag{2.3}$$

Similarly, the vector $\boldsymbol{r}$, which represents the position of an infinitesimal portion of the link at the spatial coordinate r, can be expressed as

$$\boldsymbol{r} = \begin{bmatrix} r & r\theta(t) - w(t,r) & 0 \end{bmatrix}^T. \tag{2.4}$$

To derive the motion equations using the Lagrangian formalism, one needs to consider the total kinetic energy τ_{TOT} and the potential energy ν, which are given by

$$\tau_{\text{TOT}} = \tau_{\text{motor}} + \tau_{\text{link}} + \tau_{\text{tip}}$$

$$\tau_{\text{motor}} = \frac{1}{2} J_m \dot{\theta}^2(t)$$

$$\tau_{\text{link}} = \frac{1}{2} \int_0^L \rho \dot{\boldsymbol{r}}^T \dot{\boldsymbol{r}} \, dr \qquad (2.5)$$

$$\tau_{\text{tip}} = \frac{1}{2} m \dot{\boldsymbol{P}}^T \dot{\boldsymbol{P}}$$

$$\nu = \frac{1}{2} \int_0^L EI w''^2(t, r) \, dr$$

τ_{motor}, τ_{link} and τ_{tip} are the kinetic energies of the three components of the system: the motor, the link, and the mass m placed on the tip of the link on which the environment force $\boldsymbol{F}_E$ acts. The equations of motion for the system in Figure 2.1 are derived, given the Lagrangian formulation, by minimising the action functional $\mathcal{F}$. Let's construct the Lagrangian equation as

$$\mathcal{L} = \tau_{\text{TOT}} - \nu$$

$$\mathcal{L} = \frac{1}{2} J_m \dot{\theta}^2 + \frac{1}{2} \int_0^L \rho \dot{\boldsymbol{r}}^T \dot{\boldsymbol{r}} \, dr + \frac{1}{2} m \dot{\boldsymbol{P}}^T \dot{\boldsymbol{P}} - \frac{1}{2} \int_0^L EI w''^2 \, dr \qquad (2.6)$$

where

$$\dot{\boldsymbol{r}}^T \dot{\boldsymbol{r}} = \begin{bmatrix} 0 & r\dot{\theta}(t) - \dot{w}(t,r) & 0 \end{bmatrix} \begin{bmatrix} 0 \\ r\dot{\theta}(t) - \dot{w}(t,r) \\ 0 \end{bmatrix} \qquad (2.7)$$

and

$$\dot{\boldsymbol{P}}^T \dot{\boldsymbol{P}} = \begin{bmatrix} 0 & L\dot{\theta}(t) - \dot{w}_E(t) & 0 \end{bmatrix} \begin{bmatrix} 0 \\ L\dot{\theta}(t) - \dot{w}_E(t) \\ 0 \end{bmatrix} \qquad (2.8)$$

The action functional $\mathcal{F}$ is defined as the time integral of the Lagrangian $\mathcal{L}$ on a specific trajectory

$$\mathcal{F} = \int_{t_0}^{t_1} \int_0^L \mathcal{L}(r, \theta(t), w(t,r), \dot{\theta}(t), \dot{w}(t,r), w''(t,r)) \, dr \, dt$$

$$= \int_{t_0}^{t_1} \int_0^L \frac{J_m}{2L} \dot{\theta}^2 + \frac{\rho}{2}(r\dot{\theta} - \dot{w})^2 + \frac{m}{2L}(L\dot{\theta} - \dot{w}_E)^2 - \frac{EI}{2} w''^2 \, dr \, dt \qquad (2.9)$$

According to Hamilton's principle, motion equations are obtained by introducing small perturbations on the states $\theta + \varepsilon v$ and $w + \varepsilon z$ for any $\varepsilon \in \mathbb{R}$, and these must be zero at the endpoints of the trajectory. The perturbations produce a variation $\delta\mathcal{F}$ of the functional action given by:

$$0 = \delta\mathcal{F} = \frac{d}{d\varepsilon}\bigg|_{\varepsilon=0} \int_{t_0}^{t_1} \int_0^L \frac{J_m}{2L}(\dot{\theta} + \varepsilon \dot{v})^2 + \frac{\rho}{2}(r(\dot{\theta} + \varepsilon \dot{v}) +$$

$$-(\dot{w} + \varepsilon \dot{z}))^2 + \frac{m}{2L}(L(\dot{\theta} + \varepsilon \dot{v}) - (\dot{w}_E + \varepsilon \dot{z}_E))^2 + \qquad (2.10)$$

$$-\frac{EI}{2}(w'' + \varepsilon z'')^2 \, dr \, dt$$

$$0 = \delta\mathcal{F} = \int_{t_0}^{t_1} \int_0^L \frac{J_m}{L}\dot{\theta}\dot{v} + \rho(r\dot{\theta} - \dot{w})(r\dot{v} - \dot{z}) + \\ + \frac{m}{L}(L\dot{\theta} - \dot{w}_E)(L\dot{v} - \dot{z}_E) - EIw''z'' \, dr \, dt \tag{2.11}$$

Since Hamilton's principle requires that $\delta\mathcal{F}$ is zero for all possible perturbations ε, both perturbations are set to 0, and integrals are computed to obtain the equations of motion. As a first step, considering $z = 0$ in Eq. (2.11), one can obtain

$$\int_{t_0}^{t_1} \int_0^L \underbrace{\frac{J_m}{L}\dot{\theta}\dot{v}}_{\delta\mathcal{F}_A} + \underbrace{\rho r(r\dot{\theta} - \dot{w})\dot{v}}_{\delta\mathcal{F}_B} + \underbrace{m(L\dot{\theta} - \dot{w}_E)\dot{v}}_{\delta\mathcal{F}_C} \, dr \, dt. \tag{2.12}$$

Then, integrals $\delta\mathcal{F}_A$, $\delta\mathcal{F}_B$ and $\delta\mathcal{F}_C$ are computed by parts

$$\delta\mathcal{F}_A = \int_{t_0}^{t_1} \frac{J_m}{L}\dot{\theta}\dot{v} \, dt \overset{\text{P.I}}{=} -\int_{t_0}^{t_1} \frac{J_m}{L}\ddot{\theta}v \, dt$$

$$\delta\mathcal{F}_B = \int_{t_0}^{t_1} \rho r(r\dot{\theta} - \dot{w})\dot{v} \, dt \overset{\text{P.I}}{=} -\int_{t_0}^{t_1} \rho r(r\ddot{\theta} - \ddot{w})v \, dt \tag{2.13}$$

$$\delta\mathcal{F}_C = \int_{t_0}^{t_1} m(L\dot{\theta} - \dot{w}_E)\dot{v} \, dt \overset{\text{P.I}}{=} -\int_{t_0}^{t_1} m(L\ddot{\theta} - \ddot{w}_E)v \, dt$$

$$\int_{t_0}^{t_1} \int_0^L \underbrace{-\left[\frac{J_m}{L}\ddot{\theta} + \rho r(r\ddot{\theta} - \ddot{w}) + m(L\ddot{\theta} - \ddot{w}_E)\right]}_{=0} v \, dr \, dt \tag{2.14}$$

to get the following equation

$$\frac{J_m}{L}\ddot{\theta} + \rho r(r\ddot{\theta} - \ddot{w}) + m(L\ddot{\theta} - \ddot{w}_E) = 0 \tag{2.15}$$

As a second step, considering $v = 0$ in Eq. (2.11), the following expression is obtained

$$\int_{t_0}^{t_1} \int_0^L \underbrace{-\rho(r\dot{\theta} - \dot{w})\dot{z}}_{\delta\mathcal{F}_D} - \underbrace{\frac{m}{L}(L\dot{\theta} - \dot{w}_E)\dot{z}_E}_{\delta\mathcal{F}_E} - \underbrace{EIw''z''}_{\delta\mathcal{F}_F} \, dr \, dt \tag{2.16}$$

Then, integrals $\delta\mathcal{F}_D$, $\delta\mathcal{F}_E$ and $\delta\mathcal{F}_F$ are computed by parts

$$\delta\mathcal{F}_D = -\int_{t_0}^{t_1} \rho(r\dot{\theta} - \dot{w})\dot{z}\,dt$$

$$\stackrel{\text{P.I}}{=} \int_{t_0}^{t_1} \rho(r\ddot{\theta} - \ddot{w})z\,dt$$

$$\delta\mathcal{F}_E = -\int_{t_0}^{t_1} \frac{m}{L}(L\dot{\theta} - \dot{w}_E)\dot{z}_E\,dt$$

$$\stackrel{\text{P.I}}{=} \int_{t_0}^{t_1} \frac{m}{L}(L\ddot{\theta} - \ddot{w}_E)z_E\,dt$$

$$\delta\mathcal{F}_F = -\int_0^L EIw''z''\,dr$$

$$\stackrel{\text{P.I}}{=} \int_0^L \frac{F_{E_\perp}}{L}z_E - EIw''''z\,dr$$

$$(2.17)$$

$$\int_{t_0}^{t_1}\int_0^L \underbrace{\left[\rho(r\ddot{\theta} - \ddot{w}) - EIw''''\right]}_{=0} z +$$

$$\underbrace{\left[\frac{F_{E_\perp}}{L} + \frac{m}{L}(L\ddot{\theta} - \ddot{w}_E)\right]}_{=0} z_E\,dr\,dt$$

$$(2.18)$$

and the following equations of motion are obtained

$$\rho(r\ddot{\theta} - \ddot{w}) - EIw'''' = 0 \qquad\qquad (2.19)$$

$$\frac{F_{E_\perp}}{L} + \frac{m}{L}(L\ddot{\theta} - \ddot{w}_E) = 0 \rightarrow m(L\ddot{\theta} - \ddot{w}_E) = -F_{E_\perp} \qquad (2.20)$$

Substituting the equation of motion for the link (2.19) and the boundary condition of the tip mass (2.20) in the equation of motion for the motor (2.15), one can obtain

$$\int_0^L \underbrace{\frac{J_m}{L}\ddot{\theta}}_{M_1} + \underbrace{rEIw'''' - F_{E_\perp}}_{M_2}\,dr = \int_0^L \underbrace{\frac{\tau_m}{L}}_{M_3}\,dr. \qquad (2.21)$$

Then, the integrals M_1, M_2 and M_3 are computed

$$M_1 = \int_0^L \frac{J_m}{L} \ddot{\theta} \, dr = J_m \ddot{\theta}$$

$$M_2 = \int_0^L r E I w'''' \, dr - \int_0^L F_{E_\perp} \, dr$$

$$\overset{\text{P.I}}{=} E I r w''' \Big|_0^L - E I \int_0^L w''' \, dr - F_{E_\perp} L$$

$$= F_{E_\perp} L - E I w'' \Big|_0^L - F_{E_\perp} L$$

$$= -\underbrace{E I w_E''}_{=0} + E I w_0'' = E I w_0''$$

$$M_3 = \int_0^L \frac{\tau_m}{L} \, dr = \tau_m$$

(2.22)

and the motion equations are obtained as

$$J_m \ddot{\theta}(t) + E I w''(t,0) = \tau_m(t) \tag{2.23}$$

$$\rho(r\ddot{\theta}(t) - \ddot{w}(t,r)) - E I w''''(t,r) = 0 \tag{2.24}$$

$$m(L\ddot{\theta}(t) - \ddot{w}_E(t)) = -F_{E_\perp}(t) \tag{2.25}$$

where (2.23) represents the motor dynamics, (2.24) the link dynamics, (2.25) the end-point mass dynamics and F_E is the module of $\boldsymbol{F_E}$. For the sake of completeness, Appendix 2.6 reports the derivation of the same equation by removing the small joint angle assumption, which leads to a more complex formulation.

2.3 Passivity Analysis

Now that the system model has been derived, the following theorem considers the application of a proportional force controller in the form

$$\tau_m(t) = -k_p E I w''(t,0), \quad k_p > -1 \tag{2.26}$$

where the term $E I w''(t,0)$ represents the torque measured at the link clamping point, which is used as feedback signal. The theorem proves that such controller ensures passivity at the environment port $(\boldsymbol{F_E}, \dot{\boldsymbol{P}})$.

Theorem 1. *The PDE model (2.23), (2.24) and (2.25) controlled by the control law (2.26), where k_p is a proportional gain and $E I w''(t,0)$ the torque measured at the link clamping point, is passive at the port $(\boldsymbol{F_E}, \dot{\boldsymbol{P}})$*

Proof: Let us consider as Lyapunov candidate function $\mathcal{V}$ the summation of the system kinetic and potential energy.

$$\mathcal{V} = \frac{1}{2} \alpha J_m \dot{\theta}^2 + \frac{1}{2} \int_0^L \rho \dot{\boldsymbol{r}}^T \dot{\boldsymbol{r}} \, dr + \frac{1}{2} \int_0^L E I w''^2 \, dr \tag{2.27}$$

with $\alpha = \frac{1}{k_p+1}$. Note that since $k_p > -1$, then $0 < \alpha < 1$. Differentiating the Lyapunov candidate function with respect to t yields

$$\dot{\mathcal{V}} = \alpha J_m \dot{\theta}\ddot{\theta} + \int_0^L \rho \dot{\boldsymbol{r}}^T \ddot{\boldsymbol{r}} \, dr + \int_0^L EIw'' \dot{w}'' \, dr \qquad (2.28)$$

where

$$\ddot{\boldsymbol{r}} = \begin{bmatrix} 0 & r\ddot{\theta}(t) - \ddot{w}(t,r) & 0 \end{bmatrix}^T \qquad (2.29)$$

and

$$\dot{\boldsymbol{r}}^T \ddot{\boldsymbol{r}} = \begin{bmatrix} 0 & r\dot{\theta}(t) - \dot{w}(t,r) & 0 \end{bmatrix} \begin{bmatrix} 0 \\ r\ddot{\theta}(t) - \ddot{w}(t,r) \\ 0 \end{bmatrix} \qquad (2.30)$$

The link equation (2.24) is substituted in the Lyapunov candidate equation (2.28)

$$\dot{\mathcal{V}} = \alpha J_m \dot{\theta}\ddot{\theta} + \underbrace{\int_0^L EIrw''''\dot{\theta}}_{\dot{\mathcal{V}}_A} + \underbrace{\int_0^L EIw''\dot{w}'' \, dr}_{\dot{\mathcal{V}}_B} + \\ - \underbrace{\int_0^L EI\dot{w}w'''' \, dr}_{\dot{\mathcal{V}}_C} \qquad (2.31)$$

and integrals $\dot{\mathcal{V}}_A$, $\dot{\mathcal{V}}_B$, $\dot{\mathcal{V}}_C$ are computed by parts

$$\dot{\mathcal{V}}_A = \int_0^L EIrw''''\dot{\theta} \, dr \overset{\text{P.I}}{=} EIL\dot{\theta}w'''_E + EIw''_0\dot{\theta}$$

$$= F_{E_\perp}L\theta + EIw''_0\dot{\theta}$$

$$\dot{\mathcal{V}}_B = \int_0^L EIw''\dot{w}'' \, dr \overset{\text{P.I}}{=} EI[[w''\dot{w}']_0^L + \qquad (2.32)$$

$$- \underbrace{\int_0^L EIw'''\dot{w}' \, dr}_{\dot{\mathcal{V}}_D}]$$

Let's call $\dot{\mathcal{V}}_D$ the last term of $\dot{\mathcal{V}}_B$ and, again, let's calculate it by parts

$$\dot{\mathcal{V}}_D = \int_0^L EIw'''\dot{w}' \, dr \overset{\text{P.I}}{=} EI[[w'''\dot{w}]_0^L - \int_0^L EI\dot{w}w'''' \, dr]$$

$$= EIw'''_E\dot{w}_E - \underbrace{\int_0^L EI\dot{w}w'''' \, dr}_{\dot{\mathcal{V}}_C} \qquad (2.33)$$

It can be noted that the last term of $\dot{\mathcal{V}}_D$ equals $\dot{\mathcal{V}}_C$, so substituting $\dot{\mathcal{V}}_D$ in $\dot{\mathcal{V}}_B$ yields to

$$\dot{\mathcal{V}}_B = -EIw'''_E \dot{w}_E + EI \int_0^L \dot{w}w'''' \, dr$$
$$= -F_{E_\perp} \dot{w}_E + \underbrace{EI \int_0^L \dot{w}w'''' \, dr}_{\dot{\mathcal{V}}_C} \tag{2.34}$$

Then, replacing $\dot{\mathcal{V}}_A, \dot{\mathcal{V}}_B, \dot{\mathcal{V}}_C$ in $\dot{\mathcal{V}}$, it is possible to cancel out $\dot{\mathcal{V}}_C$ leading to

$$\dot{\mathcal{V}} = \alpha J_m \dot{\theta}\ddot{\theta} + F_{E_\perp} L\dot{\theta} + EIw''_0 \dot{\theta} - F_{E_\perp} \dot{w}_E. \tag{2.35}$$

Finally, by substituting the motor motion (2.23)

$$\dot{\mathcal{V}} = \alpha\dot{\theta}(\tau_m - EIw''_0) + F_{E_\perp} L\dot{\theta} + EIw''_0 \dot{\theta} - F_{E_\perp} \dot{w}_E \tag{2.36}$$

and then the control law (2.26), one has

$$\dot{\mathcal{V}} = F_{E_\perp}(L\dot{\theta} - \dot{w}_E) = \boldsymbol{F_{E_\perp}}^T \dot{\boldsymbol{P}} \tag{2.37}$$

since, due to the Poisson equation, $\dot{\boldsymbol{P}}$ is perpendicular to $\boldsymbol{P}$, $(\boldsymbol{F_{E_\perp}}^T, \dot{\boldsymbol{P}})$ is equivalent to $(\boldsymbol{F_E}, \dot{\boldsymbol{P}})$ and passivity at the environment port is proved. ∎

We can conclude that Theorem 1 proves the passivity of proportional force feedback (Eq. 2.26) with respect to the environment port. This means that if and only if any passive environment is coupled to the system, stability is always retained [54]. This is a novel approach in which force control passivity has been proven using feedback from link deformation without relying on trunked models. Since the link deformation is measured at the base, we can name this feedback as "collocated" similarly to the nomenclature related to lumped models [55, 43]. In our case, the link deformation is indeed measured infinitely close to the motor shaft, exactly at the clamping point[1]. We acknowledge that the proposed passivity proof does not apply to the cases of non-collocated torque feedback i.e $\tau_m = -k_p EIw''(t, \varepsilon), \varepsilon > 0$ where the feedback torque is measured far from the clamping point.

We highlight that the theoretical finding of Theorem 1 agrees with existing passivity results on lumped models [54, 14]. These results often consider translational equivalent models [56]. In Appendix 2.7, we considered translational equivalent lumped models, and we derived the passivity conditions for collocated force feedback. These conditions are analytically derived for low-order models up to order 10. For all these models, it holds that collocated proportional force feedback is passive with $k_p > -1$. This is in line with Theorem 1. The analytical derivation of passivity conditions for higher-order models requires too long algebric computations and is not reported. To test higher-order cases, the next section considers a 50-order lumped model and passivity is tested numerically.

---

[1]According to [55, 43], when the feedback sensor is located on the same rigid body of the actuator we fall into the definition of "collocation"

System Parameters Range	
Proportional Gain	$k_p \in \left\{-1, -10^{-1}, -10^{-2}, 10^{-2}, 10^{-1}, 1, 10, 10^2, 10^3, 10^4, 10^5\right\}$
Motor Mass	$M_m \in [0.01, 0.1]\ kg$
Motor Friction	$d_m \in [0.01, 0.1, 1]\ \frac{N}{m^2}$
Motor Stiffness	$k_0 \in [100, 1000]\ \frac{N}{m}$
Link Block Mass	$m_i \in [0.1, 1, 10]\ kg$
Link Block Stiffness	$k_i \in [20, 40, 100]\ \frac{N}{m}$

Table 2.1: Considered parameters in passivity tests

2.4 Numerical Validation

As a first step to validate the theoretical finding expressed in Theorem 1, we derived a lumped 50-order translational equivalent model. We used the symbolic Python library Sympy [57] to compute the system impedance $I(s)$ at the environment port under the feedback action of a collocated proportional controller, as in Eq.(2.26). Details on the derivation and the implementation of such lumped model are reported in Appendix 2.8. In this section, we numerically evaluate the symbolic expression of such 50-order model, considering different link block mass and stiffness, which are reported in Table 2.1. For all the possible combinations of such values, we considered proportional controllers with $k_p \in \left\{-1, -10^{-1}, -10^{-2}, 10^{-2}, 10^{-1}, 1, 10, 10^2, 10^3, 10^4, 10^5\right\}$ and we tested the passivity of the transfer function $I(s)$ as defined in Appendix 2.8. To verify the passivity of the system, the phase of the impedance transfer function $I(s)$ in the Bode diagram was checked. The phase angle remains within the range of -90 to 90 degrees across the frequency spectrum for every proportional gain k_p with collocated feedback. This criterion confirms that the system does not generate energy. The result we found is that passivity is always verified, and this agrees with the statement of Theorem 1.

2.5 Conclusion

The main contribution of this chapter was to provide a solid theoretical motivation for the exploitation of link flexibilities in robot interaction control. In particular, while existing literature on interaction control passivity usually considers lumped models for the robotic system, here we account for the inherent continuum nature of robot links. Considering such a continuum link model, this work demonstrates that force control based on collocated link deformation feedback is always passive with $k_p > -1$. The theoretical result we found agrees with existing results on linear lumped models. As a future extension of this study, passivity could be studied by removing the small angle assumption for the joint variable θ, by including 3-dimensional external forces and by considering robots with multiple

degrees of freedom.

2.6   APPENDIX I

In this Section, the equations of motion of the system in Figure 2.1 are derived considering small link deformations $w(t, r)$ as in Section 2.2 but removing the small joint angle assumption. Let us define, in this case, the position vector $\boldsymbol{r}$ as

$$
\boldsymbol{r} = \begin{bmatrix} r \cos \theta(t) + w(t, r) \sin \theta(t) \\ r \sin \theta(t) - w(t, r) \cos \theta(t) \\ 0 \end{bmatrix} \tag{2.38}
$$

where r is the distance with respect to the center of rotation and the tip position vector $\boldsymbol{P}$ as

$$
\boldsymbol{P} = \begin{bmatrix} L \cos \theta(t) + w_E(t) \sin \theta(t) \\ L \sin \theta(t) - w_E(t) \cos \theta(t) \\ 0 \end{bmatrix} \tag{2.39}
$$

The total kinetic energy τ_{TOT} and the potential energy ν are given, as in the case of small joint angle, by

$$
\begin{aligned}
\tau_{\text{TOT}} &= \tau_{\text{motor}} + \tau_{\text{link}} + \tau_{\text{tip}} \\
\tau_{\text{motor}} &= \frac{1}{2} J_m \dot{\theta}^2(t) \\
\tau_{\text{link}} &= \frac{1}{2} \int_0^L \rho \dot{\boldsymbol{r}}^T \dot{\boldsymbol{r}} \, dr \\
\tau_{\text{tip}} &= \frac{1}{2} m \dot{\boldsymbol{P}}^T \dot{\boldsymbol{P}} \\
\nu &= \frac{1}{2} \int_0^L EI w''^2(t, r) \, dr
\end{aligned} \tag{2.40}
$$

where τ_{motor}, τ_{link} and τ_{tip} are the kinetic energies of the three components of the system: the motor, the link, and the mass m placed on the tip of the link on which the environmental force $\boldsymbol{F}_E$ acts. The symbols $(\cdot)$ and $(')$ represent the time and the space derivative, respectively. The equations of motion for the constrained system in Figure 2.1 are derived from the Lagrangian equation:

$$
\mathcal{L} = \tau_{\text{TOT}} - \nu
$$

$$
\mathcal{L} = \frac{1}{2} J_m \dot{\theta}^2 + \frac{1}{2} \int_0^L \rho \dot{\boldsymbol{r}}^T \dot{\boldsymbol{r}} \, dr + \frac{1}{2} m \dot{\boldsymbol{P}}^T \dot{\boldsymbol{P}} + \tag{2.41}
$$

$$
- \frac{1}{2} \int_0^L EI w''^2 \, dr
$$

where, differently from the case in Section 2.2,

$$
\dot{\boldsymbol{r}}^T \dot{\boldsymbol{r}} = r^2 \dot{\theta}^2 + \dot{w}^2 + w^2 \dot{\theta}^2 - 2r\dot{w}\dot{\theta} \tag{2.42}
$$

and

$$\dot{\boldsymbol{P}}^T \dot{\boldsymbol{P}} = L^2 \dot{\theta}^2 + \dot{w}_E^2 + w_E^2 \dot{\theta}^2 - 2L\dot{w}_E\dot{\theta}. \tag{2.43}$$

As in Section 2.2, the action functional $\mathcal{F}$ is defined as the time integral of the Lagrangian $\mathcal{L}$ on a specific trajectory. However, in the case of large joint angle assumption, the definitions of $\boldsymbol{r}$, $\boldsymbol{P}$ are different and will lead to a non-linear formulation of motion equations. In particular,

$$
\begin{aligned}
\mathcal{F} &= \int_{t_0}^{t_1} \int_0^L \mathcal{L}(r, \theta(t), w(t,r), \dot{\theta}(t), \dot{w}(t,r), w''(t,r))\, dr\, dt \\
&= \int_{t_0}^{t_1} \int_0^L \frac{J_m}{2L}\dot{\theta}^2 + \frac{\rho}{2}(r^2\dot{\theta}^2 + \dot{w}^2 + w^2\dot{\theta}^2 - 2r\dot{w}\dot{\theta}) + \\
&\quad + \frac{m}{2L}(L^2\dot{\theta}^2 + \dot{w}_E^2 + w_E^2\dot{\theta}^2 - 2L\dot{w}_E\dot{\theta}) - \frac{EI}{2}w''^2\, dr\, dt
\end{aligned}
\tag{2.44}
$$

According to Hamilton's principle, motion equations are obtained by introducing small perturbations on the states $\theta + \varepsilon v$ and $w + \varepsilon z$ for any $\varepsilon \in \mathbb{R}$, and these must be zero at the endpoints of the trajectory. The perturbations produce a variation $\delta\mathcal{F}$ of the action functional given by:

$$
\begin{aligned}
0 = \delta\mathcal{F} = \frac{d}{d\varepsilon}\bigg|_{\varepsilon=0} \int_{t_0}^{t_1} \int_0^L &\frac{J_m}{2L}(\dot{\theta} + \varepsilon\dot{v})^2 + \frac{\rho}{2}[r^2(\dot{\theta} + \varepsilon\dot{v})^2 + \\
(\dot{w} + \varepsilon\dot{z})^2 + (w + \varepsilon z)^2(\dot{\theta} + \varepsilon\dot{v})^2 &- 2r(\dot{w} + \varepsilon\dot{z})(\dot{\theta} + \varepsilon\dot{v})] + \\
+\frac{m}{2L}[L^2(\dot{\theta} + \varepsilon\dot{v})^2 + (\dot{w}_E + \varepsilon\dot{z})^2 &+ (w_E + \varepsilon z)^2(\dot{\theta} + \varepsilon\dot{v})^2 + \\
-2L(\dot{w}_E + \varepsilon\dot{z})(\dot{\theta} + \varepsilon\dot{v})] &- \frac{EI}{2}(w'' + \varepsilon z'')^2\, dr\, dt
\end{aligned}
\tag{2.45}
$$

$$
\begin{aligned}
0 = \delta\mathcal{F} = \int_{t_0}^{t_1} \int_0^L &\frac{J_m}{L}\dot{\theta}\dot{v} + \frac{\rho}{2}[2r^2\dot{\theta}\dot{v} + 2\dot{w}\dot{z} + 2w\dot{\theta}^2 z + \\
&+2w^2\dot{\theta}\dot{v} - 2r\dot{\theta}\dot{z} - 2r\dot{w}\dot{v}] + mL\dot{\theta}\dot{v} + \frac{m}{L}\dot{w}_E\dot{z}_E + \\
&-m\dot{w}_E\dot{v} - m\dot{\theta}\dot{z}_E + \frac{m}{L}\dot{\theta}^2 w_E z_E + \frac{m}{L}w_E^2\dot{\theta}\dot{v} + \\
&\hspace{5cm} -EIw''z''\, dr\, dt
\end{aligned}
\tag{2.46}
$$

Hamilton's principle requires that $\delta\mathcal{F}$ is zero for all possible perturbations ε. Thus, both perturbations must be set to 0 and integrals are applied to obtain the equations of motion. As a first step, considering $z = 0$ in Eq. (2.46), one can obtain

$$
\begin{aligned}
\int_{t_0}^{t_1} \int_0^L &\underbrace{\left(\frac{J_m}{L} + mL\right)\dot{\theta}\dot{v}}_{\delta\mathcal{F}_A} + \underbrace{\rho r^2\dot{\theta}\dot{v}}_{\delta\mathcal{F}_B} + \underbrace{\rho w^2\dot{\theta}\dot{v}}_{\delta\mathcal{F}_C} - \underbrace{\rho r\dot{w}\dot{v}}_{\delta\mathcal{F}_D} + \\
&-\underbrace{m\dot{w}_E\dot{v}}_{\delta\mathcal{F}_E} + \underbrace{\frac{m}{L}w_E^2\dot{\theta}\dot{v}}_{\delta\mathcal{F}_F}\, dr\, dt
\end{aligned}
\tag{2.47}
$$

Then, integrals from $\delta\mathcal{F}_A$ to $\delta\mathcal{F}_F$ are computed by parts

$$
\delta\mathcal{F}_A = \int_{t_0}^{t_1} (\frac{J_m}{L} + mL)\dot{\theta}\dot{v}\, dt \quad \overset{\text{P.I}}{=} \quad \int_{t_0}^{t_1} -(\frac{J_m}{L} + mL)\ddot{\theta}v\, dt
$$

$$
\delta\mathcal{F}_B = \int_{t_0}^{t_1} \rho r^2 \dot{\theta}\dot{v}\, dt \quad \overset{\text{P.I}}{=} \quad \int_{t_0}^{t_1} -\rho r^2 \ddot{\theta}v\, dt
$$

$$
\delta\mathcal{F}_C = \int_{t_0}^{t_1} \rho w^2 \dot{\theta}\dot{v}\, dt \quad \overset{\text{P.I}}{=} \quad \int_{t_0}^{t_1} -\rho v(w^2\ddot{\theta} + 2w\dot{w}\dot{\theta})\, dt
$$

$$
\delta\mathcal{F}_D = \int_{t_0}^{t_1} -\rho r\dot{w}\dot{v}\, dt \quad \overset{\text{P.I}}{=} \quad \int_{t_0}^{t_1} \rho r\ddot{w}v\, dt
$$

$$
\delta\mathcal{F}_E = \int_{t_0}^{t_1} -m\dot{w}_E\dot{v}\, dt \quad \overset{\text{P.I}}{=} \quad \int_{t_0}^{t_1} m\ddot{w}_E v\, dt
$$

$$
\delta\mathcal{F}_F = \int_{t_0}^{t_1} \frac{m}{L}w_E^2\dot{\theta}\dot{v}\, dt \quad \overset{\text{P.I}}{=} \quad \int_{t_0}^{t_1} -\frac{m}{L}v(w_E^2\ddot{\theta} + 2w_E\dot{w}_E\dot{\theta})\, dt
$$

(2.48)

$$
\int_{t_0}^{t_1} \int_0^L \left[-\left(\frac{J_m}{L} + mL\right)\ddot{\theta} - \rho r^2\ddot{\theta} - \rho(w^2\ddot{\theta} + 2w\dot{w}\dot{\theta}) + \right.
$$
$$
\left. + \rho r\ddot{w} + m\ddot{w}_E - \frac{m}{L}(w_E^2\ddot{\theta} + 2w_E\dot{w}_E\dot{\theta}) \right]v\, dr\, dt
$$

(2.49)

to get the following equation

$$
(\frac{J_m}{L} + \rho w^2 + \frac{m}{L}w_E^2)\ddot{\theta} + \rho r(r\ddot{\theta} - \ddot{w}) + (2\rho w\dot{w} +
$$
$$
+ 2\frac{m}{L}w_E\dot{w}_E)\dot{\theta} + m(L\ddot{\theta} - \ddot{w}_E) = 0
$$

(2.50)

As a second step, considering $v = 0$ in Eq. (2.46), the following expression is obtained

$$
\int_{t_0}^{t_1} \int_0^L \underbrace{-\rho(r\dot{\theta} - \dot{w})\dot{z}}_{\delta\mathcal{F}_G} - \underbrace{\frac{m}{L}(L\dot{\theta} - \dot{w}_E)\dot{z}_E}_{\delta\mathcal{F}_H} - \underbrace{EIw''z''}_{\delta\mathcal{F}_I} +
$$
$$
+ \rho w\dot{\theta}^2 z + \frac{m}{L}\dot{\theta}^2 w_E z_E\, dr\, dt
$$

(2.51)

Then, integrals $\delta\mathcal{F}_G$, $\delta\mathcal{F}_H$ and $\delta\mathcal{F}_I$ are computed by parts

$$\delta\mathcal{F}_G = \int_{t_0}^{t_1} -\rho(r\dot\theta - \dot w)\dot z\, dt$$

$$\overset{\text{P.I}}{=} \int_{t_0}^{t_1} \rho(r\ddot\theta - \ddot w)z\, dt$$

$$\delta\mathcal{F}_H = \int_{t_0}^{t_1} -\frac{m}{L}(L\dot\theta - \dot w_E)\dot z_E\, dt$$

$$\overset{\text{P.I}}{=} \int_{t_0}^{t_1} \frac{m}{L}(L\ddot\theta - \ddot w_E)z_E\, dt \tag{2.52}$$

$$\delta\mathcal{F}_I = -\int_0^L EIw''z''\, dr$$

$$\overset{\text{P.I}}{=} \int_0^L \frac{F_{E_\perp}}{L}z_E - EIw''''z\, dr$$

$$\int_{t_0}^{t_1}\int_0^L \underbrace{\left[\rho(r\ddot\theta - \ddot w) - EIw'''' + \rho w\dot\theta^2)\right]}_{=0} z +$$

$$\underbrace{\left[\frac{F_{E_\perp}}{L} + \frac{m}{L}(L\ddot\theta - \ddot w_E) + \frac{m}{L}\dot\theta^2 w_E\right]}_{=0} z_E\, dr\, dt \tag{2.53}$$

and the following equations of motion are obtained

$$\rho(r\ddot\theta - \ddot w) = EIw'''' - \rho w\dot\theta^2 \tag{2.54}$$

$$\frac{F_{E_\perp}}{L} + \frac{m}{L}(L\ddot\theta - \ddot w_E) + \frac{m}{L}\dot\theta^2 w_E = 0$$
$$m(L\ddot\theta - \ddot w_E) = -F_{E_\perp} - m\dot\theta^2 w_E \tag{2.55}$$

Substituting the equation of motion for the link (2.54) and the boundary condition of the tip mass (2.55) in the equation of motion for the motor (2.50), one can obtain

$$(\frac{J_m}{L} + \rho w^2 + \frac{m}{L}w_E^2)\ddot\theta + r(EIw'''' - \rho w\dot\theta^2) + (2\rho w\dot w +$$
$$+2\frac{m}{L}w_E\dot w_E)\dot\theta - F_{E_\perp} - m\dot\theta^2 w_E = \frac{\tau_m}{L} \tag{2.56}$$

2.7   APPENDIX II

According to Hogan and Colgate [54], a linear, time-invariant 1-port is passive if and only if:

1. $I(s)$ has no poles in the right half-plane

2. $I(s)$ has a Nyquist plot which lies wholly within the closed left half-plane

This section investigates the passivity conditions of two lumped models that are an equivalent linear representation of the system in Figure 2.1 where angular quantities are translated into linear quantities. The considered system is discretized in a number of blocks from 2 to 5 characterised by lumped mass, and stiffness, under the action of a proportional force controller feeding back a collocated signal.

2.7.1   System discretized into 2 blocks
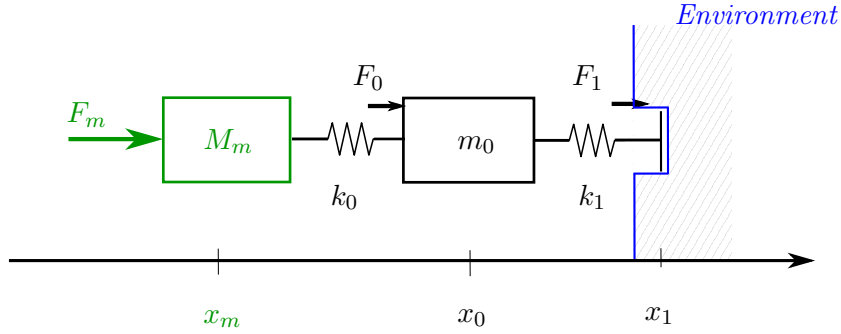
Figure 2.2: Linear representation of a two-blocks model of flexible link

The system is modelled as two rigid blocks, representing the motor and the link, respectively, connected by linear springs. The link has the whole mass lumped on its centre. In this case, the link is represented by the second block, so its mass is m_0. Let us call x_m and M_m the motor linear equivalent position and mass, x_0 the linear position of the center of mass of the link and x_1 the linear position of the environment. F_m denotes the motor input force, F_0 and F_1 the linear springs force, where F_1 measures the interaction force with the environment. k_0 describes the motor gearbox stiffness while k_1 the link bending stiffness. Therefore, the dynamics of the system in Figure 2.2 can be expressed as

$$
\begin{aligned}
M_m \ddot{x}_m + d_m \dot{x}_m &= F_m - F_0 \\
F_0 &= k_0(x_m - x_0) \\
m_0 \ddot{x}_0 &= F_0 - F_1 \\
F_1 &= k_1(x_0 - x_1)
\end{aligned}
\tag{2.57}
$$

with d_m the motor damping.

2.7.1.a   Passivity conditions

Considering the system represented in Fig. 2.2, subject to a collocated proportional force controller in the form $F_m = -k_p F_0$, the transfer function $I_2(s) = -\frac{F_1}{\dot{x}_1}$

represents the system impedance seen at the environment port $(F_1, \dot{x}_1)$. It can be computed as

$$I_2(s) = \frac{N(s)}{D(s)} \tag{2.58}$$

where

$$\mathrm{N(s)} = (M_m s^3 m_0 + d_m s^2 m_0 + d_m k_0 + s(M_m k_0 + k_p k_0 m_0 + k_0 m_0))k_1 \tag{2.59}$$

$$\begin{aligned}\mathrm{D(s)} = (M_m s^4 m_0 + d_m s^3 m_0 + k_p k_0 k_1 + s^2(M_m k_0 + M_m k_1 + k_p k_0 m_0 + \\ + k_0 m_0) + s(d_m k_0 + d_m k_1) + k_0 k_1)\end{aligned} \tag{2.60}$$

To satisfy the stability condition (1), $I_2(s)$ must have no poles in the right half-plane. For this reason, the Hurwitz criterion was applied. Considering the characteristic polynomial $P(s)$ of $I_2(s)$

$$P(s) = a_0 s^4 + a_1 s^3 + a_2 s^2 + a_3 s + a_4 \tag{2.61}$$

with

$$a_0 = M_m m_0 \tag{2.62a}$$

$$a_1 = d_m m_0 \tag{2.62b}$$

$$a_2 = M_m k_0 + M_m k_1 + k_p k_0 m_0 + k_0 m_0 \tag{2.62c}$$

$$a_3 = d_m k_0 + d_m k_1 \tag{2.62d}$$

$$a_4 = k_p k_0 k_1 + k_0 k_1 \tag{2.62e}$$

The Hurwitz matrix is constructed as

$$H = \begin{bmatrix} a1 & a3 & 0 & 0 \\ a0 & a2 & a4 & 0 \\ 0 & a1 & a3 & 0 \\ 0 & a0 & a2 & a4 \end{bmatrix} \tag{2.63}$$

Considering $P(s)$, the four principal minors of the Hurwitz matrix are analysed

$$Min_1 = a1 \tag{2.64a}$$

$$Min_2 = \begin{bmatrix} a1 & a3 \\ a0 & a2 \end{bmatrix} \tag{2.64b}$$

$$Min_3 = \begin{bmatrix} a1 & a3 & 0 \\ a0 & a2 & a4 \\ 0 & a1 & a3 \end{bmatrix} \tag{2.64c}$$

$$Min_4 = H \tag{2.64d}$$

$$H_1 : \det(Min_1) > 0 \Rightarrow d_m m_0 > 0 \Rightarrow d_m > 0,\ m_0 > 0 \tag{2.65a}$$

$$H_2 : \det(Min_2) > 0 \Rightarrow d_m k_0 m_0^2(k_p + 1) > 0 \Rightarrow d_m > 0,\ k_0 > 0,\ k_p > -1 \tag{2.65b}$$

$$H_3 : \det(Min_3) > 0 \Rightarrow d_m^2 k_0^2 m_0^2(k_p + 1) > 0 \Rightarrow k_p > -1 \tag{2.65c}$$

$$H_4 : \det(Min_4) > 0 \Rightarrow d_m^2 k_0^3 k_1 m_0^2(k_p + 1)^2 > 0 \Rightarrow k_0 > 0,\ k_1 > 0,\ k_p > -1 \tag{2.65d}$$

Considering M_m and m_0 the motor mass and the link mass, motor damping d_m, linear stiffnesses k_0 and k_1, positive terms the system is stable for $k_p > -1$.

To find the passivity condition (2), $I_2(s)$ must have a Nyquist plot that lies wholly within the closed left half-plane. Considering the $I_2(s)$ transfer function, s must be replaced with $i\omega$. This represents the Laplace transform of the system frequency response.

$$N(i\omega) = k_1(i\omega(M_m k_0 + k_0 m_0 + k_0 k_p m_0) + d_m k_0 - d_m m_0 \omega^2 - M_m m_0 i\omega^3) \tag{2.66}$$

$$D(i\omega) = k_0 k_1 - \omega^2(M_m k_0 + M_m k_1 + k_0 m_0 + k_0 k_p m_0) + k_0 k_1 k_p + M_m m_0 \omega^4 +$$
$$+ i\omega(d_m k_0 + d_m k_1) - d_m m_0 i\omega^3$$
$$D(i\omega) = a - ib$$
$$\text{with a} = M_m m_0 \omega^4 + (-M_m k_0 - M_m k_1 - k_0 m_0 - k_0 k_p m_0)\omega^2 + k_0 k_1 + k_p k_0 k_1$$
$$\text{and b} = -d_m m_0 \omega^3 + (d_m k_0 + d_m k_1)\omega \tag{2.67}$$

To simplify the transfer function $I_2(i\omega)$, it must be rationalised by multiplying the numerator and the denominator by the conjugate of the denominator $(a - ib)$. Then, we looked for the condition for $Re(I_2(i\omega))$ strictly positive. Both the real part of the numerator and denominator must be strictly positive: $Re(N(i\omega)) > 0$ and $Re(D(i\omega)) > 0$. We found only the condition on the numerator because the real part of the denominator equals $a^2 + b^2$, so it is always strictly positive.

$$N(i\omega) = (k_1(i\omega(M_m k_0 + k_0 m_0 + k_0 k_p m_0) + d_m k_0 - d_m m_0 \omega^2 + M_m m_0 i\omega^3))$$
$$(a + bi) \tag{2.68}$$

$$Re(N(i\omega)) = a d_m k_0 k_1 + b\omega M_m k_0 k_1 + b\omega k_0 k_1 m_0 - b M_m k_1 m_0 \omega^3 - a d_m k_1 m_0 \omega^2 +$$
$$b k_0 k_1 k_p m_0 \omega \tag{2.69}$$

Substituting the definitions of a and b (2.67), the passivity condition on $Re(N(i\omega)) > 0$ is calculated

$$Re(N(i\omega)) > 0 \Rightarrow d_m k_0^2 k_1^2(k_p + 1) > 0 \Rightarrow d_m > 0,\ k_p > -1 \tag{2.70}$$

Considering M_m, m_0 the motor mass and the link mass, motor damping d_m, linear stiffnesses k_0 and k_1 positive terms the system is passive for $k_p > -1$.

2.7.2   System discretized into 3 blocks

The system is modelled as three rigid blocks connected by linear springs. The link is split into the second and third blocks of masses m_i. Each block has the mass lumped at its centre.
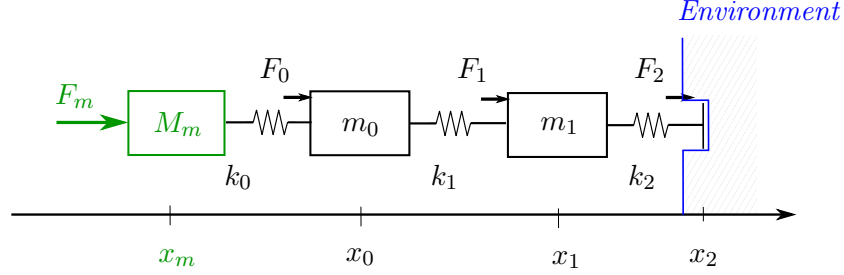
Figure 2.3: Linear representation of a three-blocks model of flexible link

We define x_m and M_m as the motor position and mass, x_0 and x_1 as the positions of the center of mass of the link blocks, x_2 as the position of the environment and m_0 and m_1 represent the mass discretization of the link. The input force of the motor is indicated by F_m while F_0, F_1 and F_2 are the linear springs force and F_2 measures also the interaction force with the environment. k_0 represents the motor gearbox stiffness while k_1 and k_2 are the linear stiffness of the link. Therefore, the dynamics of the system in Figure 2.3 can be expressed as

$$
\begin{aligned}
M_m\ddot{x}_m + d_m\dot{x}_m &= F_m - F_0 \\
F_0 &= k_0(x_m - x_0) \\
m_0\ddot{x}_0 &= F_0 - F_1 \\
F_1 &= k_1(x_0 - x_1) \\
m_1\ddot{x}_1 &= F_1 - F_2 \\
F_2 &= k_2(x_1 - x_2)
\end{aligned}
\tag{2.71}
$$

with d_m the motor damping.

2.7.2.a   Passivity Conditions

Considering the system represented in Fig. 2.3, subject to a collocated proportional force controller in the form $F_m = -k_p F_0$, the transfer function $I_3(s) = -\frac{F_2}{\dot{x}_2}$ represents the system impedance seen at the environment port $(F_2, \dot{x}_2)$. It can be computed as

$$
I_3(s) = \frac{N(s)}{D(s)}
\tag{2.72}
$$

where

$$\begin{aligned}
\text{N(s)} = (&M_m s^5 m_0 m_1 + d_m s^4 m_0 m_1 + d_m k_0 k_1 + s^3 (M_m k_0 m_1 + M_m k_1 m_0 + \\
&+ M_m k_1 m_1 + k_p k_0 m_0 m_1 + k_0 m_0 m_1) + s^2 (d_m k_0 m_1 + d_m k_1 m_0 + \\
&+ d_m k_1 m_1) + s(M_m k_0 k_1 + k_p k_0 k_1 m_0 + k_p k_0 k_1 m_1 + k_0 k_1 m_0 + \\
&+ k_0 k_1 m_1)) k_2
\end{aligned}$$
(2.73)

$$\begin{aligned}
\text{D(s)}(&M_m s^6 m_0 m_1 + d_m s^5 m_0 m_1 + k_p k_0 k_1 k_2 + s^4 (M_m k_0 m_1 + M_m k_1 m_0 + M_m k_1 m_1 + \\
&+ M_m k_2 m_0 + k_p k_0 m_0 m_1 + k_0 m_0 m_1) + s^3 (d_m k_0 m_1 + d_m k_1 m_0 + d_m k_1 m_1 + \\
&+ d_m k_2 m_0) + s^2 (M_m k_0 k_1 + M_m k_0 k_2 + M_m k_1 k_2 + k_p k_0 k_1 m_0 + k_p k_0 k_1 m_1 + \\
&+ k_p k_0 k_2 m_0 + k_0 k_1 m_0 + k_0 k_1 m_1 + k_0 k_2 m_0) + s(d_m k_0 k_1 + d_m k_0 k_2 + \\
&+ d_m k_1 k_2) + k_0 k_1 k_2)
\end{aligned}$$
(2.74)

As in the previous case, to find the stability conditions, $I_3(s)$ must have no poles in the right half-plane. This condition is verified using the Hurwitz criterion. Considering the characteristic polynomial $P(s)$ of $I_3(s)$

$$P(s) = a_0 s^6 + a_1 s^5 + a_2 s^4 + a_3 s^3 + a_4 s^2 + a_5 s + a_6 \tag{2.75}$$

with

$$a_0 = M_m m_0 m_1 \tag{2.76a}$$
$$a_1 = d_m m_0 m_1 \tag{2.76b}$$
$$a_2 = M_m k_0 m_1 + M_m k_1 m_0 + M_m k_1 m_1 + M_m k_2 m_0 + k_0 m_0 m_1 + k_p k_0 m_0 m_1 \tag{2.76c}$$
$$a_3 = d_m k_0 m_1 + d_m k_1 m_0 + d_m k_1 m_1 + d_m k_2 m_0 \tag{2.76d}$$
$$\begin{aligned}a_4 = &M_m k_0 k_1 + M_m k_0 k_2 + M_m k_1 k_2 + k_0 k_1 m_0 + k_0 k_1 m_1 + k_0 k_2 m_0 + \\ &k_p k_0 k_1 m_0 + k_p k_0 k_1 m_1 + k_p k_0 k_2 m_0\end{aligned} \tag{2.76e}$$
$$a_5 = d_m k_0 k_1 + d_m k_0 k_2 + d_m k_1 k_2 \tag{2.76f}$$
$$a_6 = k_0 k_1 k_2 + k_p k_0 k_1 k_2 \tag{2.76g}$$

The Hurwitz matrix is constructed as

$$H = \begin{bmatrix} a1 & a3 & a5 & 0 & 0 & 0 \\ a0 & a2 & a4 & a6 & 0 & 0 \\ 0 & a1 & a3 & a5 & 0 & 0 \\ 0 & a0 & a2 & a4 & a6 & 0 \\ 0 & 0 & a1 & a3 & a5 & 0 \\ 0 & 0 & a0 & a2 & a4 & a6 \end{bmatrix} \tag{2.77}$$

Considering $P(s)$, the six principal minors of the Hurwitz matrix are analysed

$$Min_1 = a1 \tag{2.78a}$$

$$Min_2 = \begin{bmatrix} a1 & a3 \\ a0 & a2 \end{bmatrix} \tag{2.78b}$$

$$Min_3 = \begin{bmatrix} a1 & a3 & a5 \\ a0 & a2 & a4 \\ 0 & a1 & a3 \end{bmatrix} \tag{2.78c}$$

$$Min_4 = \begin{bmatrix} a1 & a3 & a5 & 0 \\ a0 & a2 & a4 & a6 \\ 0 & a1 & a3 & a5 \\ 0 & a0 & a2 & a4 \end{bmatrix} \tag{2.78d}$$

$$Min_5 = \begin{bmatrix} a1 & a3 & a5 & 0 & 0 \\ a0 & a2 & a4 & a6 & 0 \\ 0 & a1 & a3 & a5 & 0 \\ 0 & a0 & a2 & a4 & a6 \\ 0 & 0 & a1 & a3 & a5 \end{bmatrix} \tag{2.78e}$$

$$Min_6 = H \tag{2.78f}$$

$$H_1 = det(Min_1) > 0 \Rightarrow d_m m_0 m_1 > 0 \Rightarrow d_m > 0, \; m_0 > 0, \; m_1 > 0 \tag{2.79a}$$

$$H_2 = det(Min_2) > 0 \Rightarrow d_m k_0 m_0^2 m_1^2 (k_p + 1) > 0 \Rightarrow d_m > 0, \; k_0 > 0, \tag{2.79b}$$

$$k_p > -1 \tag{2.79c}$$

$$H_3 = det(Min_3) > 0 \Rightarrow d_m^2 k_0^2 m_0^2 m_1^3 (k_p + 1) > 0 \Rightarrow m_1 > 0, \; k_p > -1 \tag{2.79d}$$

$$H_4 = det(Min_4) > 0 \Rightarrow d_m^2 k_0^3 k_1 m_0^2 m_1^4 (k_p + 1)^2 > 0 \Rightarrow k_0 > 0, \; k_1 > 0, \; k_p > -1 \tag{2.79e}$$

$$H_5 = det(Min_5) > 0 \Rightarrow d_m^3 k_0^4 k_1^2 m_0^2 m_1^4 (k_p + 1)^2 > 0 \Rightarrow d_m > 0, \; k_p > -1 \tag{2.79f}$$

$$H_6 = det(Min_6) > 0 \Rightarrow d_m^3 k_0^5 k_1^3 k_2 m_0^2 m_1^4 (k_p + 1)^3 > 0 \Rightarrow d_m > 0, \; k_0 > 0, \tag{2.79g}$$

$$\tag{2.79h}$$

$$k_1 > 0, \; k_2 > 0, \; k_p > -1 \tag{2.79i}$$

Considering the motor mass M_m, link mass m_0 and m_1, motor damping d_m and linear stiffnesses k_0, k_1, k_2 positive terms, the system is stable, as in the case (2.7.1.a), for every $k_p > -1$.

To find the passivity conditions, $I_3(s)$ must have a Nyquist plot that lies wholly within the closed left half-plane. Considering the $I_3(s)$ transfer function,

s must be replaced with $i\omega$.

$$N(i\omega) = k_2(d_m k_0 k_1 - \omega^2(d_m k_0 m_1 + d_m k_1 m_0 + d_m k_1 m_1) + d_m m_0 m_1 \omega^4 +$$
$$+ i\omega(M_m k_0 k_1 + k_0 k_1 m_0 + k_0 k_1 m_1 + k_0 k_1 k_p m_0 + k_0 k_1 k_p m_1) +$$
$$- i\omega^3(M_m k_0 m_1 + M_m k_1 m_0 + M_m k_1 m_1 + k_0 m_0 m_1 + k_0 k_p m_0 m_1) +$$
$$+ M_m m_0 m_1 i\omega^5)$$

$$(2.80)$$

$$D(i\omega) = i\omega(d_m k_0 k_1 + d_m k_0 k_2 + d_m k_1 k_2) - i\omega^3(d_m k_0 m_1 + d_m k_1 m_0 + d_m k_1 m_1 +$$
$$+ d_m k_2 m_0) - \omega^2(M_m k_0 k_1 + M_m k_0 k_2 + M_m k_1 k_2 + k_0 k_1 m_0 + k_0 k_1 m_1 +$$
$$+ k_0 k_2 m_0 + k_0 k_1 k_p m_0 + k_0 k_1 k_p m_1 + k_0 k_2 k_p m_0) + \omega^4(M_m k_0 m_1 +$$
$$+ M_m k_1 m_0 + M_m k_1 m_1 + M_m k_2 m_0 + k_0 m_0 m_1 + k_0 k_p m_0 m_1) + k_0 k_1 k_2 +$$
$$+ k_0 k_1 k_2 k_p - M_m m_0 m_1 \omega^6 + d_m m_0 m_1 i\omega^5$$

$$(2.81)$$

$$D(i\omega) = a + ib \qquad (2.82)$$
$$\text{with } a = -M_m m_0 m_1 \omega^6 + (M_m k_0 m_1 + M_m k_1 m_0 + M_m k_1 m_1 + M_m k_2 m_0 +$$
$$+ k_0 m_0 m_1 + k_0 k_p m_0 m_1)\omega^4 + (-M_m k_0 k_1 - M_m k_0 k_2 - M_m k_1 k_2 +$$
$$- k_0 k_1 m_0 - k_0 k_1 m_1 - k_0 k_2 m_0 - k_0 k_1 k_p m_0 - k_0 k_1 k_p m_1 +$$
$$- k_0 k_2 k_p m_0)\omega^2 + k_0 k_1 k_2 + k_0 k_1 k_2 k_p$$

$$(2.83)$$
$$\text{and } b = d_m m_0 m_1 \omega^5 + (-d_m k_0 m_1 - d_m k_1 m_0 - d_m k_1 m_1 - d_m k_2 m_0)\omega^3 +$$
$$+ (d_m k_0 k_1 + d_m k_0 k_2 + d_m k_1 k_2)\omega$$
$$(2.84)$$

To simplify the transfer function $I_3(i\omega)$, it must be rationalised by multiplying the numerator and the denominator by the conjugate of the denominator $(a - ib)$. Then, we looked for the condition for $Re(I_3(i\omega))$ strictly positive. Both the real part of the numerator and denominator must be strictly positive: $Re(N(i\omega)) > 0$ and $Re(D(i\omega)) > 0$. We found only the condition on the numerator because the

real part of the denominator equals $a^2 + b^2$, so it is always strictly positive.

$$
\begin{aligned}
\text{N}(i\omega) = &(k_2(d_m k_0 k_1 - \omega^2(d_m k_0 m_1 + d_m k_1 m_0 + d_m k_1 m_1) + d_m m_0 m_1 \omega^4 + \\
&+ i\omega(M_m k_0 k_1 + k_0 k_1 m_0 + k_0 k_1 m_1 + k_0 k_1 k_p m_0 + k_0 k_1 k_p m_1) + \\
&- i\omega^3(M_m k_0 m_1 + M_m k_1 m_0 + M_m k_1 m_1 + k_0 m_0 m_1 + k_0 k_p m_0 m_1) + \\
&+ M_m m_0 m_1 i\omega^5))(a + bi)
\end{aligned}
$$
$$(2.85)$$

$$
\begin{aligned}
\text{Re}(\text{N}(i\omega)) = &a d_m k_0 k_1 k_2 - M_m b k_0 k_2 m_1 \omega^3 - M_m b k_1 k_2 m_0 \omega^3 - M_m b k_1 k_2 m_1 \omega^3 + \\
&+ M_m b k_2 m_0 m_1 \omega^5 - a d_m k_0 k_2 m_1 \omega^2 - a d_m k_1 k_2 m_0 \omega^2 + \\
&- a d_m k_1 k_2 m_1 \omega^2 + a d_m k_2 m_0 m_1 \omega^4 - b k_0 k_2 m_0 m_1 \omega^3 + \\
&+ M_m b k_0 k_1 k_2 \omega + b k_0 k_1 k_2 m_0 \omega + b k_0 k_1 k_2 m_1 \omega + b k_0 k_1 k_2 k_p m_0 \omega + \\
&+ b k_0 k_1 k_2 k_p m_1 \omega - b k_0 k_2 k_p m_0 m_1 \omega^3
\end{aligned}
$$
$$(2.86)$$

Substituting the definitions of a and b (2.82), the passivity condition on $Re(N(i\omega)) > 0$ is calculated

$$
\text{Re}(\text{N}(i\omega)) > 0 \Rightarrow d_m k_0^2 k_1^2 k_2^2 (k_p + 1) > 0 \Rightarrow d_m > 0,\ k_p > -1 \qquad (2.87)
$$

so the passivity condition is again for $k_p > -1$.

2.7.3   Lumped models with 3 and 4 segments

The cases of lumped models with 3 and 4 segments are similar to the previous ones. Since mathematical expressions are too long, we just report the passivity condition which is again $k_p > -1$ for both models.

2.8   APPENDIX III

This section shows the derivation of a high-order lumped model and the computation of the system impedance $I(s)$ to the environment port $(F_{n-1}, \dot{x}_{n-1})$.

The dynamics of the system can be modelled as a series of rigid blocks connected by linear springs as shown in Figure 2.4.
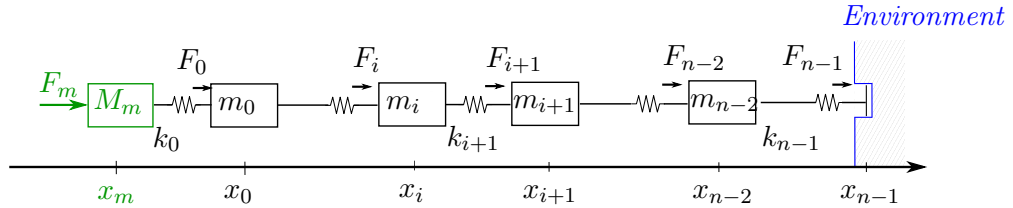

Figure 2.4: Linear representation of a n-blocks model of flexible link

The system is modelled as n rigid blocks connected by linear springs. The flexible link is split into $n - 1$ segments. Each link block has the mass m_i lumped at its centre. We define x_m and M_m as the motor position and mass, x_i as the position of the center of mass of the i-th block and x_{n-1} as the position of the environment. The input force of the motor is indicated by F_m while F_i is the linear spring force of the i-th block and F_{n-1} measures the interaction force with the environment. The linear springs have stiffness k_i while k_0 is the motor gearbox stiffness. The dynamics of the system in Figure 2.4 can finally be expressed in iterative form as

$$
\begin{aligned}
M_m \ddot{x}_m + d_m \dot{x}_m &= F_m - F_0 \\
F_0 &= k_0(x_m - x_0) \\
m_i \ddot{x}_i &= F_i - F_{i+1} \\
F_{i+1} &= k_{i+1}(x_i - x_{i+1}) \\
m_{n-2} \ddot{x}_{n-2} &= F_{n-2} - F_{n-1} \\
F_{n-1} &= k_{n-1}(x_{n-2} - x_{n-1})
\end{aligned}
\tag{2.88}
$$

Using the Laplace transform, the system dynamics can be expressed as

$$
\begin{aligned}
F_0 &= F_m - s x_m (M_m s + d_m) \\
s x_m &= \frac{s F_0}{k_0} + s x_0 \\
F_{i+1} &= F_i - m_i s^2 x_i \\
s x_i &= \frac{s F_{i+1}}{k_{i+1}} + s x_{i+1} \\
F_{n-1} &= F_{n-2} - m_{n-2} s^2 x_{n-2} \\
s x_{n-2} &= \frac{s F_{n-1}}{k_{n-1}} + s x_{n-1}
\end{aligned}
\tag{2.89}
$$

Then, a collocated proportional force controller in the form $F_m = -k_p F_0$ is applied and the impedance $I(s) = \frac{F_{n-1}}{\dot{x}_{n-1}}$ at the environment port $(F_{n-1}, \dot{x}_{n-1})$ is computed following the steps reported in Table 2.2. This procedure has been implemented using the Python Simbolic library [57] in order to obtain the impedance of a generic flexible link split into $n - 1$ segments.

Algebric steps to compute $I(s)$	
Substitution	**Leads to**
$sx_m(F_0, sx_0)$ in F_0	$F_0(sx_0, F_m)$
$F_0(sx_0, F_m)$ in F_{i+1}	$F_{i+1}(sx_i, F_m)$
$sx_i(F_{i+1}, sx_{i+1})$ in F_{i+1}	$F_{i+1}(sx_{i+1}, F_m)$
$F_{i+1}(sx_{i+1}, F_m)$ in F_{n-1}	$F_{n-1}(sx_{n-2}, F_m)$
$sx_{n-2}(F_{n-1, sx_{n-1}})$ in F_{n-1}	$F_{n-1}(sx_{n-1}, F_m)$

Table 2.2: steps to find impedance I(s)

Chapter 3

Force control exploiting
non-collocated feedback

3.1 Introduction

The previous chapter derived a general result about force control passivity: proportional collocated force control of a continuum flexible link is passive at the environment port. However, we derive passivity conditions only in the case of collocated feedback. On one side, existing results on lumped models state that non-collocated feedback can lead to inferior stability properties [55]; on the other side, non-collocated feedback can lead to important application-specific advantages. As an example, in robotic surgery, the force measured at the laparoscopic tool base (collocated) is subject to noise due to friction effects when sliding into trocars, which may significantly hinder the accurate measurement of tissue interaction forces [23]. Such noise can easily be avoided by placing a force sensor after the trocar, e.g., close to the tip of the surgical tool. This arrangement could provide an extremely accurate estimation of tissue interaction forces. Since we were not able to derive passivity conditions for non-collocated sensor arrangement on continuum links, this chapter presents some passivity and stability results using accurate high-order lumped approximants of the continuum mechanics model in Fig. 2.1. First, Section 3.2 presents a symbolic software library able to model a generic flexible link clamped to a revolute robotic joint. The software library can generate n^{th}-order lumped models to accurately approximate the dynamics of flexible links characterized by certain inertia, stiffness, and damping parameters under the action of non-collocated feedback. Stability and passivity of these models are then analysed in Section 3.3, considering robotic surgery as a reference application. A high-order lumped model of a commonly used laparoscopic tool is used to analyse the stability margins of proportional control using non-collocated feedback. Different kinds of non-collocation are compared, coming from deformation measures at different tool locations (e.g. base, middle points and tip). Finally, an experimental validation of theoretical findings is reported in Section 3.5 and the conclusion are drawn in Section 3.6.

The results of this chapter are reported in "Force control of a flexible link exploiting non-collocated feedback" submitted to "IEEE Transactions on Mechatronics".

3.2 Modelling flexible links using high-order lumped models

This section describes a symbolic software library implemented using the Python Simbolic library [57] able to derive a high-order lumped approximation of the continuum mechanics model in Fig. 2.1.

The system is modelled as n rigid blocks connected by rotational springs and dampings, as shown in Figure 3.1. The link of length L and mass M is split into $n-1$ segments. Each link block has a mass $m_i = \frac{M}{n-1}$ and a rotational moment of inertia j_i.
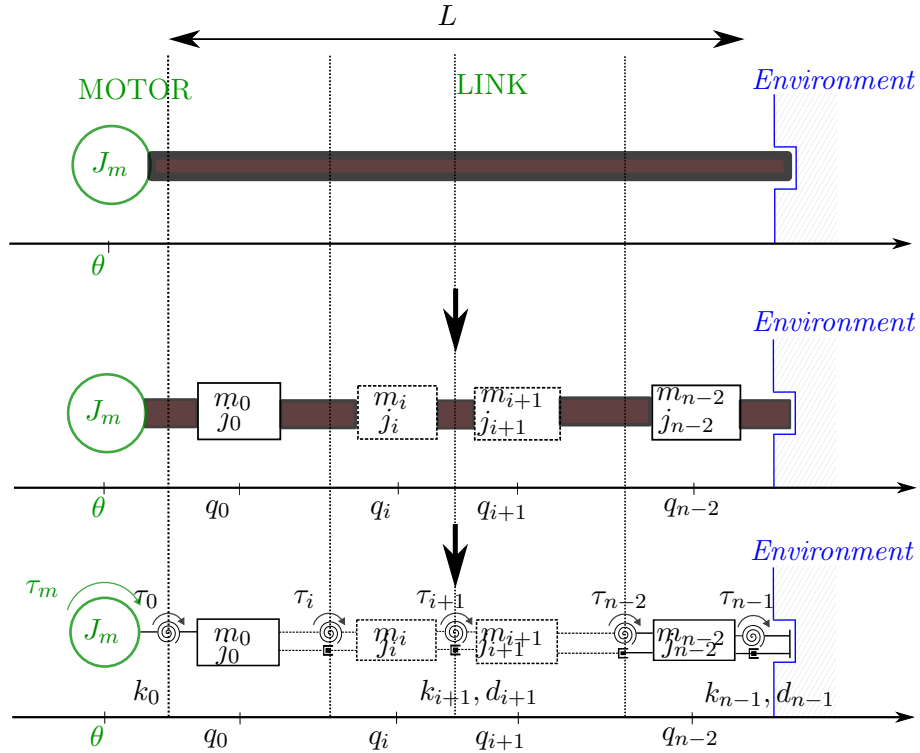
Figure 3.1: Modelling of a flexible link driven by a motor into discrete blocks

Let us call θ and J_m the motor position and inertia, and q_i the positions of the center of mass and inertia of the motor and the i-th block. The motor input torque is denoted τ_m while τ_i is the torsional spring torque related to the i-th block, and τ_{n-1} is the interaction torque with the environment. k_0 represents the motor gearbox stiffness, while k_i and d_i represent the torsional stiffness and damping of the i-th block. Given the bending stiffness of the link K and the link

damping D, the stiffness of the rotational springs and damping of the i-th block is calculated respectively as $k_i = (n-1)K$ and $d_i = (n-1)D$. $l = \frac{L}{n-1}$ is the distance between one block and another. The dynamics of the system in Figure 3.1 interacting with a stiff environment can be expressed in iterative form as

$$J_m\ddot{\theta} + d_m\dot{\theta} + \sum_{h=0}^{n-2}(m_h((h+1)l)^2 + j_h)\ddot{q}_h = \tau_m$$

$$\tau_0 = k_0(\theta - q_0)$$

$$j_i\ddot{q}_i + \sum_{h=i+1}^{n-2}(m_h((h-i)l)^2 + j_h)\ddot{q}_h = \tau_i \qquad (3.1)$$

$$\tau_{i+1} = k_{i+1}(q_i - q_{i+1}) + d_{i+1}(\dot{q}_i - \dot{q}_{i+1})$$

$$j_{n-2}\ddot{q}_{n-2} = \tau_{n-2}$$

$$\tau_{n-1} = k_{n-1}(q_{n-2}) + d_{n-1}(\dot{q}_{n-2})$$

with i from 0 to $n-3$.

Eventually, the model can be re-written as:

$$J_m\ddot{\theta} + d_m\dot{\theta} + \sum_{h=0}^{n-2}m_h((h+1)l)^2\ddot{q}_h = \tau_m - \tau_0$$

$$\tau_0 = k_0(\theta - q_0)$$

$$j_i\ddot{q}_i + \sum_{h=i+1}^{n-2}m_h((h-i)l)^2\ddot{q}_h = \tau_i - \tau_{i+1} \qquad (3.2)$$

$$\tau_{i+1} = k_{i+1}(q_i - q_{i+1}) + d_{i+1}(\dot{q}_i - \dot{q}_{i+1})$$

$$j_{n-2}\ddot{q}_{n-2} = \tau_{n-2} - \tau_{n-1}$$

$$\tau_{n-1} = k_{n-1}(q_{n-2}) + d_{n-1}(\dot{q}_{n-2})$$

Using the Laplace transform, the system dynamics is derived as

$$s\theta = \frac{\tau_m - \tau_0 - \sum_{h=0}^{n-2}m_h((h+1)l)^2 s^2 q_h}{J_m s + d_m}$$

$$\tau_0 = \frac{k_0}{s}(s\theta - sq_0)$$

$$sq_i = \frac{\tau_i - \tau_{i+1} - \sum_{h=i+1}^{n-2}m_h((h-i)l)^2 s^2 q_h}{j_i s} \qquad (3.3)$$

$$\tau_{i+1} = \frac{k_{i+1}}{s}(sq_i - sq_{i+1}) + d_{i+1}(sq_i - sq_{i+1})$$

$$sq_{n-2} = \frac{\tau_{n-2} - \tau_{n-1}}{j_{n-2}s}$$

$$\tau_{n-1} = \frac{k_{n-1}}{s}sq_{n-2} + d_{n-1}sq_{n-2}$$

The dynamics of the system represented in Figure 3.1 can be described by splitting

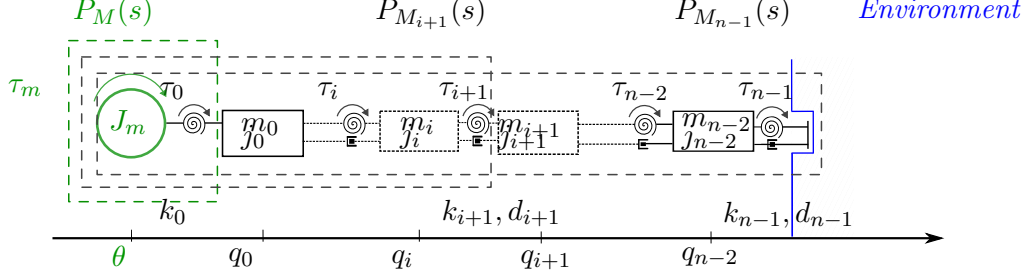the actuator and link-environment models into $n-1$ subsystems $P_{M_i}(s)$ defining the relation between τ_m and τ_i.

Figure 3.2: Model subsystems

The τ_0 signal represents the deformation at the base of the link, τ_i the deformation of the link measured in different (non-collocated) locations of the link and τ_{n-1} the deformation at the tip of the link. Practically, these signals can be measured using deformation sensors such as strain gauges, providing a measure of the link interaction torque with different levels of collocation, as shown in Figure 3.2. P_{M_i} is calculated by multiplying the transfer function $G_1(s)$, which represents the dynamics between the motor torque τ_m and the interaction torque with the environment τ_{n-1} and the transfer function $G_2(s)$, which describes the dynamics between the torque sensor signals τ_i and the interaction torque with the environment τ_{n-1}. These transfer functions are derived following the steps reported in Table 3.1.

3.3   Case Study

In this chapter, robotic surgery is considered as the application of interest, and a laparoscopic tool used in minimally invasive surgery is selected as an example of a flexible link. The laparoscopic tool is an empty cylinder 380 millimetres long, with an external radius of 4.1 millimetres and a thickness of 0.85 millimetres. It is made of a fibre-reinforced composite that is characterized by a Young modulus E, Shear modulus S and Poisson ratio ν_{RATIO} equals, respectively, to 54.48 GPa, 11.41 GPa and 0.32 GPa.

The laparoscopic tool is driven by two different motor models (Maxon model EC45 and Maxon model DCX22L with a reduction gearbox of 1000 and 103, respectively). Table 3.2 reports parameters related to these two application cases.

In order to define a suitable order of the lumped approximant, i.e. how many link segments we need to consider, we implemented lumped approximants with different orders and, for each order, we computed a common stability parameter: the gain margin Gm in order to check how the approximation truncation affects stability. Results are reported in Tables 3.3, 3.4, considering a non-collocated sensor placed at a distance L from the motor shaft (on the tip of the instrument).

It is possible to observe that, for both cases, as the number of segments increases, the gain margin Gm converges to a plateau and the stability parameter

Algebric steps to compute $G_1(s) = \frac{\tau_{n-1}(s)}{\tau_m(s)}$	
Substitutions	**Leads to**
$s\theta$ in τ_0	$\tau_0(sq_i, sq_{n-2}, \tau_m)$
τ_0 in sq_i	$sq_i(\tau_i, \tau_m)$
sq_i in τ_{i+1}	$\tau_{i+1}(sq_{i+1}, sq_{n-2}, \tau_m)$
τ_{i+1} in sq_{i+1}	$sq_{i+1}(\tau_{n-1}, \tau_m)$
sq_{n-1} in τ_{n-1}	$\tau_{n-1}(\tau_m)$

Algebric steps to compute $G_2(s) = \frac{\tau_i(s)}{\tau_{n-1}(s)}$	
Substitutions	**Leads to**
$s\tau_i$ in τ_{i+1}	$\tau_{i+1}(sq_{i+1}, sq_{n-2}, \tau_i)$
τ_{i+1} in sq_{i+1}	$sq_{i+1}(\tau_{i+1}, \tau_i)$
sq_{i+1} in τ_{n-1}	$\tau_{n-1}(\tau_{i+1})$

Table 3.1: Algorithm to find system dynamics

		EC45	DCX22L
Motor Parameters	J_m $[kgm^2]$	0.133	0.0104
	d_m $[\frac{Nms}{rad}]$	0.8	0.1
Motor Gearbox	k_0 $[\frac{Nm}{rad}]$	1000	103
Link Parameters	L $[m]$	0.38	0.38
	M $[kg]$	0.1	0.1
	K $[\frac{Nm}{rad}]$	61.07	61.07
	D $[\frac{Nms}{rad}]$	0.01	0.01

Table 3.2: Physical parameters related to the considered case studies

does not significantly change for orders higher than 40 (20 masses). Thus, we chose 25 as a suitable number of segments that reasonably approximates the continuum system.

We used the symbolic software library described before to derive such high-order frequency model: a lumped 50-order approximant of the continuum mechanics model. The order can be computed as the number of segments × 2 plus 2 to represent the motor dynamics.

Case Maxon EC45: System Gain Margin Gm					
N°segments	6	8	10	20	30
Gm	38.25	41.93	44.30	49.62	51.77

Table 3.3: Laparoscopic Tool driven by Maxon EC45 motor - Gain Margin Gm with sensor at L

Case Maxon DCX22L: System Gain Margin Gm					
N°segments	6	8	10	20	30
Gm	3.11	3.52	3.79	4.43	4.70

Table 3.4: Laparoscopic Tool driven by Maxon DCX22L motor - Gain Margin Gm with sensor at L

3.4 Passivity and stability analysis

In this section, we analyzed the passivity and stability of the 50-order approximant of the laparoscopic tool driven by two different motor models (Maxon model EC45 and Maxon model DCX22L with reduction gearbox of 1000 and 103, respectively). Table 3.2 reports parameters related to these two application cases.

Regarding stability, the system dynamics $G(s) = \frac{\tau_i(s)}{\tau_m(s)}$ is computed considering the action of non-collocated feedback and considering a stiff environment. We decided to consider a stiff environment because it is the most challenging case for stability [58, 11]. Also, characterizing a soft environment is not simple, as many different cases should be considered. Figure 3.3 shows the Bode diagrams of $G(s)$ for the two cases of study reported in Table 3.2. One can observe that the system has a first low-frequency peak $\omega_S = \sqrt{K/J_m}$ given by the motor inertia and the link stiffness parameters. The other peaks correspond to the link resonances, and one can observe several link harmonics. Depending on the motor parameters, the first resonance may significantly vary in frequency and amplitude, but the Bode diagram retains a similar shape. In addition, the variation of the position of the sensor location along the link affects the system's dynamics. Moving the sensor location towards the tip of the link leads to changes in the Bode diagram. In particular, it is noted that the zeros of the system can be lost. Variations in the amplitude and phase in the Bode diagram evidence this phenomenon. As expected, the poles of the system remain the same. They are stable as they reflect the intrinsic passivity of the system itself.

3.4.1 Stability

To evaluate the stability of the system $G(s)$ under the action of non-collocated feedback, we analyzed the minimum distance that the Nyquist diagram of the
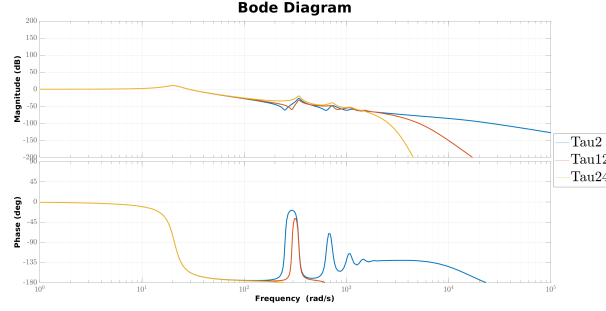
(a) Bode Diagram - Case EC45 motor
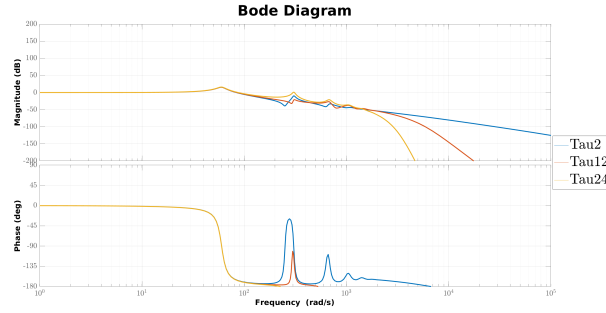

(b) Bode Diagram - Case DCX22L motor

Figure 3.3: Bode Diagrams - Maxon models EC45 e DCX22L

system takes from the critical point in the complex plane. The critical point is placed at the coordinate -1 on the real axis. Being all poles stable, crossing this point leads to system instability. To compute such distance (which actually measures the "distance from the instability"), we use the following expression:

$$\text{min\_distance} = \frac{1}{\|\frac{1}{k_p G(j\omega)+1}\|_\infty}. \tag{3.4}$$

When the system is stable, this value provides an indicator of the stability robustness. Low values correspond to oscillating behaviour where at least one closed-loop pole is close to the unstable area $Re(s) > 0$. In this work, we define an acceptability threshold based on the value of the minimum distance (Eq. 3.4) set to 0.15 which emerged from experimental observations. The system is considered too oscillating if the minimum distance (Eq. 3.4) is below this threshold.

For the specific application cases of the laparoscopic tool in robotic surgery (system's parameters are reported in Table 3.2), we considered a proportional controller with $k_p \in [1, 2, 3, 5, 10, 20]$. Considering these gain values, Figure 3.4 shows the stability index (3.4) related to non-collocated force feedback when the laparoscopic instrument is in contact with a rigid environment. We consider 24 sensor locations across the line. In case of system instability, i.e. when the Nyquist diagram crosses -1, the index is set to 0. Thus, in Figure 3.4, the value 0 means
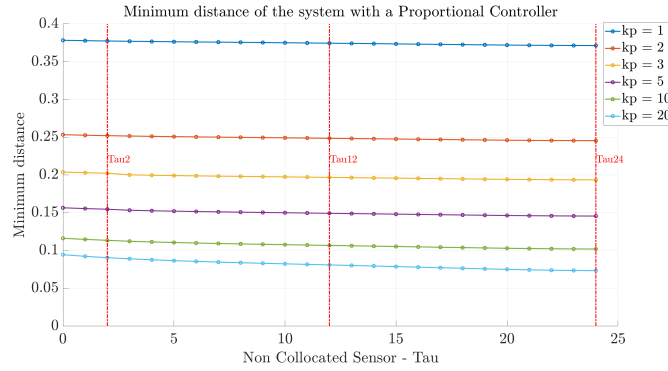
(a) Minimum distance with motor EC45
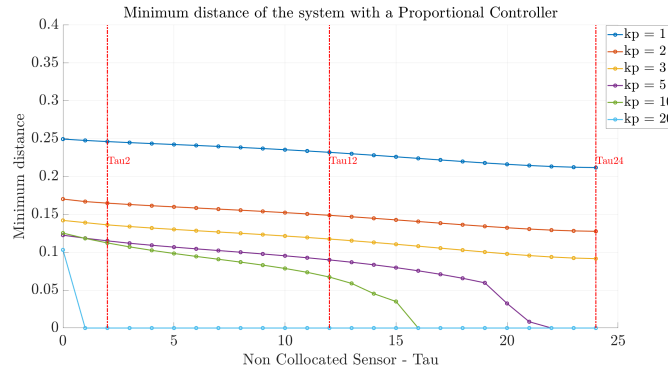
(b) Minimum distance with motor DCX22L

Figure 3.4: Stability Analysis considering the minimum distance

instability and not marginal stability.

3.4.2 Passivity

In this section, we describe the computation of the system impedance $I(s)$ to the environment port $(\tau_{n-1}, \dot{q}_{n-1})$ under the feedback action of non-collocated proportional force controllers for the two case studies in Table 3.2.
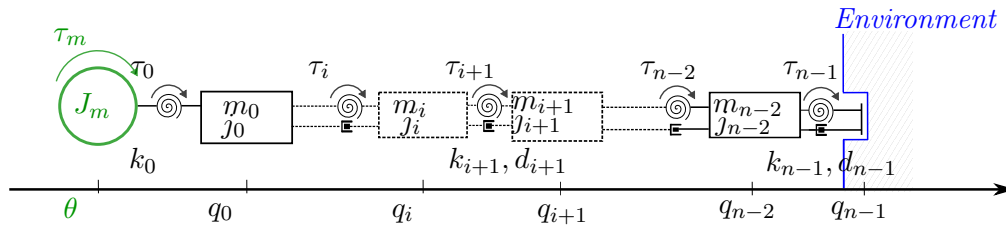

Figure 3.5: Modelling as discrete blocks

We consider the dynamics of the 50-order lumped model represented in Figure 3.5, approximants the continuum mechanics model in Fig. 2.1.

$$J_m\ddot{\theta} + d_m\dot{\theta} + \sum_{h=0}^{n-2} m_h((h+1)l)^2\ddot{q}_h = \tau_m - \tau_0$$

$$\tau_0 = k_0(\theta - q_0)$$

$$j_i\ddot{q}_i + \sum_{h=i+1}^{n-2} m_h((h-i)l)^2\ddot{q}_h = \tau_i - \tau_{i+1} \tag{3.5}$$

$$\tau_{i+1} = k_{i+1}(q_i - q_{i+1}) + d_{i+1}(\dot{q}_i - \dot{q}_{i+1})$$

$$j_{n-2}\ddot{q}_{n-2} = \tau_{n-2} - \tau_{n-1}$$

$$\tau_{n-1} = k_{n-1}(q_{n-2} - q_{n-1}) + d_{n-1}(\dot{q}_{n-2} - \dot{q}_{n-1})$$

Using the Laplace transform, the system dynamics can be expressed as

$$s\theta = \frac{\tau_m - \tau_0 - \sum_{h=0}^{n-2} m_h((h+1)l)^2 s^2 q_h}{J_m s + d_m}$$

$$\tau_0 = \frac{k_0}{s}(s\theta - sq_0)$$

$$sq_i = \frac{\tau_i - \tau_{i+1} - \sum_{h=i+1}^{n-2} m_h((h-i)l)^2 s^2 q_h}{j_i s} \tag{3.6}$$

$$\tau_{i+1} = \frac{k_{i+1}}{s}(sq_i - sq_{i+1}) + d_{i+1}(sq_i - sq_{i+1})$$

$$sq_{n-2} = \frac{\tau_{n-2} - \tau_{n-1}}{j_{n-2} s}$$

$$\tau_{n-1} = \frac{k_{n-1}}{s}(sq_{n-2} - sq_{n-1}) + d_{n-1}(sq_{n-2} - sq_{n-1})$$

The passivity at the environment port $(\tau_{n-1}, \dot{q}_{n-1}) = (\tau_{24}, \dot{q}_{24})$ was calculated using a symbolic software library implemented in Python [57] that follows the steps reported in Table 3.5.

Algebric steps to compute $I(s)$	
Substitution	**Leads to**
$s\theta$ in τ_0	$\tau_0(sq_i, sq_{n-2}, \tau_m)$
τ_0 in τ_{i+1}	$\tau_{i+1}(sq_i, sq_{n-2}, \tau_m)$
sq_i in τ_{i+1}	$\tau_{i+1}(sq_{i+1}, sq_{n-2}, \tau_m)$
τ_{i+1} in τ_{n-1}	$\tau_{n-1}(sq_{n-2}, sq_{n-1}, \tau_m)$
sq_{n-2} in τ_{n-1}	$\tau_{n-1}(sq_{n-1}, \tau_m)$

Table 3.5: steps to find impedance I(s)

We tested the passivity of the transfer function $I(s)$ considering 24 sensor

locations along the link, which provide a non-collocated feedback. For each case, we search for the maximum proportional gain k_p, which retains passivity.
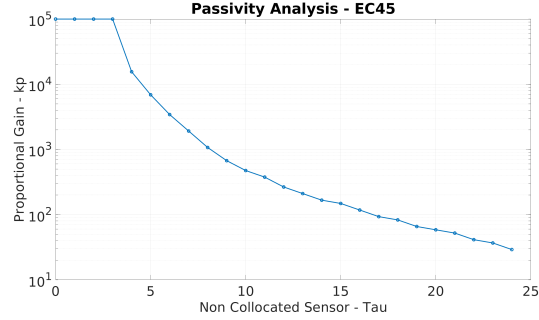
(a) Maximum k_p gain guaranteeing passivity - Case study with the EC45 motor

(b) Maximum k_p gain guaranteeing passivity - Case study with the DCX22L motor

Figure 3.6: Passivity Analysis - Maxon models EC45 e DCX22L

The identified gain was found through a trial and error approach, gradually increasing the value of the proportional parameter k_p and verifying the system passivity. Results are reported in Table 3.6 and in Figure 3.6 on a logaritmic scale. One can observe that the maximum gain retain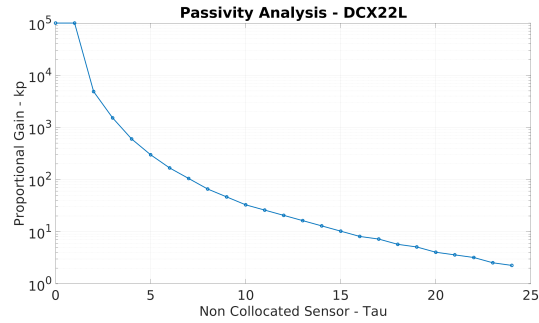ing passivity dramatically drops as the sensor location approaches the link's tip. Comparing the two cases of study, one can see that the motor inertia significantly affects the maximum allowable gain. For instance, by placing the sensor at the tip, one can reach $k_p = 29$ in the case of the EC45 motor and $k_p = 2.3$ in the case of the DCX22L motor. The experimental validation will show coherence with these values. We highlight that passivity cannot define the performance do the closed-loop system. This implies that a passive system can stably interact with a passive environment but eventually can show extremely bad performance, e.g. with high overshoots and oscillations. This is particularly true in the case of the "high" gains reported in Figure 3.6.

Maximum Proportional Gain k_p - Passivity Index		
	EC45 Motor	DCX22L Motor
Feedback at τ_1	10^5	10^5
Feedback at τ_2	10^5	4862
Feedback at τ_3	10^5	1519
Feedback at τ_4	15556	599
Feedback at τ_5	6892	298
Feedback at τ_6	3430	166
Feedback at τ_7	1917	104
Feedback at τ_8	1072	65
Feedback at τ_9	673	46
Feedback at τ_{10}	475	32
Feedback at τ_{11}	376	25
Feedback at τ_{12}	265	20
Feedback at τ_{13}	210	16
Feedback at τ_{14}	166	12
Feedback at τ_{15}	148	10
Feedback at τ_{16}	117	8.1
Feedback at τ_{17}	93	7.2
Feedback at τ_{18}	83	5.0
Feedback at τ_{19}	65	4.5
Feedback at τ_{20}	58	4.0
Feedback at τ_{21}	52	3.6
Feedback at τ_{22}	41	3.2
Feedback at τ_{23}	36	2.5
Feedback at τ_{24}	29	2.3

Table 3.6: Maximum k_p gain guaranteeing passivity

3.5   Experimental Validation

A laparoscopic tool used in minimally invasive surgery is selected as an example of a flexible link. The laparoscopic tool is an empty cylinder made of a fibre-reinforced composite. Link parameters are reported in Table 3.2. The link is arranged on a custom test bed in such a way that the motor torque produces a link bending deformation when pushing a kinematic constraint, the metal cube in Figure 3.7. A rigid kinematic constraint is selected as a worst-case passive environment since stability is more challenging to observe in stiff environments [58, 11]. In this configuration, the system can be modelled exactly as in Figures 2.1 and 3.1. We chose two motors: model Maxon EC45 and model Maxon DCX22L with reduction gearbox of 1000 and 103, respectively.

The link deformation is measured using strain gauges in half-bridge configuration arranged at different positions along the link. Of course, we cannot arrange sensors exactly at the clamping point because of mechanical accessibility issues and existing edge effects. The following experiments are related to different sensor arrangements considering small ε, $\frac{L}{2}$ and L. The strain gauges are connected to a custom electronic board, which includes a Wheatstone bridge and an amplification stage.

The proportional control algorithm is implemented in C++ on a custom microcontroller running the control task with an execution frequency of 2000 Hz. More details on the implementation can be found in [59].

Figures 3.8 and 3.9 show the torque step response of the proportional force controller based on link deformation feedback at the link base for $k_p \in [1, 2, 3, 5, 10, 20]$, the same gain values considered in section 3.4.1. The torque reference τ_{ref} is shown in blue, and the measured torque τ is in red. Plots 3.10, 3.11, 3.12 and 3.13 show the same kind of responses, considering link deformation feedback at the middle point and at the tip of the link for both motors.
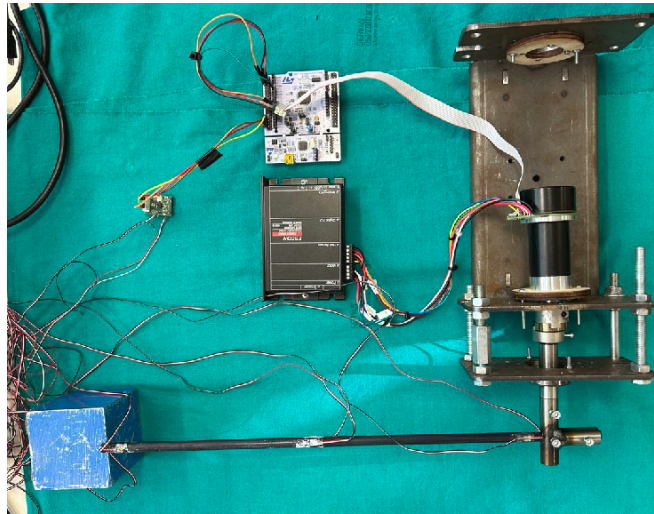
(a) Setup with Maxon motor EC45: the laparoscopic tool is
arranged on a custom test bed in such a way that the motor
torque produces a link bending deformation when pushing a
kinematic constraint, the rigid cube
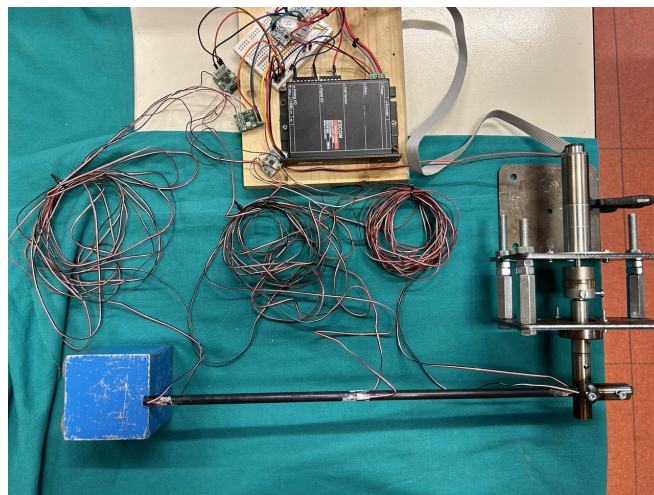
(b) Setup with Maxon motor DCX22L: the laparoscopic tool
is arranged on a custom test bed in such a way that the motor
torque produces a link bending deformation when pushing a
kinematic constraint, the rigid cube
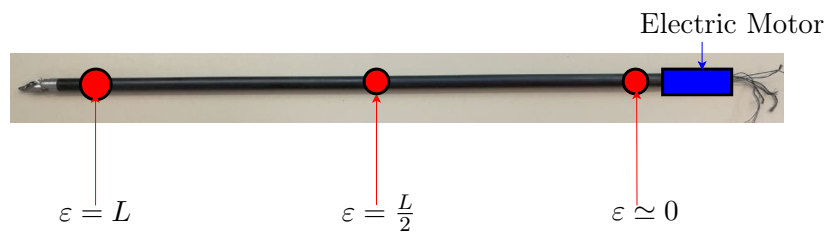
(c) Sensor (strain gauges) arrangements on the flexible link in order to mea-
sure the deformation/torque in different locations

Figure 3.7: The experimental setup with EC45 and DXC22L motors and sensor
arrangements on the flexible link

(a) Step Response with $k_p = 1$

(b) Step Response with $k_p = 2$

(c) Step Response with $k_p = 3$

(d) Step Response with $k_p = 5$

(e) Step Response with $k_p = 10$

(f) Step Response with $k_p = 20$

Figure 3.8: Step Response with torque feedback at the link base with motor EC45

(a) Step Response with $k_p = 1$

(b) Step Response with $k_p = 2$
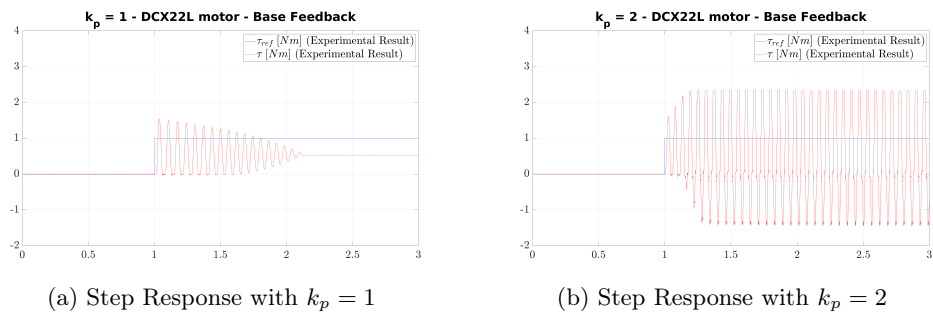
Figure 3.9: Step Response with torque feedback at the link base with motor DCX22L
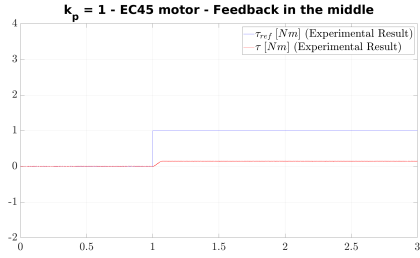
(a) Step Response with $k_p = 1$ (b) Step Response with $k_p = 2$
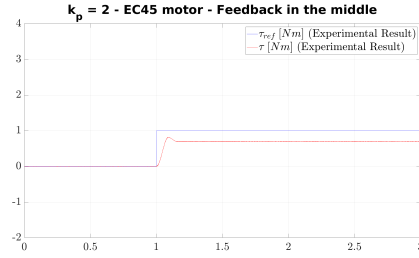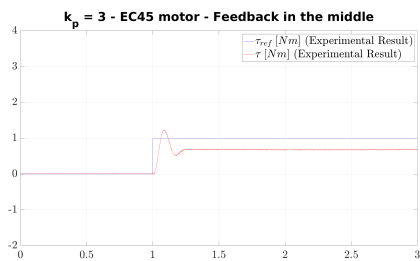
(c) Step Response with $k_p = 3$ (d) Step Response with $k_p = 5$
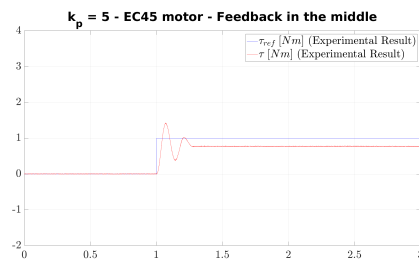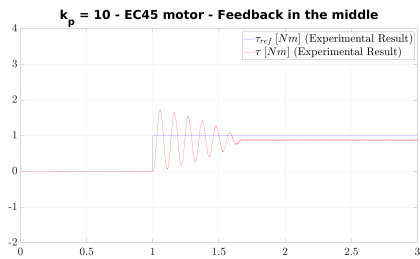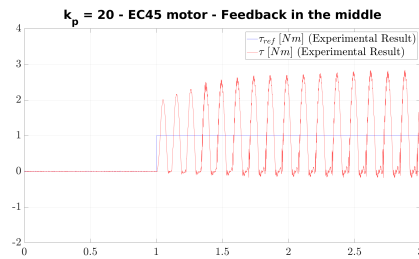
(e) Step Response with $k_p = 10$ (f) Step Response with $k_p = 20$

Figure 3.10: Step Response with torque feedback at $\frac{L}{2}$ with motor EC45
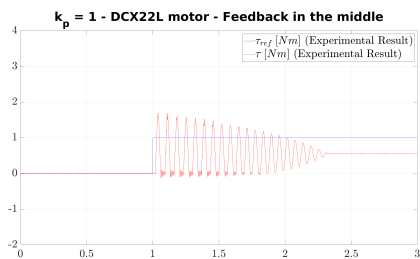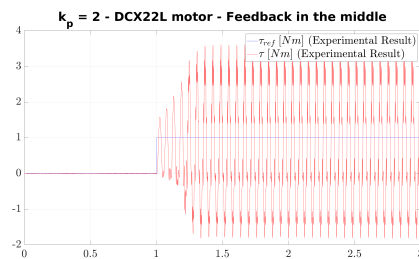
(a) Step Response with $k_p = 1$ (b) Step Response with $k_p = 2$

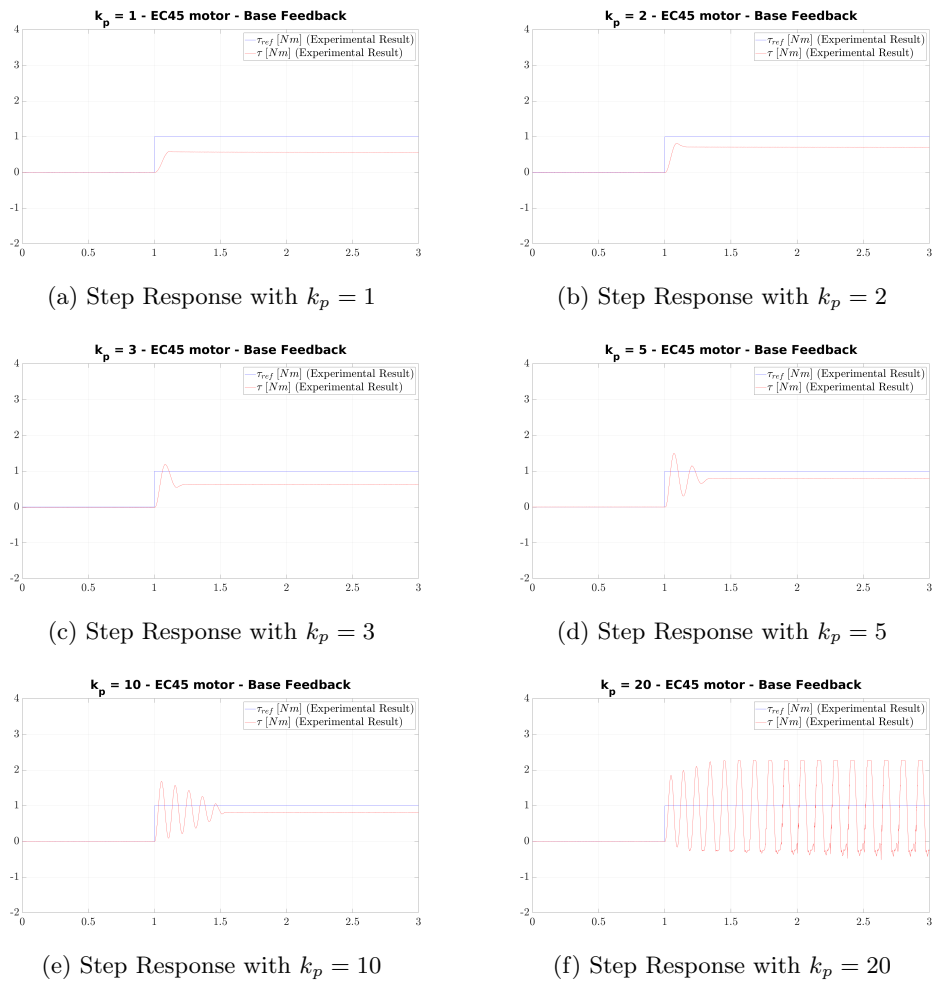Figure 3.11: Step Response with torque feedback at $\frac{L}{2}$ with motor DCX22L
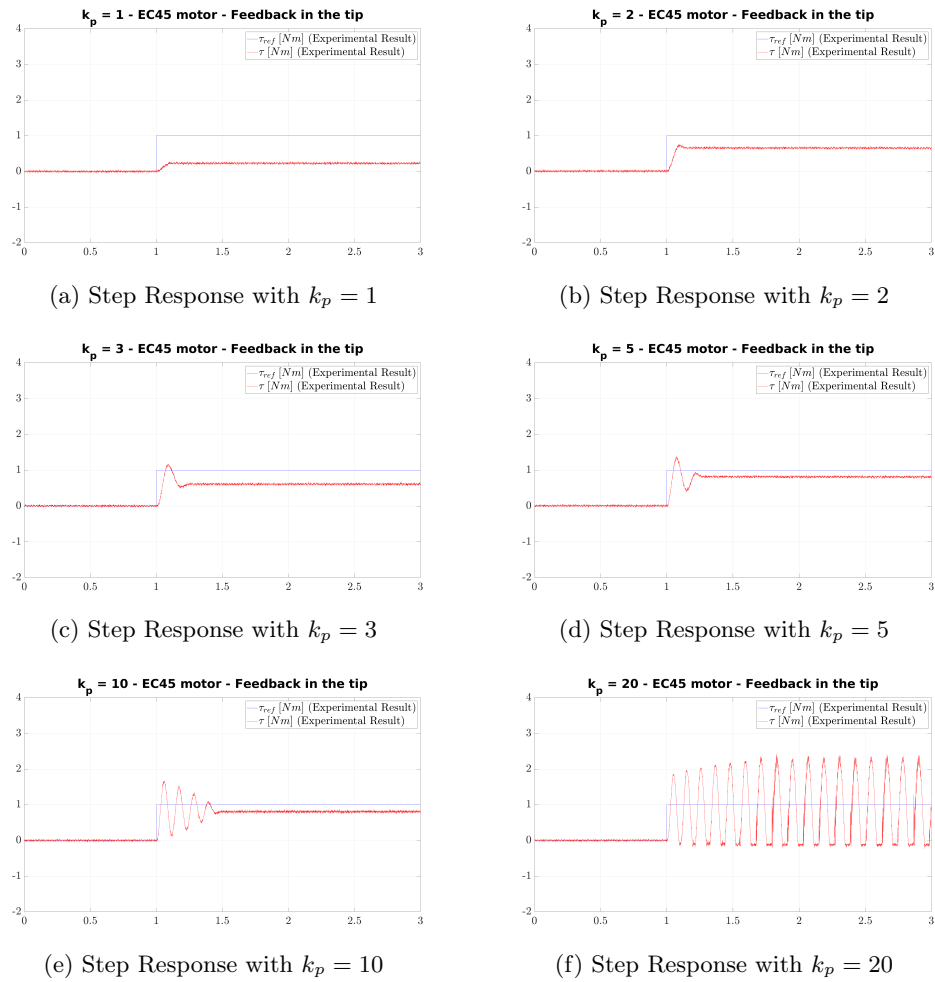
Figure 3.12: Step Response with torque feedback at the L with motor EC45
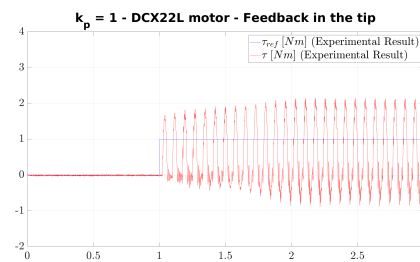
(a) Step Response with $k_p = 1$

Figure 3.13: Step Response with torque feedback at L with motor DCX22L. The case $k_p = 2$ is unstable and not reported.

3.5.1   Discussion on passivity

It is known that experimentally validating passivity conditions is a hard task because of the existing discrepancies between theory and practice due to neglected dynamics and discretization [60]. However, it's interesting to observe that when the feedback sensor is located on the tip, the theoretical passivity constraint defines $k_p \leq 29$ and $k_p \leq 2.3$ for EC45 and DCX22L motors, respectively. Similar limits can be observed in the practice. As reported in Figure 3.6, $k_p = 20$ leads to marginal stability for the EC45 motor while $k_p = 1$ leads to marginal stability for the DCX22L motor. Besides confirming coherence between theoretical and experimental results, this observation highlights that motor dynamics has a significant impact on passivity, as already observed in section 3.4.2.

3.5.2   Discussion on stability

Similarly to the previous section, the motor dynamics has a significant effect also on stability. Theoretically, this can be observed by comparing plots (a) and (b) in Fig. 3.4. Regarding the case study with the EC45 motor, quite surprising we didn't notice significant differences on stability margins due to the level of collocation: the plots in Figure 3.8 are qualitatively similar to plots in Figure 3.10 and to those in Figure 3.12. Instead, the case study with DCX22L motor seems to be much more sensitive to non-collocation issue: this can be observed by looking at differences between plots in Figures 3.11, 3.13. For instance, using feedback from the tip we couldn't reach a stable response with $k_p = 2$, whereas the same gain could be used for base-link and mid-link feedback. Both these observations agree with the trends in Figure 3.4a (where the minimum distance is almost constant) and in Figure 3.4b (where the minimum distance decreases when approaching the tip). As a final observation, one can see that the most oscillating responses occur when the minimum distance values reported in Figure 3.4 approach the value 0.15. This means that the minimum distance (Eq. 3.4) can be an effective indicator of stability margins.

3.6   Conclusion

In this chapter, we developed a symbolic library to derive a high-order lumped approximant for a common surgical instrument (a laparoscopic tool) in order to analyse related passivity and stability properties. Considering proportional force feedback measured at different locations, we found, as expected, that the passivity constraint is more strict as the sensor location approaches the instrument tip, especially in the case of a low-inertia motor. Interestingly, the passivity constraint found at the tip is coherent with maximum allowable gain during real-world experiments on a stiff environment. Regarding stability, we found that the system is less sensitive to non-collocation, especially in the case of high-inertia motors. In the case of low-inertia motors, non-colocation can become an issue. Experimental results agree with these findings.

In this case study, we consider the mass, length, and stiffness of the laparo-scopic tool, focusing our analysis on minimally invasive robotic surgery applications. However, the developed solver is versatile and can be used to analyze the passivity and stability margins of various systems depending on the context of interest.

Part II

Needle Insertion and deflection estimation

Chapter 4

Needle Insertion Models - A Comparison between Kinematic Models for Robotic Needle Insertion with Application into Transperineal Prostate Biopsy

4.1   Background and state of art

One of the main causes of death for men is prostate cancer (PCa), which is the second most common cancer after breast cancer [61]. Epidemiologic studies of prostate cancer have revealed numerous ways in which individual biology and lifestyle factors, such as older age and family history, influence the risk of developing prostate cancer and survival from this disease [61]. Prostate cancer is a clinically heterogeneous disease; some men have an aggressive form, and most others have a slow-growing or indolent form of the disease. The successful treatment of high-risk patients and avoiding overtreatment in low-risk patients depends greatly on early and accurate PCa detection. Needle biopsy is the most reliable technique for detecting PCa and estimating its aggressiveness [62]. Robot-assisted needle insertion can improve the accuracy of this procedure, helping to place the tip of the needle safely and accurately without damaging tissues, organs, or vessels. Unfortunately, precise needle placement is difficult to accomplish in real practice because of tissue heterogeneity, needle bending, and tissue/organ deformation and movement. As a result, modelling the interaction between the needle and the tissue is a critical requirement for robotic needle insertion.

During a transperineal prostate biopsy, the physician uses ultrasound images to guide the needle from the perineum entry points towards the selected target spots [63]. Due to several reasons, including economic cost, needles with a bevelled tip are the most commonly used. Unfortunately, when these needles cross

the prostate, they deflect due to tissue forces acting on the bevelled tip, producing an unwanted deflection and degrading the accuracy of the system. The advantage of a bevelled tip is that it causes less tissue damage than a symmetric tip and that curved trajectories can be used to avoid delicate tissues, such as bones and blood vessels, which are located between practical entry sites and possible targets. During a transperineal prostate biopsy, the surgeon can compensate for the deformation of the needle by twisting the instrument to reach the lesion on the prostate. If we consider robotic automated insertions of needle for prostate biopsy, needle twisting is not possible so it is necessary to plan the trajectory from the entry points to the points to be sampled on the organ, considering the deformation of the needle and surrounding tissue. Thus, modelling the needle deflection path becomes of paramount importance, and several authors have addressed this topic over the years [64, 65]. Previous reports depict three different formalisms to model needle deflection: kinematic models, finite elements (FE) models, and quasi-static approximated mechanical models.

The first research team that presented a kinematic model is *Park et al.* [66]. The authors developed a simple nonholonomic 2D unicycle model to describe how an ideal needle with a bevelled tip moves through a firm tissue. One year later, *Webster et al.* [67] introduced a nonholonomic 3D bicycle-like model for steering flexible bevelled tip needles. This model describes the same circular arc of the unicycle model but differs when an axial rotation of the needle occurs between two straight insertions. Both models assume that the tissue does not deform. Inserting the needle into a stationary tissue causes negligible deformation of the surroundings as the needle bends, so the modelling is limited to the motion of the tip. However, if the tissue is not stiff, as the instrument bends, the tissue is compressed. This leads the needle tip to follow a non-circular path. For this reason, *Fallahi et al.* [68] proposed an extension to the bicycle model of *Webster et al.* [67]. In this model, the back wheel is replaced with an omnidirectional wheel that can move sideways, allowing the needle to follow a path with a variable radius of curvature. The principal limitation of this model is that only the position of the needle tip is estimated, and all forces applied by the tissue along the needle shaft cannot be calculated. This information is critical to account for target displacement, so a finite elements model has been proposed.

DiMaio et al. and *Goksel et al.* were the first to use FE to model the needle-tissue interaction [69, 70]. Initially, a FE model was used to simulate the deflection of a needle in free space and take geometric nonlinearities into account [71]. Then, to model the effects of the surrounding tissue, a linear elastic tissue model was used. The geometry of the soft tissue is typically defined using a mesh composed of 2D or 3D polyhedral elements that are deformed as the needle cuts and advances into tissue [72]. *Alterovitz et al.* presented a 2-D finite element method of needle insertion considering the effect of tip bevel to perform motion planning for steerable needles without the need for explicit position feedback [73, 74, 75] and then *Chentanez et al.* expanded the model in 3-D [76]. In *Maghsoudi and Jahed* [77, 78], FEM is also used to estimate the needle-tissue contact forces that
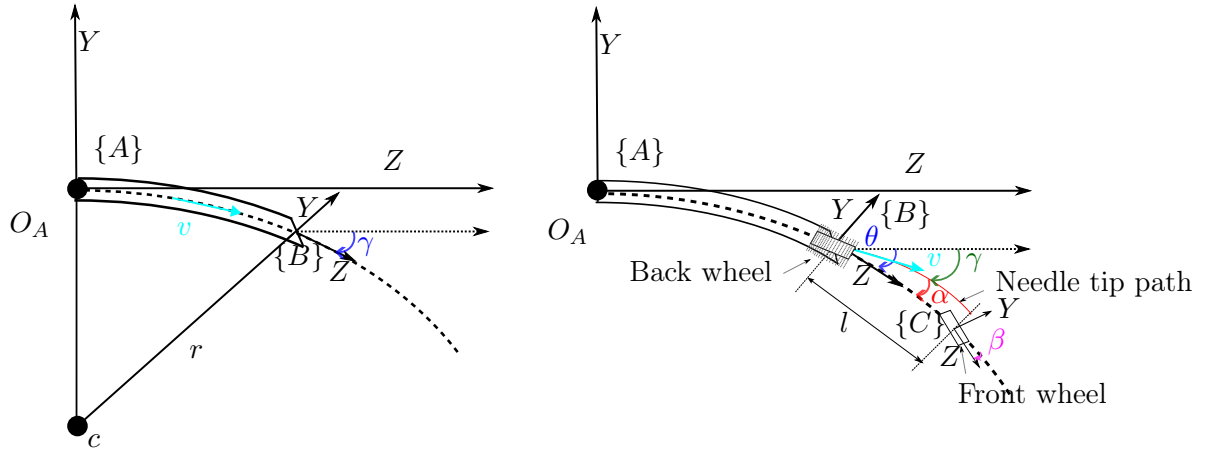
Figure 4.1: Unicycle and Extended bicycle models of a bevelled tip needle

result from tissue deformation. Other applications of FEM include modelling the effect of external forces applied to the tissue to shift the target location and improve needle targeting accuracy [79]. *Mallapragada, Sarkar, and Podder* used this concept for breast biopsy procedures [80]. It can also be used to enhance target accessibility by pushing obstacles and sensitive tissue away from the needle path. Because of their high flexibility, FE-based models can effectively describe the behaviour of needles in tissue in the presence of external perturbations.
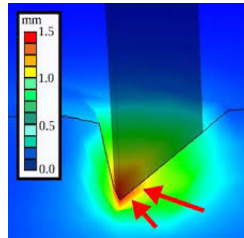
Figure 4.2: Finite Elements Simulation of Needle Insertion

Employing a comprehensive FE model of tissue can be very time-consuming and not suitable for real-time control [81, 71]. More computationally efficient models may come at the expense of reduced accuracy [70]. Furthermore, certain parameters in FEM simulators may not relate to physical properties that can be experimentally and independently measured. In this regard, the right tradeoff may be a quasi-static, approximated mechanical model.

The needle's mechanical behaviour during insertion depends on the coupled deformations of both the needle shaft and the surrounding tissue. The interaction can be classified into four distinct phases: tissue puncturing, tissue cutting, needle-tissue friction, and tissue deformation [82, 81, 83].

- Tissue puncturing happens at the initial contact between the needle tip and

the tissue. It starts by deforming the tissue and continues until the contact force reaches its maximum and a crack is formed on the tissue surface. Puncturing results in a relatively large force at the needle tip that drops when the needle tip enters the tissue [84, 82, 83].

- Tissue cutting: As the needle tip further advances into tissue, it displaces the immediately surrounding tissue and the crack grows, creating the effect of tissue cutting [85]. Considering the tissue as an elastic medium, tissue compression at the needle tip leads to a distributed load being applied on both sides of the needle tip that, due to the asymmetric bevel tip, results from a net force normal to the needle shaft [81].

- Friction is applied tangentially to the needle shaft against the motion of the needle. Three regimes of interest exist: (1) static friction while the needle is in a steady state; (2) transition from the steady state to the sliding state; and (3) velocity-dependent forces as the needle moves [86, 87]. Friction contributes to tissue displacement along the needle shaft but does not have a significant effect on needle deflection [81].

- Tissue deformation: the force Q applied at the needle tip makes the needle bend and follow a curved trajectory as it moves. Consequently, the deformed needle shaft compresses the surrounding tissue, which in turn applies forces to the needle shaft and influences the tip trajectory [85]. Tissue reaction forces are applied perpendicularly to the contact surface between the needle shaft and the tissue. Therefore, needle deflection and tissue deformation are coupled effects that influence each other [88, 89].
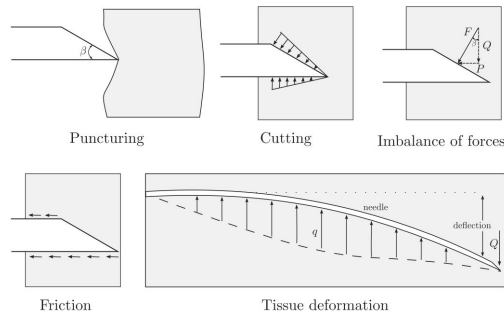

Figure 4.3: Needle insertion fases

As a bevelled-tip needle advances in soft tissue, the needle tip cuts and displaces the tissue, and a force F is created normal to the bevel. The resultant vertical force $Q = F\cos(\phi)$, where ϕ is the bevel angle, causes the needle to bend and deform the surrounding tissue, resulting in the distributed load q being applied to the needle shaft.

To account for the fact that needle deflection and tissue deformation are coupled effects, researchers have adopted beam theories to develop fundamental mechanics-based models of needles in tissue [86, 71, 87, 90]. *Goksel et al.* were among the first to develop mechanics-based models of a needle in free space subjected to a constant load applied at the tip. Tissue deformation is modelled by contact forces that evolve as the needle bends and compresses the tissue. The Euler-Bernoulli equation describes the relationship between the beam's deflection v at a point z along its shaft and the applied load q as dz.

$$\frac{d^2}{dz^2}(EI\frac{d^2v}{dz^2}) = q \tag{4.1}$$

where EI is the needle's flexural rigidity, and q is a distributed load that acts anywhere along the needle shaft. Integrating both sides of (2.1) with respect to the position z gives the shear force acting on the needle. To the obtained shear force, the tip force Q is added, and the result is further integrated until the deflection v(t,z) is obtained.
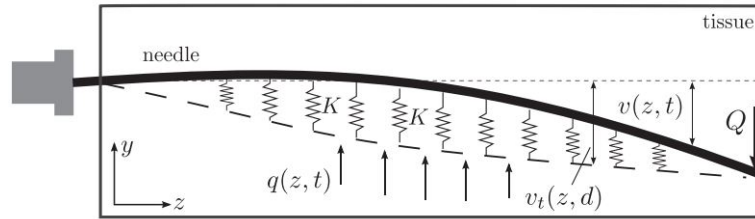
Figure 4.4: Forces acting on the needle shaft

We have also *Misra et al.* that used an energy-based formulation for a beam which is in contact with a nonlinear hyperplastic tissue to simulate needle steering [81]. This model accounts for lateral and axial deflection of the needle, tissue deformation, and input force applied at the needle base. Later, the same model was extended to include needle rotation during needle insertion [91]. *Khadem et al.* used a dynamic beam theory to study the effects of insertion velocity on needle deflection [87]. *Reed et al.* studied the effects of torsional friction on needle deflection dynamics [92]. They developed an estimator that allows the needle to maintain motion in a prescribed plane. The design of needle steering planners and most types of feedback controllers requires a model of the needle-tissue interaction that predicts the needle tip position given the inputs at the needle base, such as insertion velocity and needle axial rotation.

In the end, in a recent MICCAI conference, *Daniel Glozman and Moshe Shoham* [93, 94] have presented a simplified virtual spring model that allowed fast path planning and real-time tracking for the needle insertion procedure. They assumed small tissue displacement and a linear lateral force response. So the tissue forces on the needle could be modelled as lateral virtual springs distributed along the needle curve plus friction forces tangent to the needle's longitudinal axis.

Modelling of a flexible needle was based on the assumption of quasistatic motion, so the needle is in an equilibrium state at each step. They adopted the nodal degrees of freedom from finite elements theory, in which the coordinates were specifically identified with a single nodal point and represented a displacement or rotation. A third-degree polynomial was used to calculate the displacement of each element. A compromise had to be made between computation efficiency and model accuracy.

In this Chapter, we propose an experimental comparison of kinematic models evaluating their accuracy in the context of a transperinary prostate biopsy, considering different needle insertion speeds and different organ stiffnesses. We adapted Fallahi's extended bicycle model to suit our application. To enable a comparative experimental analysis of models, we develop:

1. identification procedures to estimate model parameters,

2. a vision algorithm based on an RGB-D camera system to reconstruct the needle tip position at each insertion step,

3. four transparent phantoms with different stiffnesses which allow the use of standard cameras to collect needle insertion frames.

The Chapter is organised as follows: Section 4.2 provides the theoretical background on kinematic models and explores in detail the considered models. Section 4.3 describes the proposed method, including the vision algorithm that recognizes and tracks the needle, the robotic setup and the phantom design. Sections 4.4 and 4.5 describe the experimental results and their discussion and Section 4.6 reports our conclusions and future works.

The results of this chapter are reported in "A Comparison between Kinematic Models for Robotic Needle Insertion with Application into Transperineal Prostate Biopsy" published to "Technologies 2024, 12, 33", `https://doi.org/10.3390/technologies12030033`.

4.2   Kinematic models

The transperineal prostate biopsy procedure consists of straight needle insertion into tissues, without twisting. For this reason, the original bicycle model [67] cannot be used in this context because it describes a needle trajectory in the 3D space which is not distinguishable from the unicycle model when limited to the 2D space. Therefore, our comparison will consider the unicycle [66] and the extended bicycle models [68]. These models consider a bevelled-tip needle driven by an insertion speed v. The tip moves along a path defined by the surrounding material's properties, the geometry of the needle's bevelled tip, and the needle insertion speed. We suppose that the needle is inserted at a constant velocity v, measured with respect to the $\{A\}$ frame along the z-axis and without twisting.

4.2.1   Unicycle Model

The unicycle model considers the needle tip as located at the center of a single wheel (unicycle) lying on the ZY plane as shown in Fig. 4.5. The labels $\{A\}$ and $\{B\}$ represent the global fixed frame and the needle tip frame, respectively.
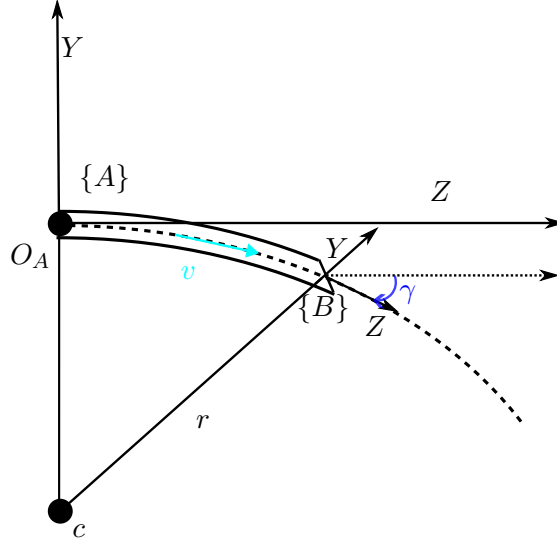
Figure 4.5: Unicycle model of a flexible needle with a bevelled tip.

According to this model, the needle tip follows a planar path formed by single-arc of fixed curvature with center $c = [0, c_y]$ and radius r, considering the entry point O_A at $(0, 0)$ in the $\{A\}$ frame. Here we assume that the needle tip is oriented such that bending occurs toward the negative y-axis as in Fig. 4.5. Let (z, y, γ) define the configuration of the needle tip frame shown in Fig.4.5, where the vector (z, y) is the tip location and γ is the angle between the z-axis of the $\{A\}$ frame and the z-axis of the $\{B\}$ frame that is the needle tip direction. Considering that the needle bends toward the negative y-axis, we have $\gamma \in [-\pi/2, 0]$.

Since the wheel movement satisfies the pure rolling, non-slipping, constraint, in the $\{B\}$ frame, the velocity has only z-axis component, without lateral movements:

$$^{B}v_y = 0 \tag{4.2a}$$

where we suppose that the wheel speed v_z equals the insertion velocity. The dynamic evolution of the needle configuration can be described as:

$$^{A}\dot{z}(t) = \cos\gamma(t)v_z \tag{4.3a}$$

$$^{A}\dot{y}(t) = \sin\gamma(t)v_z \tag{4.3b}$$

$$^{A}\dot{\gamma}(t) = -\frac{v_z}{r} \tag{4.3c}$$

with r constant. Considering O_A as the entry point of the insertion at $t = 0$, the integration of equations (4.3), leads to:

$$^A z(t) = -r \sin \gamma(t) \tag{4.4a}$$

$$^A y(t) = c_y + r \cos \gamma(t) \tag{4.4b}$$

$$^A \gamma(t) = -\frac{v_z}{r} t \tag{4.4c}$$

4.2.2   Extended Bicycle Model

The extended bicycle model [68] considers a bicycle lying on the ZY plane as shown in Fig. 4.6 where the labels $\{A\}$, $\{B\}$ and $\{C\}$ denote, respectively, the global fixed frame, the needle tip frame (back wheel) and the front wheel frame. The model consists of two wheels positioned at a fixed distance l from each other with the front wheel oriented at a fixed angle β. The well-known bicycle model with front and back wheels is defined as (z, y, γ), parameterized by the (z, y) location of the back wheel and the angle of the bicycle body with respect to the horizontal, γ. The constraints for the front and back wheels are formed by setting the sideways velocity of the wheels to zero. Using the Pfaffian constraints, the following dynamical system is obtained:

$$\dot{z} = v_z \cos \gamma \tag{4.5a}$$

$$\dot{y} = v_z \sin \gamma \tag{4.5b}$$

$$\dot{\gamma} = \frac{v_z}{l} \tan \beta \tag{4.5c}$$

with β constant. This model has been modified in such a way that, when the needle is moving forward into the tissue, lateral movements can happen on the back wheel due to tissue deformation. In this case, the final shape of the needle doesn't follow the tip path. This model, in contrast to the bicycle model (4.5), accounts for this phenomenon by considering an additional state θ. As for the unicycle model, we suppose that the needle path points toward the negative y-axis starting from the entry point O_A. As in the standard bicycle, (z, y, θ) represents the $\{B\}$ frame configuration which is the back wheel body frame. Differently from the standard bicycle model, the needle tip configuration is (z, y, γ) where γ is the angle between the z-axis of the $\{A\}$ frame and the needle tip velocity vector $^B v$. In practice, γ describes a back wheel slippage phenomenon along the y-axis of $\{B\}$ frame. If γ defines the needle tip velocity with respect to the frame $\{A\}$, α defines the same quantity respect to frame $\{B\}$ and the following relation holds

$$^B \alpha = \theta - \gamma \tag{4.6}$$

As the needle bends toward the negative y-axis, the tissue deformation pulls the needle in the opposite direction, so $\alpha \in [-\pi/2, 0]$ and $\gamma \in [-\pi/2, 0]$. The needle tip velocity vector $^B v$ and the lateral slipping velocity $^B v_y$ are defined as:
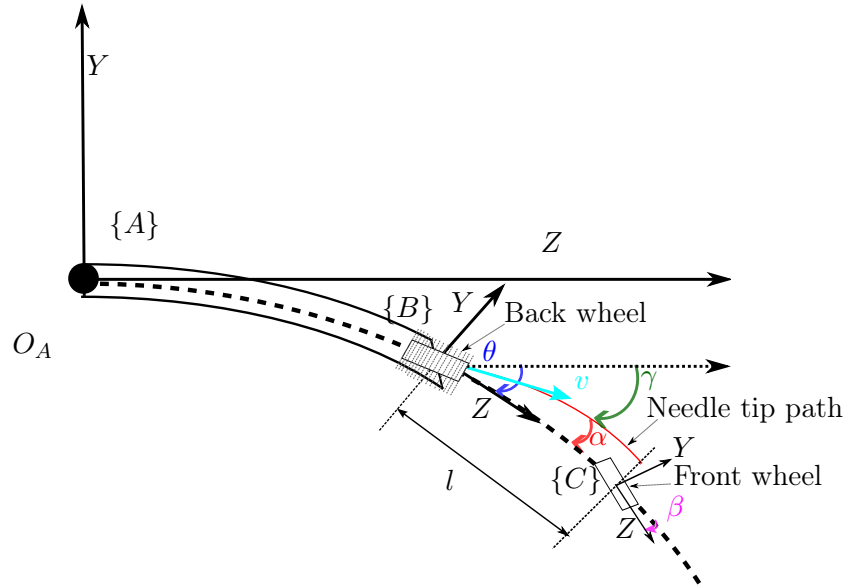
Figure 4.6: Extended bicycle model of a flexible needle with a bevelled tip.

$$^{B}v = v_z + v_y \tag{4.7a}$$

$$^{B}v_y = v_z \tan \alpha \tag{4.7b}$$

where authors assume α as a quadratic function of γ

$$^{B}\alpha = \lambda_1 \gamma^2 + \lambda_2 \gamma \tag{4.8}$$

and λ_i represent tissue-specific parameters related to its mechanical properties. Considering the definition of α as the slippage of the back wheel (Eq. (4.8)), it is clear that for non-zeros λ_1 and λ_2, the needle path deviates from the constant curvature circular path corresponding to $\lambda_1 = \lambda_2 = 0$. Using the definition of the needle tip velocity ^{B}v (4.7a) and the angle $^{B}\alpha$ (4.6), the angle $^{B}\theta$ can be expressed as

$$^{B}\dot{\theta} = \frac{v_z + v_y}{l}[\tan(\theta - \gamma) + \tan\beta] \tag{4.9}$$

Considering the angle $^{B}\alpha$ (4.6)- (4.8) the time variation of the angle $^{B}\gamma$, $^{B}\dot{\gamma}$, is calculated as

$$^{B}\dot{\gamma} = \dot{\theta} - \dot{\alpha} \tag{4.10a}$$

$$^{B}\dot{\gamma} = \dot{\theta} - \dot{\gamma}(2\lambda_1\gamma + \lambda_2) \tag{4.10b}$$

$$^{B}\dot{\gamma} = \frac{\dot{\theta}}{1 + 2\lambda_1\gamma + \lambda_2} \tag{4.10c}$$

$$^{B}\dot{\gamma} = \frac{\dot{\theta}}{1 + \frac{\partial\alpha}{\partial\gamma}} \tag{4.10d}$$

Finally, the extended bicycle model [68] can be written as:

$$^{B}\dot{z} = v\cos\gamma \tag{4.11a}$$

$$^{B}\dot{y} = v\sin\gamma \tag{4.11b}$$

$$^{B}\dot{\theta} = \frac{v}{l}[\tan(\theta-\gamma)+\tan\beta] \tag{4.11c}$$

$$^{B}\dot{\gamma} = \frac{\dot{\theta}}{1+\frac{\partial\alpha}{\partial\gamma}} \tag{4.11d}$$

4.3   Method

The experimental comparison has been carried out with the setup shown in Fig 4.7. It consists of a robotic system which performs the insertion with a bevelled tip needle. This system, described in Section 4.3.4, includes a force sensor on the needle base and an external RGB-D camera. The insertions were performed on phantoms with different stiffnesses that emulate the prostate with different tumour levels defined by the Gleason score, which is a grading system for the progress of the tumour. Phantoms' preparation is described in Section 4.3.5.
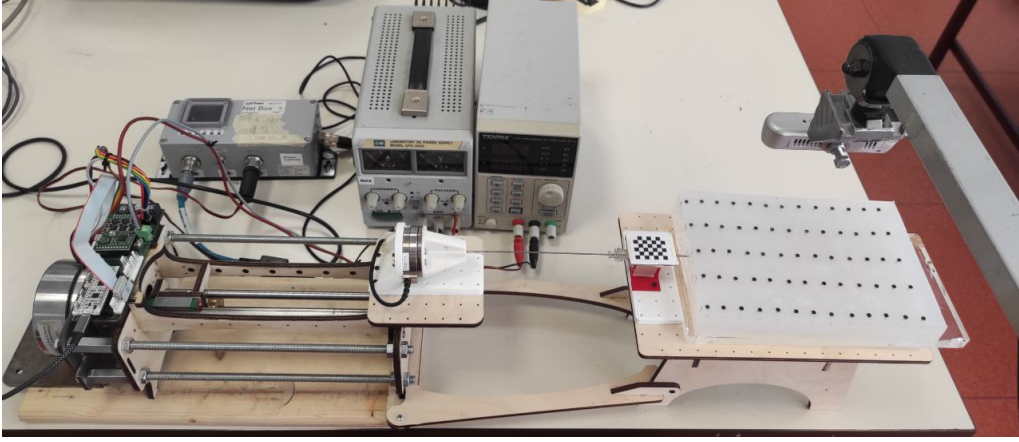
Figure 4.7: Expeimental Setup: A robotic system which performs the insertion with a bevelled tip needle into transparent phantoms

A fundamental step of our methodology is to identify the parameters of the unicycle and extended bicycle models to fit a needle tip trajectory (Sections 4.3.1 and 4.3.2). The trajectory is reconstructed using a vision algorithm (Section 4.3.3) that identifies and tracks the needle tip throughout its insertion.

4.3.1   Unicycle Model Identification

This section introduces a methodology to estimate the parameters r and c_y for the unicycle model. Given the needle tip coordinates $^{B}z(t)$ and $^{B}y(t)$ computed

from the vision algorithm (see section 4.3.3), these are fitted to the unicycle circumference. The implicit equation of a circumference with center in $(0, c_y)$ and radius r can be written as:

$$z^2(t) + (y(t) - c_y)^2 = r^2 \tag{4.12}$$

To obtain a formulation suitable for least-square regression in the form $\Phi \vec{\rho} = b$, we rewrote (4.12) as:

$$\underbrace{2y\rho_1 + \rho_2}_{\Phi\vec{\rho}} = \underbrace{z^2 + y^2}_{b} \tag{4.13}$$

where $\rho_1 = c_y$ and $\rho_2 = r^2 - c_y^2$. Then c_y and r can be easily found.

4.3.2 Extended Bicycle Model Identification

Authors of [68] introduced a methodology to estimate the parameters of the extended bicycle model: β and l in (4.9) and λ_1, λ_2 in (4.8). From the needle tip trajectory (z, y), computed from the vision algorithm in section 4.3.3, it is possible to measure the γ angle as the orientation of the needle tip velocity in the $\{A\}$ frame:

$$\gamma = \sin^{-1}\left(\frac{\Delta y}{\Delta d}\right) = \tan^{-1}\left(\frac{\Delta y}{\Delta z}\right) \tag{4.14}$$

where Δy, Δz, and Δd denote, respectively, the variations of the needle tip deflection, insertion, and depth between two sample times. In this context, depth refers to the Euclidean distance in the ZY plane between two successive tip positions. The angle θ is not directly measurable, but its time variation can be expressed in two different formulations leading to:

$$\dot{\theta} = \frac{v}{l}\left(\tan\left(\lambda_1\gamma^2 + \lambda_2\gamma\right) + \tan\beta\right) \tag{4.15a}$$

$$\dot{\theta} = \dot{\gamma}\left(1 + \frac{\partial\alpha}{\partial\gamma}\right) = \dot{\gamma}(1 + 2\lambda_1\gamma + \lambda_2) \tag{4.15b}$$

where (4.15a) is obtained from (4.9) substituting (4.8) while (4.15b) is calculated from (4.11d) considering (4.8). We combined (4.15a) and (4.15b) to obtain

$$-2l\lambda_1\gamma\frac{\dot{\gamma}}{v} - l\lambda_2\frac{\dot{\gamma}}{v} - l\frac{\dot{\gamma}}{v} + \tan\beta + \tan\left(\lambda_1\gamma^2 + \lambda_2\gamma\right) = 0 \tag{4.16}$$

which is a function of parameters and known quantities. Known quantities are γ, (4.14), its time variation $\dot{\gamma}$ and the needle tip speed v. Unknown parameters are l, β, λ_1, λ_2 and can be identified by a non-linear least square regression algorithm, as proposed by authors [68]. Unfortunately, the objective function presents several local minima and, to improve the results, the following constraints are imposed:

$$l \in [0, 2] \tag{4.17a}$$

$$\beta \in [-\frac{\pi}{2}, 0] \tag{4.17b}$$

$$\lambda_1 \in [-1, 1] \tag{4.17c}$$

$$\lambda_2 \in [-1, 1] \tag{4.17d}$$

Even by using such constraints, this methodology, as proposed by authors [68], was not always able to find an appropriate solution. For this reason, we used a genetic algorithm to minimize the residual error between the experimental data and the predicted ones.

4.3.3   Needle recognition and tracking

To track the needle tip position in each time frame, we used the *semantic segmentation* module based on the Generative Adversarial Network (GAN) model [95]. Compared to the other models, this network has the advantage of requiring very few RGB samples representing the setup to obtain high-quality results. The GAN consists of two main components: a generator and a discriminator.

- Generator: The generator takes an input image, processes it through a neural network, and produces an output image. It learns to create realistic and visually appealing results by mimicking the patterns, textures, and styles found in the training data. As training progresses, the generator becomes increasingly adept at generating images that are indistinguishable from real data.

- Discriminator: The discriminator, on the other hand, acts as a critic. It tries to distinguish between real images from the training dataset and fake images generated by the generator. Through adversarial training, the discriminator becomes skilled at identifying flaws or inconsistencies in the generated images.

As training continues, the generator and discriminator engage in a competitive process, with the generator constantly improving its ability to generate convincing output, while the discriminator becomes better at discerning real from fake. This dynamic equilibrium ultimately results in the generator producing high-quality, pixel-to-pixel output that retains the essential characteristics of the input data.

Figure 4.8 shows an example of segmentation of an image acquired from the realsense camera. The classes corresponding to objects in the scene are encoded following the Table 4.1.

Once we obtained the segmented image, we defined the workspace by placing a chessboard over a 3D-printed support where the needle passes through. This allows us to retrieve the pixels/millimeters ratio that is needed to have the needle position in the 3D metric space. Starting from the pose of the chessboard, we
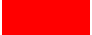
Color	Semantic Meaning
⬛	Background
🟥	Needle
🟦	Markers
🟨	Tissue

Table 4.1: Semantic Scene Color Encoding

(a) Realsense view   (b) Segmented image
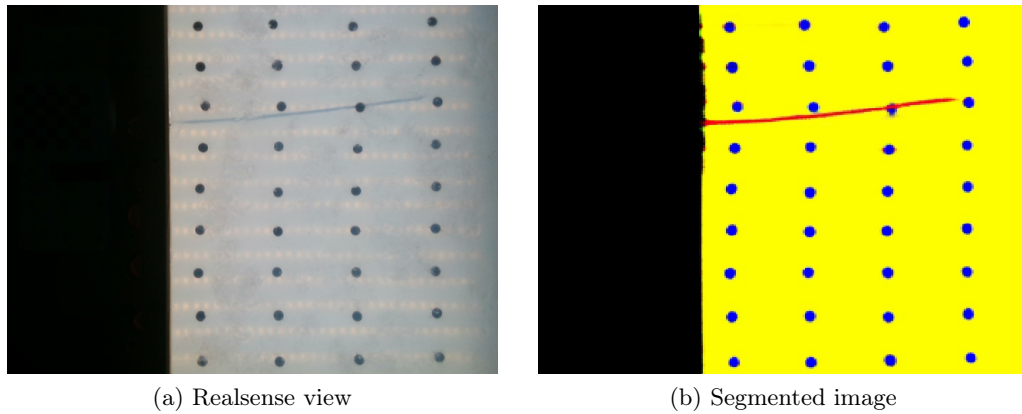
Figure 4.8: An example of real-time semantic segmentation computed with the realsense camera

Figure 4.9: An example frame with the needle tip estimation represented as a red dot

filter out an area of interest around the needle path and create a bounding box in the semantic image then work with a smaller image. Finally, we segment the needle from the semantic image and then we can extract the center point of the needle tip as shown in Fig 4.9, which will be used later for model estimation.

The coordinates (z, y) of the needle tip, which are derived from the mask obtained through semantic segmentation for each frame, are individually subjected to a third-order polynomial fitting process over time-to-position data in order to mitigate measurement noise.

4.3.4   Experimental Setup

We design a robotic system to perform insertion experiments into tissues, with one degree of freedom (DoF) capable of translational motion along the needle's

principal axis. A mechanical drive system pushes the needle into the phantom using a direct drive motor (model EC90flat) and a worm gear system. The trajectory of the needle tip is reconstructed by using an Intel RealSense d435 camera positioned approximately 20 centimeters from the surface of the phantom, operating at a rate of 30 Hz to capture the images fed into the vision algorithm. The use of transparent phantoms and a camera allows us to acquire the entire needle tip trajectory during the insertion with good accuracy, which is something ultrasound imaging cannot afford due to its noise.

The needle bevel tip is oriented so that the needle deflection plane ZY is parallel to the imaging plane. In the experiments, a standard 18 gauge brachytherapy needle with a bevel angle of 15∘ was used. The insertions are carried out at various constant velocities to a depth of 100 mm.

4.3.5 Phantom Design

In our experimentation comparison, we consider four transparent phantoms with increasing stiffness (30, 50, 70, 100 kPa) in the range of prostate gland stiffnesses in benign and malignant disease conditions [96, 97]. Two-component silicone elastomers (SL 3358 A and SL 3358 B, KCC Silicone) were utilized in equal amounts for the preparation of the phantom. Silicone oil (G Line T100, KCC Silicone) in differing amounts (50, 55.5, 66.6) and 0.03 wt % cotton fibers were added to the silicone mixture to adjust the stiffness of the model and simulate the fibrous and muscular tissue of the prostate. The preparation of the first layer of the phantom body with fibers (2.5 cm height) was followed by the insertion of the 65 pin markers (13 x 5 rows) positioned at the required locations (Fig. 4.10 - a). Subsequently, the final layer of the phantom (0.5 cm height) with fibers was produced by curing the silicone formulation that is equivalent to the bottom layer. Each layer was cured separately at 70 °C in an oven for 100 min (20 cm x 14 cm x 3 cm) (Fig. 4.10 - b).

(a)   (b)
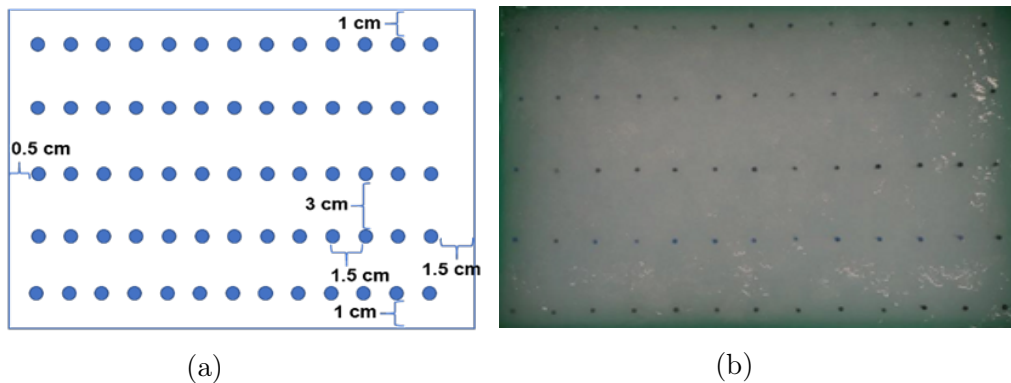
Figure 4.10: a) The sketch of the prostate phantom and the markers; b) The view of the prostate phantom from the top

4.3.6 Mechanical Characterization

Different formulations of the two-component silicone elastomers with silicone oil and cotton fibers supplements were prepared in dog bone shape according to the American Society for Testing and Materials International (ASTM) standards. The specimens were tested with 200 N force via the Universal Testing Machine (UTM) (Zwick/Roell) and an average of three tests were reported (Fig. 4.11).
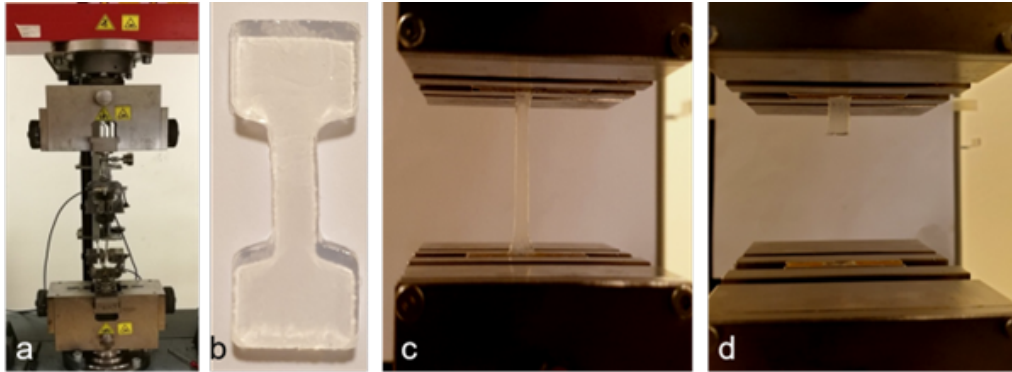
Figure 4.11: a) The mechanical properties measurement setup in Zwick/Roell UTM, b) silicone sample prepared in dog-bone shape, and the image of the silicone sample, c) during the tensile test and d) at the end of the test (fracture)

The stiffnesses were adjusted with the addition of silicone oil and supplementary materials (e.g., cotton fibers) to reach the highest resemblance to the reported values of the prostate tissue. The stiffness of the phantom body range was between 32.8–107 kPa (Fig. 4.12).
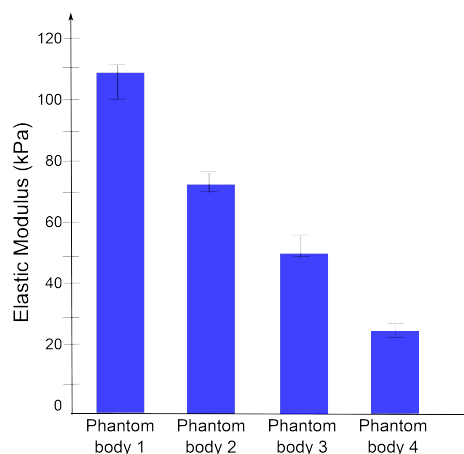
Figure 4.12: The stiffness of the different silicone-based prostate model formulations with supplements that are utilized in the design of the phantom body

4.4 Experimental Results

Using the robotic setup the needle is inserted to a depth of 100 mm considered between the longest distances between the perineum and the apex of the prostate. Insertions are performed at two different velocities (10, 20 mm/s). For each stiffness and velocity pair, we performed four repetitions. We performed model identification procedures using data from the first three repetitions, and we used the fourth repetition to assess the prediction accuracy of the models. The unicycle model and the extended bicycle model are labeled, respectively, as $M1$ and $M2$. Results in Tables 4.2 and 4.3 show respectively the average final tip deflection $\omega_{exp}(l)$ with the standard deviation of the final tip position σ_{exp} and the average tip error identification for unicycle model e_{meanM1} and extended bicycle model e_{meanM2} with their standard deviation σ_{eM1} and σ_{eM2} for every phantom's stiffness and velocity pair. Figure 4.13 shows examples of data from identification procedures related to phantoms with stiffness 30 kPa and 100 kPa at velocities $10\frac{mm}{s}$ and $20\frac{mm}{s}$.

Insertion Velocity [mm/s]	Stiffness [kPa]	$\omega_{exp}(l)$ [mm]	σ_{exp} [mm]
10	30	-8.26	0.43
	50	-10.80	0.95
	70	-12.18	1.13
	100	-12.58	1.11
20	30	-7.65	0.56
	50	-9.51	0.20
	70	-10.57	1.14
	100	-11.78	1.44

Table 4.2: Average final tip deflection and standard deviation considering 8 experimental conditions (4 phantoms and 2 velocities pair) with four repetitions each

We estimated the parameters of the models by performing a least square identification for the unicycle model and using a genetic algorithm for the extended bicycle model as described in Sections 4.3.1 and 4.3.2. To robustify the identification procedure the estimated parameters are averaged considering data from the three insertions. To access the models' accuracy, the simulated needle trajectory is compared to experimental data of the fourth repetition. Results in Table 4.4 show the maximum tip prediction error for the unicycle model e_{maxM1} and the extended bicycle model e_{maxM2} and their root-mean-squared error (RMSE) $RMSE_{M1}$ and $RMSE_{M2}$ for every phantom's stiffness and velocity pair. Figure 4.14 shows examples of data from prediction procedures related to phantoms with stiffness 30 kPa and 100 kPa at velocities $10\frac{mm}{s}$ and $20\frac{mm}{s}$.

(a) Stiffness 30 kPa, Velocity 10 mm/s

(b) Stiffness 30 kPa, Velocity 20 mm/s

(c) Stiffness 100 kPa, Velocity 10 mm/s

(d) Stiffness 100 kPa, Velocity 20 mm/s
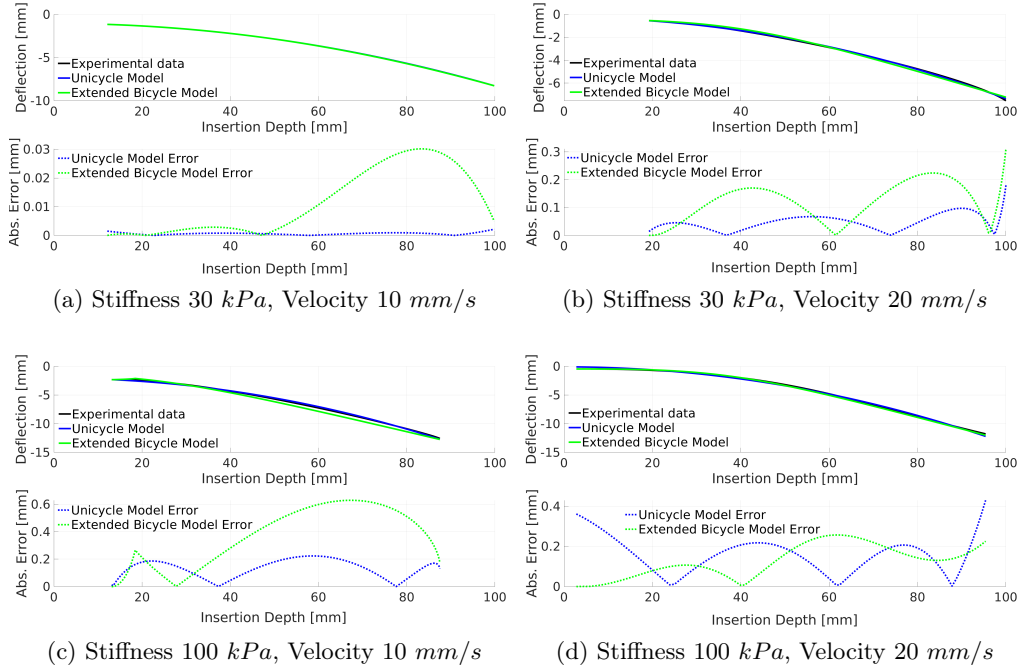
Figure 4.13: Models identification on needle insertions experiments in the prostate stiffness range (30, 100 kPa) at two different velocities (10, 20 mm/s)

Insertion Velocity [mm/s]	Stiffness [kPa]	e_{meanM1} [mm]	e_{meanM2} [mm]	σ_{eM1} [mm]	σ_{eM2} [mm]
	30	$6.15\ 10^{-4}$	0.012	$5.18\ 10^{-7}$	$2.52\ 10^{-4}$
10	50	0.051	0.065	0.005	0.006
	70	0.056	0.338	0.005	0.156
	100	0.130	0.364	0.020	0.174
	30	0.053	0.126	0.004	0.022
20	50	0.013	0.142	0.022	0.032
	70	0.014	0.151	0.027	0.033
	100	0.153	0.166	0.031	0.034

Table 4.3: Average tip error identification and standard deviation for Unicycle Model and Extended Bicycle Model considering 8 experimental conditions (4 phantoms and 2 velocities pair) with four repetitions each

4.5 Discussion

From Table 4.2 one can notice that insertions exhibit a notable final displacement, around 10% of their whole length and this motivates the use of models for the prediction of needle deflection. From Table 4.4 one can observe that both models are quite accurate in predicting the tip's final position. In terms of RMSE, we

Insertion Velocity [mm/s]	Stiffness [kPa]	e_{maxM1} [mm]	e_{maxM2} [mm]	$RMSE_{M1}$ [mm]	$RMSE_{M2}$ [mm]
10	30	0.18	0.77	0.11	0.49
	50	0.32	0.45	0.26	0.27
	70	0.43	2.07	0.31	0.76
	100	0.44	1.04	0.28	0.71
20	30	0.20	0.61	0.12	0.19
	50	0.22	0.45	0.18	0.26
	70	0.29	0.78	0.19	0.33
	100	0.75	1.24	0.29	0.85

Table 4.4: Maximum tip prediction error and the root-mean-squared error (RMSE) for Unicycle Model e_{maxM1} and Extended Bicycle Model e_{maxM2} considering 8 experimental conditions (4 phantoms and 2 velocities pair) with four repetitions each

(a) Stiffness 30 kPa, Velocity 10 mm/s (b) Stiffness 30 kPa, Velocity 20 mm/s

(c) Stiffness 100 kPa, Velocity 10 mm/s (d) Stiffness 100 kPa, Velocity 20 mm/s
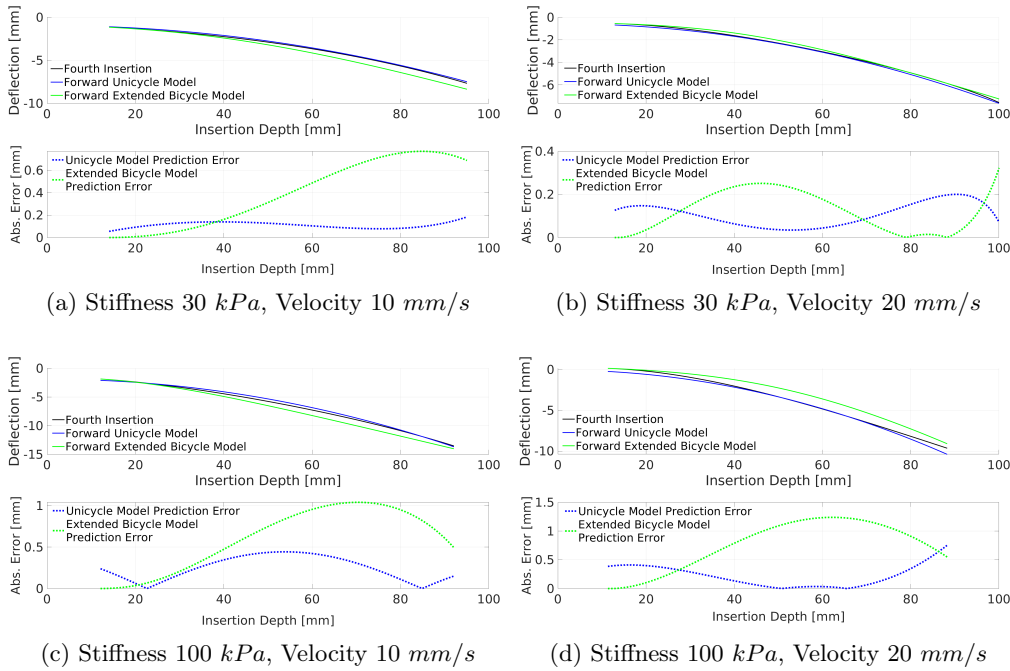
Figure 4.14: Unicycle and Extended Bicycle Models prediction on the fourth needle insertion experiment

achieved a tenth of a millimetre accuracy down to the millimetre (in the case of more rigid phantom insertions). The maximum errors are less than or equal to 0.75 mm for the unicycle model and less or equal to 2.07 mm for the extended bicycle model. In spite of its lower complexity, the unicycle model is more accurate than the extended bicycle model. Both in terms of RMSE and maximum error, the

unicycle model is, on average, 2.5 times more accurate than the extended bicycle model. In any experimental scenario, the unicycle model generates smaller errors than the extended bicycle model (for each stiffness and velocity pair). For both model, higher errors in predicting the final needle tip deflection are obtained when the needle is pushed into the more rigid phantoms (70 and 100 kPa) at the highest velocity ($20 \frac{mm}{s}$). Since the unicycle model is a linear regression identification, it is faster and requires less computational effort than the extended bicycle model. We measured an average computation time of $0.7ms$ for the unicycle model and $45s$ (range $20s$-$65s$, executed on Intel Core i7-6700HQ processor running 4 threads) for the extended bicycle model as a final remark.

4.6   Conclusion

This work compared the kinematic models for robotic needle insertion targeting straight needle insertion as in transperineal prostate biopsy. Our experimental comparison considers four transparent phantoms with increasing stiffness simulating fibrous and muscular prostate tissue in benign and malignant disease conditions. Experimental results show that, in spite of its simplicity, the unicycle model outperformed the extended bicycle model in terms of accuracy and computational time. Modelling the deformation of the needle and surrounding tissue during insertion into the prostate allows surgeons to take samples accurately from the organ, thus ensuring the accurate identification of prostate cancer and indicating the level of risk for the patient. A prostate biopsy is one of the most impactful and independent parameters that direct physicians to the surgery if it is not possible to follow other treatments. In this comparative study of kinematic models, the tissue is considered rigid or with small deformation, allowing the deflection of the needle to be modelled without necessarily considering the forces of interaction with the tissue. However, heterogeneous tissues with different stiffness levels are crossed in the transperineal biopsy procedure. In our future work, we will evaluate non-straight needle insertions, including more complex models such as virtual spring mechanical models [98, 99] and finite elements models [100, 101, 102] and the influence of skin tension, subcutaneous fat, and pelvic diaphragm will be considered to evaluate the targeting error in a complete robotic needle insertion procedure.

Chapter 5

Conclusions

In the first part of the thesis, we investigated interaction control algorithms which take advantage of the inherent flexibility of commonly used surgical instruments. First, we leverage on continuum mechanics theory to model the surgical instrument and investigate passivity properties. Using the Lyapunov approach, we demonstrated that proportional force control based on a collocated feedback signal from a continuum flexible beam is always passive with respect to the environment port. However, using the same methodology, we were not able to derive passivity results for non-collocated feedback. Then, we used high-order approximants to investigate non-collocated feedback, focusing on application-specific conditions. The result was that passivity imposes a constraint on maximum gain values, having more strict conditions as non-collocation approaches the tip of the instrument.

In the second part, we focus on modelling the interaction between a bevel-tip biopsy needle and the surrounding tissue to enable automated needle insertion during a robotic prostate biopsy. In this context, the objective is to estimate the deflection of the tip during insertion and to plan the trajectory accordingly. An experimental comparison is conducted to assess the accuracy of existing models in predicting needle deflection. Interestingly, we found that the simplest model is also the most accurate both in fitting and prediction.

All the results in this thesis are validated on custom setups, which mimic some of the challenges of real robotic surgery within the Autonomous Robotic Surgery (ARS) and the Autonomous Prostate Biopsy Project (PROST) projects.

Bibliography

[1] C. D'Ettorre, A. Mariani, A. Stilli, F. Rodriguez y Baena, P. Valdastri, A. Deguet, P. Kazanzides, R. H. Taylor, G. S. Fischer, S. P. DiMaio, A. Menciassi, and D. Stoyanov, "Accelerating surgical robotics research: A review of 10 years with the da vinci research kit," *IEEE Robotics & Automation Magazine*, vol. 28, no. 4, pp. 56–78, 2021.

[2] E. Tagliabue, M. Bombieri, P. Fiorini, and D. Dall'Alba, "Autonomous robotic surgical systems: Needing common sense to achieve higher levels of autonomy [opinion]," *IEEE Robotics & Automation Magazine*, vol. 30, no. 3, pp. 149–163, 2023.

[3] G.-Z. Yang, J. Cambias, K. Cleary, E. Daimler, J. Drake, P. E. Dupont, N. Hata, P. Kazanzides, S. Martel, R. V. Patel, V. J. Santos, and R. H. Taylor, "Medical robotics—regulatory, ethical, and legal considerations for increasing levels of autonomy," *Science Robotics*, vol. 2, no. 4, 2017.

[4] G. Van de Perre, T. Hubert, T. Verstraten, and B. Vanderborght, "Investigating the potential of flexible links for increased payload to mass ratios for collaborative robotics," *IEEE Access*, vol. 11, pp. 15981–15995, 2023.

[5] J. Liu, M. Tan, and X. Zhao, "Legged robots — an overview," *Transactions of the Institute of Measurement and Control*, vol. 29, no. 2, pp. 185–202, 2007.

[6] A. Calanca and P. Fiorini, "On the role of compliance in force control," in *Intelligent Autonomous Systems 13*, pp. 1243–1255, Springer International Publishing, 2016.

[7] D. W. Robinson, *Design and analysis of series elasticity in closed-loop actuator force control*. PhD thesis, Massachussetts Institute of Technology, 2000.

[8] R. D. Howard, *Joint and Actuator Design for Enhanced Stability in Robotic Force Control*. PhD thesis, Massachussetts Institute of Technology, 1990.

[9] G. Pratt and M. Williamson, "Series elastic actuators," in *Proceedings 1995 IEEE/RSJ International Conference on Intelligent Robots and Systems. Hu-*

man Robot Interaction and Cooperative Robots, vol. 1, pp. 399–406 vol.1, 1995.

[10] A. Calanca, E. Sartori, and B. Maris, "Force control of lightweight series elastic systems using enhanced disturbance observers," *Robotics and Autonomous Systems*, vol. 164, p. 104407, 2023.

[11] A. Calanca, R. Muradore, and P. Fiorini, "A review of algorithms for compliant control of stiff and fixed-compliance robots," *IEEE/ASME Transactions on Mechatronics*, vol. 21, no. 2, pp. 613–624, 2016.

[12] T. Valency and M. Zacksenhouse, "Accuracy/robustness dilemma in impedance control," *Journal of Dynamic Systems Measurement and Control-transactions of The Asme*, vol. 125, pp. 310–319, 2003.

[13] A. Calanca, R. Muradore, and P. Fiorini, "Impedance control of series elastic actuators: Passivity and acceleration-based control," *Mechatronics*, vol. 47, pp. 37–48, 2017.

[14] H. Vallery, J. Veneman, E. van Asseldonk, R. Ekkelenkamp, M. Buss, and H. van Der Kooij, "Compliant actuation of rehabilitation robots," *IEEE Robotics & Automation Magazine*, vol. 15, no. 3, pp. 60–69, 2008.

[15] A. Calanca, E. Dimo, R. Vicario, P. Fiorini, M. Serpelloni, and G. Legnani, "Introducing series elastic links for affordable torque-controlled robots," *IEEE Robotics and Automation Letters*, vol. 4, no. 1, pp. 137–144, 2019.

[16] J. Malzahn, A. S. Phung, F. Hoffmann, and T. Bertram, "Vibration control of a multi-flexible-link robot arm under gravity," in *2011 IEEE International Conference on Robotics and Biomimetics*, pp. 1249–1254, Dec 2011.

[17] Y. Morita, F. Matsuno, Y. Kobayashi, M. Ikeda, H. Ukai, and H. Kando, "Lyapunov-based force control of a flexible arm considering bending and torsional deformation," *IFAC Proceedings Volumes*, vol. 35, no. 1, pp. 133–138, 2002. 15th IFAC World Congress.

[18] A. Garcia and V. Feliu, "Force control of a single-link flexible robot based on a collision detection mechanism," *IEE Proceedings - Control Theory and Applications*, vol. 147, pp. 588–595, November 2000.

[19] A. D. Luca and B. Sicilianot, "Inversion-based nonlinear control of robot arms with flexible links," *Journal of Guidance Control and Dynamics*, vol. 16, pp. 1169–1176, 1993.

[20] L. Meirovitch and R. G. Parker, *Fundamentals of Vibrations*. McGraw-Hill, 2000.

[21] S. Pal, H. E. Stephanou, and G. Cook, "Optimal control of a single-link flexible manipulator," *Journal of Intelligent and Robotic Systems*, vol. 2, pp. 187–199, 1989.

[22] V. Feliu, K. S. Rattan, and J. Brown, H. B., "Modeling and Control of Single-Link Flexible Arms With Lumped Masses," *Journal of Dynamic Systems, Measurement, and Control*, vol. 114, pp. 59–69, 03 1992.

[23] P. Puangmali, K. Althoefer, L. D. Seneviratne, D. Murphy, and P. Dasgupta, "State-of-the-art in force and tactile sensing for minimally invasive surgery," *IEEE Sensors Journal*, vol. 8, no. 4, pp. 371–381, 2008.

[24] M. B. Naf, A. S. Koopman, S. J. Baltrusch, C. R. Guerrero, B. Vanderborght, and D. Lefeber, "Passive back support exoskeleton improves range of motion using flexible beams," *Frontiers in Robotics and AI*, vol. 5, 2018.

[25] V. Duindam, A. Macchelli, S. Stramigioli, and H. Bruyninckx, *Modeling and Control of Complex Physical Systems: The port-hamiltonian approach.* Germany: Springer, 2009.

[26] R. Rashad, F. Califano, A. J. van der Schaft, and S. Stramigioli, "Twenty years of distributed port-Hamiltonian systems: a literature review," *IMA Journal of Mathematical Control and Information*, vol. 37, pp. 1400–1422, 07 2020.

[27] A. van der Schaft and D. Jeltsema, "Port-hamiltonian systems theory: An introductory overview," *Foundations and Trends in Systems and Control*, vol. 1, no. 2-3, pp. 173–378, 2014.

[28] D. Feliu-Talegon, V. Feliu-Batlle, I. Tejado, B. M. Vinagre, and S. H. HosseinNia, "Stable force control and contact transition of a single link flexible robot using a fractional-order controller," *ISA Transactions*, vol. 89, pp. 139–157, 2019.

[29] J. Malzahn and T. Bertram, "Collision detection and reaction for a multi-elastic-link robot arm," *IFAC Proceedings Volumes*, vol. 47, no. 3, pp. 320–325, 2014. 19th IFAC World Congress.

[30] J. Malzahn, R. F. Reinhart, and T. Bertram, "Dynamics identification of a damped multi elastic link robot arm under gravity," in *2014 IEEE International Conference on Robotics and Automation (ICRA)*, pp. 2170–2175, 2014.

[31] J. Malzahn, R. Schloss, and T. Bertram, "Link elasticity exploited for payload estimation and force control," in *2015 IEEE/RSJ International Conference on Intelligent Robots and Systems (IROS)*, pp. 1508–1513, 2015.

[32] Y. Aoustin, C. Chevallereau, A. Glumineau, and C. Moog, "Experimental results for the end-effector control of a single flexible robotic arm," *IEEE Transactions on Control Systems Technology*, vol. 2, no. 4, pp. 371–381, 1994.

[33] M. Shao, Y. Huang, and V. Silberschmidt, "Intelligent manipulator with flexible link and joint: Modeling and vibration control," *Shock and Vibration*, vol. 2020, pp. 1–15, 01 2020.

[34] X. He, S. Zhang, Y. Ouyang, and Q. Fu, "Vibration control for a flexible single-link manipulator and its application," *IET Control Theory & Applications*, vol. 14, 03 2020.

[35] P. Chedmail, Y. Aoustin, and C. Chevallereau, "Modelling and control of flexible robots," *International Journal for Numerical Methods in Engineering*, vol. 32, no. 8, pp. 1595–1619, 1991.

[36] B. Siciliano and W. J. Book, "A singular perturbation approach to control of lightweight flexible manipulators," *The International Journal of Robotics Research*, vol. 7, no. 4, pp. 79–90, 1988.

[37] F. Lewis and M. Vandegrift, "Flexible robot arm control by a feedback linearization/singular perturbation approach," in *[1993] Proceedings IEEE International Conference on Robotics and Automation*, pp. 729–736 vol.3, 1993.

[38] K. S. Yeung and Y. P. Chen, "Regulation of a one-link flexible robot arm using sliding-mode technique," *International Journal of Control*, vol. 49, no. 6, pp. 1965–1978, 1989.

[39] A. Shawky, D. Zydek, Y. Z. Elhalwagy, and A. Ordys, "Modeling and nonlinear control of a flexible-link manipulator," *Applied Mathematical Modelling*, vol. 37, no. 23, pp. 9591–9602, 2013.

[40] W. Book, "Recursive lagrangian dynamics of flexible manipulator arms via transformation matrices," *IFAC Proceedings Volumes*, vol. 16, no. 19, pp. 5–17, 1983. 2nd IFAC Symposium on computer Aided Design of Multivariable Technological Systems, West Lafayette, USA, 15-17 September 1982.

[41] A. De Luca and B. Siciliano, "Joint-based control of a nonlinear model of a flexible arm," in *1988 American Control Conference*, pp. 935–940, 1988.

[42] S. Tso, T. Yang, W. Xu, and Z. Sun, "Vibration control for a flexible-link robot arm with deflection feedback," *International Journal of Non-Linear Mechanics*, vol. 38, no. 1, pp. 51–62, 2003.

[43] J. Robert H. Cannon and E. Schmitz, "Initial experiments on the end-point control of a flexible one-link robot," *The International Journal of Robotics Research*, vol. 3, no. 3, pp. 62–75, 1984.

[44] Y. Sakawa, F. Matsuno, and S. Fukushima, "Modeling and feedback control of a flexible arm," *Journal of Robotic Systems*, vol. 2, no. 4, pp. 453–472, 1985.

[45] A. Chassiakos and G. Bekey, "Pointwise control of a flexible manipulator arm," *IFAC Proceedings Volumes*, vol. 18, no. 16, pp. 181–185, 1985. 1st IFAC Symposium on Robot Control (SYROCO '85), Barcelona, Spain', 6-8 November 1985.

[46] E. Bayo, "A finite-element approach to control the end-point motion of a single-link flexible robot," *Journal of Robotic Systems*, vol. 4, no. 1, pp. 63–75, 1987.

[47] G. Hastings and W. Book, "A linear dynamic model for flexible robotic manipulators," *IEEE Control Systems Magazine*, vol. 7, no. 1, pp. 61–64, 1987.

[48] E. Barbieri and U. Ozguner, "Unconstrained and constrained mode expansions for a flexible slewing link," in *1988 American Control Conference*, pp. 83–88, 1988.

[49] D. Wang and M. Vidyasagar, "Transfer functions for a single flexible link," in *Proceedings, 1989 International Conference on Robotics and Automation*, pp. 1042–1047 vol.2, 1989.

[50] D. Wang and M. Vidyasagar, "Passive control of a single flexible link," in *Proceedings., IEEE International Conference on Robotics and Automation*, pp. 1432–1437 vol.2, 1990.

[51] H. Geniele, R. Patel, and K. Khorasani, "Control of a flexible-link manipulator," in *Proceedings of 1995 IEEE International Conference on Robotics and Automation*, vol. 1, pp. 1217–1222 vol.1, 1995.

[52] V. Feliu and F. Ramos, "Strain gauge based control of single-link flexible very lightweight robots robust to payload changes," *Mechatronics*, vol. 15, no. 5, pp. 547–571, 2005.

[53] D. Feliu-Talegon, V. Feliu-Batlle, I. Tejado, B. M. Vinagre, and S. H. HosseinNia, "Stable force control and contact transition of a single link flexible robot using a fractional-order controller," *ISA Transactions*, vol. 89, pp. 139–157, 2019.

[54] E. Colgate and N. Hogan, "An analysis of contact instability in terms of passive physical equivalents," in *Proceedings, 1989 International Conference on Robotics and Automation*, pp. 404–409 vol.1, 1989.

[55] S. Eppinger and W. Seering, "Understanding bandwidth limitations in robot force control," in *Proceedings. 1987 IEEE International Conference on Robotics and Automation*, vol. 4, pp. 904–909, 1987.

[56] S. Eppinger and W. Seering, "On dynamic models of robot force control," in *Proceedings. 1986 IEEE International Conference on Robotics and Automation*, vol. 3, pp. 29–34, 1986.

[57] A. Meurer, C. P. Smith, M. Paprocki, O. Čertík, S. B. Kirpichev, M. Rocklin, A. Kumar, S. Ivanov, J. K. Moore, S. Singh, T. Rathnayake, S. Vig, B. E. Granger, R. P. Muller, F. Bonazzi, H. Gupta, S. Vats, F. Johansson, F. Pedregosa, M. J. Curry, A. R. Terrel, v. Roučka, A. Saboo, I. Fernando, S. Kulal, R. Cimrman, and A. Scopatz, "Sympy: symbolic computing in python," *PeerJ Computer Science*, vol. 3, p. e103, Jan. 2017.

[58] D. E. Whitney, "Force feedback control of manipulator fine motions," *Journal of Dynamic Systems Measurement and Control-transactions of The Asme*, vol. 99, pp. 91–97, 1977.

[59] A. Calanca, E. Dimo, E. Palazzi, and L. Luzi, "Enhancing force controllability by mechanics in exoskeleton design," *Mechatronics*, vol. 86, p. 102867, 2022.

[60] S. P. Buerger and N. Hogan, "Relaxing passivity for human-robot interaction," in *2006 IEEE/RSJ International Conference on Intelligent Robots and Systems*, pp. 4570–4575, 2006.

[61] C. H. Pernar, E. M. Ebot, K. M. Wilson, and L. A. Mucci, "The Epidemiology of Prostate Cancer," *Cold Spring Harbor Perspectives in Medicine*, vol. 8, no. 12, p. a030361, 2018.

[62] S. Verma, P. L. Choyke, S. C. Eberhardt, A. Oto, C. M. Tempany, B. Turkbey, and A. B. Rosenkrantz, "The Current State of MR Imaging–targeted Biopsy Techniques for Detection of Prostate Cancer," *Radiology*, vol. 285, pp. 343–356, Nov. 2017.

[63] B. Maris, C. Tenga, R. Vicario, L. Palladino, N. Murr, M. De Piccoli, A. Calanca, S. Puliatti, S. Micali, A. Tafuri, *et al.*, "Toward autonomous robotic prostate biopsy: a pilot study," *International Journal of Computer Assisted Radiology and Surgery*, vol. 16, pp. 1393–1401, 2021.

[64] S. P. DiMaio and S. E. Salcudean, "Needle insertion modeling and simulation," *IEEE Transactions on robotics and automation*, vol. 19, no. 5, pp. 864–875, 2003.

[65] C. Simone and A. M. Okamura, "Modeling of needle insertion forces for robot-assisted percutaneous therapy," in *Proceedings 2002 IEEE International Conference on Robotics and Automation (Cat. No. 02CH37292)*, vol. 2, pp. 2085–2091, IEEE, 2002.

[66] W. Park, J. S. Kim, Y. Zhou, N. J. Cowan, A. M. Okamura, and G. Chirikjian, "Diffusion-based motion planning for a nonholonomic flexible needle model," in *Proceedings of the 2005 IEEE International Conference on Robotics and Automation*, pp. 4600–4605, 2005.

[67] R. J. Webster III, J. S. Kim, N. J. Cowan, G. S. Chirikjian, and A. M. Okamura, "Nonholonomic modeling of needle steering," *The International Journal of Robotics Research*, vol. 25, no. 5-6, pp. 509–525, 2006.

[68] B. Fallahi, M. Khadem, C. Rossa, R. Sloboda, N. Usmani, and M. Tavakoli, "Extended bicycle model for needle steering in soft tissue," in *2015 IEEE/RSJ International Conference on Intelligent Robots and Systems (IROS)*, pp. 4375–4380, 2015.

[69] S. P. DiMaio and S. E. Salcudean, "Needle steering and model-based trajectory planning," in *Medical Image Computing and Computer-Assisted Intervention - MICCAI 2003*, (Berlin, Heidelberg), pp. 33–40, Springer Berlin Heidelberg, 2003.

[70] O. Goksel, S. E. Salcudean, and S. P. DiMaio, "3d simulation of needle-tissue interaction with application to prostate brachytherapy," *Computer Aided Surgery*, vol. 11, no. 6, pp. 279–288, 2006.

[71] O. Goksel, E. Dehghan, and S. E. Salcudean, "Modeling and simulation of flexible needles," *Medical Engineering & Physics*, vol. 31, no. 9, pp. 1069 – 1078, 2009.

[72] D. Gao, Y. Lei, B. Lian, and B. Yao, "Modeling and Simulation of Flexible Needle Insertion Into Soft Tissue Using Modified Local Constraints," *Journal of Manufacturing Science and Engineering*, vol. 138, 08 2016.

[73] R. Alterovitz, K. Goldberg, and A. Okamura, "Planning for steerable bevel-tip needle insertion through 2d soft tissue with obstacles," in *Proceedings of the 2005 IEEE International Conference on Robotics and Automation*, pp. 1640–1645, April 2005.

[74] R. Alterovitz, A. Lim, K. Goldberg, G. S. Chirikjian, and A. M. Okamura, "Steering flexible needles under markov motion uncertainty," in *2005 IEEE/RSJ International Conference on Intelligent Robots and Systems*, pp. 1570–1575, Aug 2005.

[75] R. Alterovitz, K. Goldberg, J. Pouliot, R. Taschereau, and I. C. Hsu, "Sensorless planning for medical needle insertion procedures," in *Proceedings 2003 IEEE/RSJ International Conference on Intelligent Robots and Systems (IROS 2003) (Cat. No.03CH37453)*, vol. 4, pp. 3337–3343 vol.3, Oct 2003.

[76] N. Chentanez, R.Alterovitz, D. Ritchie, L. Cho, K. K. Hauser, K. Goldberg, J. R. Shewchuk, and J. F. O'Brien, "Interactive simulation of surgical needle insertion and steering," in *ACM SIGGRAPH 2009 Papers*, 2009.

[77] A. Maghsoudi and M. Jahed, "A comparison between disturbance observer-based and model-based control of needle in percutaneous applications," in

IECON 2012 - 38th Annual Conference on IEEE Industrial Electronics Society, pp. 2104–2108, Oct 2012.

[78] A. Maghsoudi and M. Jahed, "Inverse dynamics control of needle in prostate brachytherapy," in *2012 IEEE International Conference on Industrial Technology*, pp. 510–515, March 2012.

[79] M. Torabi, K. Hauser, R. Alterovitz, V. Duindam, and K. Goldberg, "Guiding medical needles using single-point tissue manipulation," in *2009 IEEE International Conference on Robotics and Automation*, pp. 2705–2710, May 2009.

[80] V. G. Mallapragada, N. Sarkar, and T. K. Podder, "Robot-assisted real-time tumor manipulation for breast biopsy," *IEEE Transactions on Robotics*, vol. 25, pp. 316–324, April 2009.

[81] S.Misra, K.Reed, B.Schafer, W.Ramesh, and A.Okamura, "Mechanics of flexible needles robotically steered through soft tissue," *The International Journal of Robotics Research*, vol. 29, p. 1640–1660, June 2010.

[82] S. Misra, K. B. Reed, A. S. Douglas, K. T. Ramesh, and A. M. Okamura, "Needle-tissue interaction forces for bevel-tip steerable needles," in *2008 2nd IEEE RAS EMBS International Conference on Biomedical Robotics and Biomechatronics*, pp. 224–231, Oct 2008.

[83] A. M. Okamura, C. Simone, and M. D. O'Leary, "Force modeling for needle insertion into soft tissue," *IEEE Transactions on Biomedical Engineering*, vol. 51, pp. 1707–1716, Oct 2004.

[84] M. Khadem, C. Rossa, N. Usmani, R. S. Sloboda, and M. Tavakoli, "Semi-automated needle steering in biological tissue using an ultrasound-based deflection predictor," *Annals of Biomedical Engineering*, vol. 45, 2017.

[85] M. Khadem, C. Rossa, N. Usmani, R. S. Sloboda, and M. Tavakoli, "Introducing notched flexible needles with increased deflection curvature in soft tissue," in *2016 IEEE International Conference on Advanced Intelligent Mechatronics (AIM)*, pp. 1186–1191, July 2016.

[86] A. Asadian, R. V. Patel, and M. R. Kermani, "A distributed model for needle-tissue friction in percutaneous interventions," in *2011 IEEE International Conference on Robotics and Automation*, pp. 1896–1901, May 2011.

[87] M. Khadem, B. Fallahi, C. Rossa, R. S. Sloboda, N. Usmani, and M. Tavakoli, "A mechanics-based model for simulation and control of flexible needle insertion in soft tissue," in *2015 IEEE International Conference on Robotics and Automation (ICRA)*, pp. 2264–2269, May 2015.

[88] C. Rossa, M. Khadem, R. Sloboda, N. Usmani, and M. Tavakoli, "Adaptive quasi-static modelling of needle deflection during steering in soft tissue," *IEEE Robotics and Automation Letters*, vol. 1, pp. 916–923, July 2016.

[89] G. Wan, Z. Wei, L. Gardi, D. B. Downey, and A. Fenster, "Brachytherapy needle deflection evaluation and correction," *Medical Physics*, vol. 32, no. 4, pp. 902–909, 2005.

[90] K. G. Yan, T. Podder, Y. Yu, T. Liu, C. W. S. Cheng, and W. S. Ng, "Flexible needle–tissue interaction modeling with depth-varying mean parameter: Preliminary study," *IEEE Transactions on Biomedical Engineering*, vol. 56, pp. 255–262, Feb 2009.

[91] R. J. Roesthuis, M. Abayazid, and S. Misra, "Mechanics-based model for predicting in-plane needle deflection with multiple bends," in *2012 4th IEEE RAS EMBS International Conference on Biomedical Robotics and Biomechatronics (BioRob)*, pp. 69–74, June 2012.

[92] K. B. Reed, A. M. Okamura, and N. J. Cowan, "Modeling and control of needles with torsional friction," *IEEE Transactions on Biomedical Engineering*, vol. 56, pp. 2905–2916, Dec 2009.

[93] D. Glozman and M. Shoham, "Image-guided robotic flexible needle steering," *IEEE Transactions on Robotics*, vol. 23, pp. 459–467, June 2007.

[94] D. Glozman and M.Shoham, "Flexible needle steering and optimal trajectory planning for percutaneous therapies," in *Medical Image Computing and Computer-Assisted Intervention – MICCAI 2004* (D. C. Barillot and P.Hellier, eds.), pp. 137–144, Springer Berlin Heidelberg, 2004.

[95] P. Isola, J.-Y. Zhu, T. Zhou, and A. A. Efros, "Image-to-image translation with conditional adversarial networks," in *Computer Vision and Pattern Recognition (CVPR), 2017 IEEE Conference on*, 2017.

[96] N. Hungr, J. A. Long, V. Beix, and J. Troccaz, "A realistic deformable prostate phantom for multimodal imaging and needle-insertion procedures," *Medical Physics*, vol. 39, no. 4, pp. 2031–2041, 2012. Publisher: John Wiley and Sons Ltd.

[97] Y. Ji, L. Ruan, W. Ren, G. Dun, J. Liu, Y. Zhang, and Q. Wan, "Stiffness of prostate gland measured by transrectal real-time shear wave elastography for detection of prostate cancer: a feasibility study," *The British Journal of Radiology*, vol. 92, p. 20180970, May 2019.

[98] D. Glozman and M. Shoham, "Flexible needle steering and optimal trajectory planning for percutaneous therapies," in *Medical Image Computing and Computer-Assisted Intervention–MICCAI 2004: 7th International Conference, Saint-Malo, France, September 26-29, 2004. Proceedings, Part II 7*, pp. 137–144, Springer, 2004.

[99] D. Glozman and M. Shoham, "Image-guided robotic flexible needle steering," *IEEE Transactions on Robotics*, vol. 23, no. 3, pp. 459–467, 2007.

[100] R. Alterovitz, K. Goldberg, and A. Okamura, "Planning for steerable bevel-tip needle insertion through 2d soft tissue with obstacles," in *Proceedings of the 2005 IEEE international conference on robotics and automation*, pp. 1640–1645, IEEE, 2005.

[101] R. Alterovitz, A. Lim, K. Goldberg, G. S. Chirikjian, and A. M. Okamura, "Steering flexible needles under markov motion uncertainty," in *2005 IEEE/RSJ International Conference on Intelligent Robots and Systems*, pp. 1570–1575, IEEE, 2005.

[102] E. Dehghan and S. E. Salcudean, "Needle insertion parameter optimization for brachytherapy," *IEEE Transactions on Robotics*, vol. 25, no. 2, pp. 303–315, 2009.